Virginia Commonwealth University

VCU Scholars Compass

2011

Design of control release drug delivery system (DDS) for imaging and therapeutic applications

Sweta Naik
Virginia Commonwealth University

www.manaraa.com

Design of control release drug delivery system (DDS) for imaging and therapeutic applications

A dissertation submitted in partial fulfillment of the requirement for the degree of Doctor of Philosophy at Virginia Commonwealth University

By

Sweta Hemang Naik
M.Sc. South Gujarat University, India, 2002

Director: Dr. Everett E. Carpenter
Associate Professor, Department of Chemistry

Virginia Commonwealth University
Richmond, Virginia
September 2011

Acknowledgements

In the completion of this dissertation, there are many people who encouraged, guided and supported; without them it would not have been possible to complete this journey. Before I begin I would like to seek the blessing of my Guruji (spiritual Guru). First, I would like to thank my husband Hemang for his constant encouragement, love and support that keeps me going every day. Truly I could not have achieved this without your support. I would also like to thank my daughter Vedika who has been the motivation that actually pushed me to go harder every day to finish graduate school. I take this opportunity to extend my deep appreciation to Hemang's parents, my parents, brother, sister-in-law and other family members who have helped me in different ways to get to where I am today.

I am indebted to my advisor, Dr. Everett Carpenter for his continuous help, guidance, and encouragement throughout the graduate work. Dr. Carpenter has been extremely supportive during tough times, which gave me strength and determination to continue my studies, and for that I will forever be grateful. I consider myself very lucky to have had this great opportunity to be one of his students. I am grateful to my committee members Dr. Maryanne Collinson, Dr. Massimo Bertino and Dr. Joseph Topich for their time and valuable advice. I would like to acknowledge the chemistry department at VCU. I have learned so much from faculty and labmates, not only in lab but for the many hours of conversation, relaxation, and inspiration.

Table of Contents

List of Figures

Chapter: 1

Chapter: 2

Chapter: 3

Chapter: 4

Chapter: 5

Chapter:6

List of Tables

Abstract

DESIGN OF CONTROL RELEASE DRUG DELIVERY SYSTEM (DDS) FOR IMAGING AND THERAPEUTIC APPLICATIONS

By Sweta H. Naik, Ph.D.

A dissertation submitted in partial fulfillment of the requirements for the degree of Doctor of Philosophy at Virginia Commonwealth University.

Virginia Commonwealth University, 2011

Director: Dr. Everett E. Carpenter
Associate Professor of Chemistry

The main challenge in disease treatment is no more the discovery of new therapeutic drugs, but to provide targeted delivery of therapeutic drugs to specific sites without incurring systemic toxicity effects. An efficient way of reducing the toxicity is by encapsulating the drug with a biodegradable matrix that can provide controlled release of the drug along with local heating of the drug. Local heating can be obtained by incorporating magnetic iron oxide particles that heat upon exposure to AC electromagnetic fields. The magnetic iron oxide nanoparticles are also gaining much attention as MRI contrast agents. Thus it would be of potential benefit if a drug delivery system is designed to encapsulate the drug as well as the magnetic iron oxide nanoparticles within a biodegradable matrix, thereby providing a dual modal imaging and therapeutic delivery system. The key step in the design of a dual modal drug delivery system is

the encapsulation of the magnetic iron oxide nanoparticles with polymer of choice. The magnetic iron oxide nanoparticles were encapsulated into a robust poly (styrene-co-vinylbenzylchloride-co-divinylbenzene) (PSVBDVB) to study these synthetic variations upon encapsulation with a polymer. The next step to the design of drug delivery system was to replace the PSVBDVB polymer by a biocompatible and biodegradable polymer- Poly (lactide-co-glycolide) (PLGA). The PLGA composites containing the Fe@FeOx core shell nanoparticles and the drug analog [Ru(bpy) dye] was prepared by oil-in water emulsion solvent evaporation technique. The local heating of the PLGA composites was also achieved by irradiating the Fe@FeOx nanoparticles with 2.45 GHz microwave radiations. Higher Ru(bpy) dye release from the composites by locally heating the sample with 2.45 GHz microwave pulse compared to externally heating the composite sample was achieved.

The final step was the design of controlled release drug delivery system with dual modal imaging and therapeutic capabilities. To obtain narrow sized PLGA composites the Fe@FeOx nanoparticles were replaced by chloroform based ferrofluid. The ferrofluid was synthesized by novel thermolysis technique. The release of the dye from the PLGA composites when placed in the Rf induction coil was determined by fluorescence spectroscopy and a linear increase in the fluorescent intensity was observed with time. Also, the controlled release of the dye from the composites was achieved by a pulsed Rf treatment. Magnetic resonance imaging was also performed using the PLGA composites which showed enhancement in the T_2-weighted image contrast and thus negligible reduction in the contrast capabilities of the iron oxide particles ($R_2 =$ 58.7 $s^{-1}mM^{-1}$). The PLGA composites containing the drug analog and the iron oxide nanoparticles thus constitute a controlled release drug delivery system with dual modal imaging and therapeutic capabilities.

Chapter 1. Introduction

1.1. Overview

Advances in the drug development and delivery have evolved in several phases, beginning with the botanical phase of human civilization, via the synthetic chemistry era, and now presently in the biotechnology era. Researchers are continuously developing new and more powerful drugs, but still the drugs are administered conventionally. The conventional route of administration of these drugs are primarily enteral or perenteral routes. Enteral route of drug administration rely on introducing a drug to the digestive tract through the mouth or rectum. Perenteral route of drug administration involves the injection or infusion of a drug into the body (intravenous or intramuscular).[1,2] Many vaccines as well as the chemotherapeutic drugs are delivered through the perenteral route of administration.[1] Oral delivery is most attractive due to high patient convenience and compliance. In both type of administration the resultant effect is systemic i.e. upon administration the drug molecules are distributed throughout the body. [3,4] Several different types of cell are involved into the diseased tissues: the diseased cells, normal cells from which the disease evolves, vascular cells, fibroblasts, and immune cells. The systemically distributed drug metabolizes throughout the body leading to the damage of healthy cells and tissues, resulting in general toxicity and poor acceptance of the treatments by patients.[4] For example, the treatment of cancer, HIV infections, tuberculosis, and malaria generally involve very powerful drugs, and their use is considerably reduced due to the occurrences of side effects. In addition, conventionally delivered drugs get diluted in the blood and body fluids resulting in insufficient drug concentration at the diseased site.[5] Drugs are often too quickly cleared from the blood stream due to the uptake by the reticuloendothelial system (RES) i.e. the body's immune system, and the kidneys.[5] This leads to a treatment approach of higher doses, or the inconvenience of continuous infusion again resulting in

perhaps intolerable or even more toxic levels of drugs.[4] This side effects result in a dose limiting situation where the drug administration has to be brought to a level that is just tolerable to the patients, but may be less effective. Also the drugs may be unstable and degrades quickly or may have a very poor solubility in aqueous solution. For instance hydrophobic drugs get precipitated in blood plasma, and require solubilizers/stabilizers in order to administer the drugs.[6] Unfortunately, these solubilizers/stabilizers not only dilutes the potency of the drugs but also adds up to the drug toxicity.[7] **Therefore, for effective treatment it is necessary to maintain the drug concentration between the effective therapeutic level and the maximum tolerable limit for prolonged period of time as shown in figure**.[8,9] The drug release from conventional route is in a form of a burst where in the drug is released all at a time and needs to be given on a regular basis. A controlled release drug delivery system is desirable that can release the drug effectively in the therapeutic window over a long period of time. This will allow for fewer drug dosage and patient compliance. This all can be achieved by designing a controlled release drug delivery system specific for the diseased cells within the body. The challenges presented here can be overcome by properly integrating nanotechnology with the established knowledge of the disease characteristics.
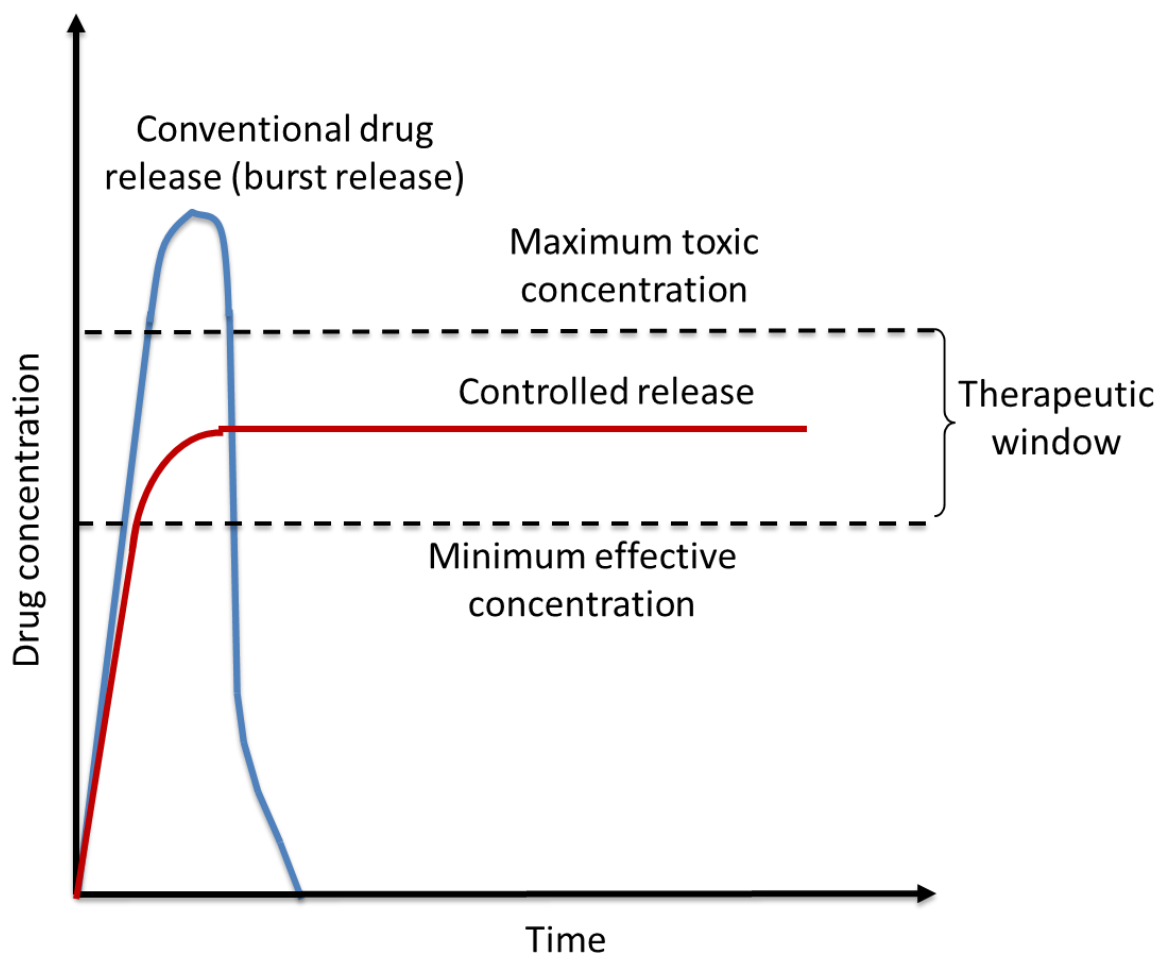
Figure 1-1: Therapeutic window showing the effect of conventional burst release and controlled release relative to the effective concentration and the maximum tolerable toxic concentration.

1.2. Nanotechnology

Nanotechnology is an emerging field of science that can facilitate a way to overcome the short coming to an efficient and safe drug delivery system.[10,11] Nanotechnology is an interdisciplinary field of science which deals with the design, synthesis, characterization and application of devices and materials in the nanoscale range.[4] Although nanomaterials are widely considered to be an invention of modern science, they actually have a very long history.

Nanoparticles (NPs) were empirically used by artisans as far back as the 9th century BC in Mesopotamia to generate a glittering effect on the surfaces of pots. Modern nanotechnology was envisioned by the physicist and Nobel laureate Richard Feynman in his lecture "There is plenty of room at the bottom" in 1959. Nanotechnology refers to structures roughly in the 1 to 500 nm size in at least one dimension and are developed by top-down or bottom-up approaches.[12] To put this size range in perspective, an atom, molecules, proteins, virus, cell mitochondrium, red blood cells, and the mammalian cells are around 0.1 nm, 1 nm, 10 nm, 100 nm, 1000 nm, 10,000 nm and 100,000 nm respectively as shown in Figure 1-2. The application of nanotechnology to life sciences has been termed as nanobiotechnology.[13-15]
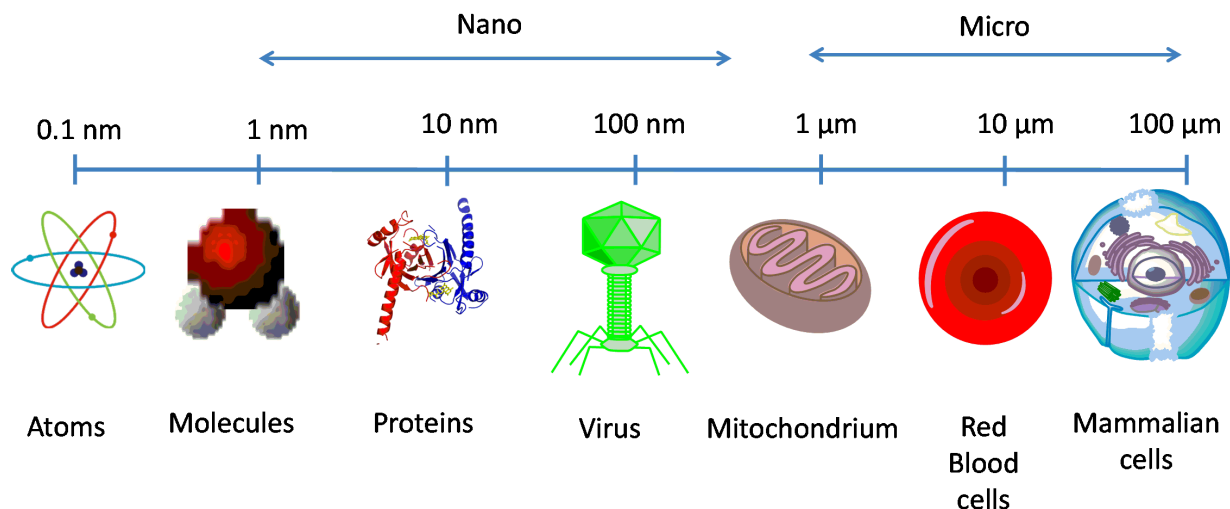
Figure 1-2: Representation of size of species in the nano and micron region

These nanoscale materials possess unique and unusual properties and are currently used in multidisciplinary scientific areas that range from physics and engineering to biochemistry. Among many unique physical and chemical properties at the nanoscale, one basic physical property for nanomaterials is the large surface area to volume ratio.[16] For example, in bulk materials only a relatively small percentage of atoms can be at or near the surface. When the

dimensions continue to shrink to the nanoscale, the percentage of bulk atoms decreases while the surface atoms increase. This provides relatively large (functional) surface area which is able to bind, absorb and carry other compounds such as drugs and probes.[17] Also the physiochemical properties of nanomaterials like friction and interaction with other molecules are different from their bulk counterparts. Depending on the type of application nanomaterials can be synthesized from different materials like iron, gold, silica, semiconductors, lipids or polymers. Also the nanomaterials can be fabricated into different shapes such as nanospheres, nanorods, nanotubes, nanowires. The nanomaterials due to their small size can cross biological barriers including the blood-brain barrier, transit out of blood vessel walls or the cells by difference uptake mechanisms thereby interacting with wide range of biological entities. These characteristics confer nanomaterials high interaction and transport capabilities making them attractive for the design of biosensors, imaging and/or therapeutic agents. Advances in nanobiotechnology have heralded the advent of several innovative nanomaterials, which are set to revolutionize the field of targeted drug delivery system.

1.3. Drug delivery system (DDS)

A drug delivery system (DDS) is defined as a system in which the bioactive agent (drug) is integrated with a non-active agent (carrier) in such a way that the drug is released from the carrier in a predetermined manner, at a constant rate in what is known as zero-order release, in a cyclic manner, or in response to an external trigger such as a change in pH, ionic strength or temperature of the medium.[18-21] Ideally the carrier system, whether it is synthetic or natural, should be able to provide a nontoxic support system that can be manufactured on an industrial scale that can be translated into a cost-effective, clinically practical medicine.[22] In addition to controlling the rate and duration of the drug release, the DDS should be able to target the drugs

to specific organs and tissues, as well as individual organelles within the individual cells (i.e. tumors, bacterial cells of definite species) or respond to a biofeedback mechanism such as glucose levels in hyperglycemia patients. The schematic of an ideal drug delivery system is depicted in Figure 1-3.
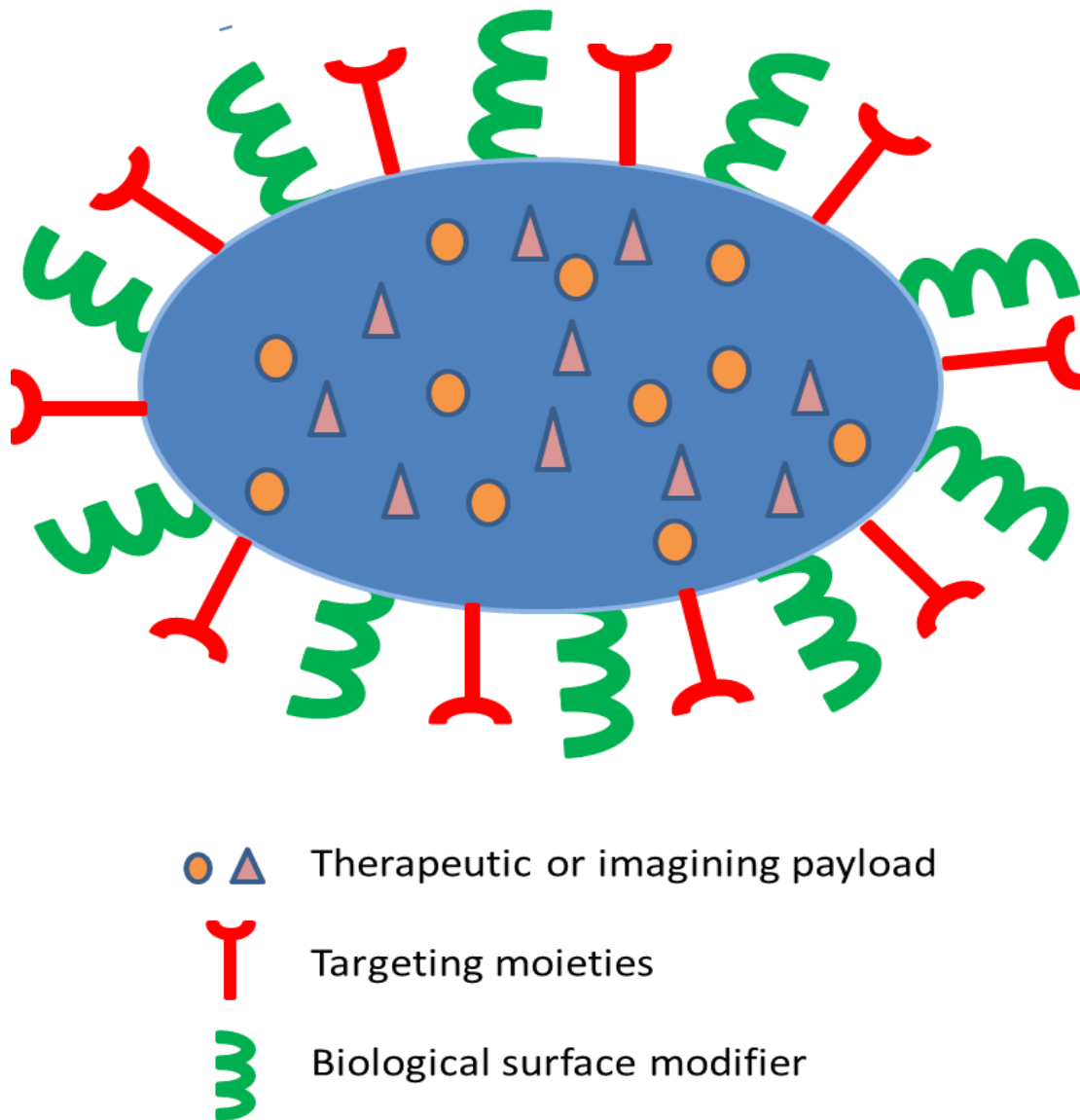
Figure 1-3: Schematic representation of an ideal drug delivery system (DDS)

The benefits offered by controlled DDS over traditional pharmaceutical administration include maintenance of the drug levels within desired limits, maximize the pharmaceutical drug

activity, the need for fewer doses, and better patient compliance.[23] In addition, association of the drug with a carrier may provide enhanced protection to the active agent from degradation in the physiological environment, and improve the stability of the drug that is required for formulation and administration. **The field of DDS is characterized by the need of delivering the existing drugs to specific targets in the diseased cells through specific cell reorganization mechanism and be able to overcome the biological barriers that prevent the drug from effectively reaching the target.** [19,24-27] The application of nanobiotechnology to drug delivery has benefited all streams of medical science with oncology being the foremost

1.4. Cancer

Cancer is a class of disease in which the cells in a part of the body begin to grow out of control.[28] Cell multiplication (proliferation) is a normal physiologic process that occurs in almost all tissues and under many circumstances, such as response to injury, immune responses, or to replace cells those have died or have been shed as a part of their lifecycle. Normally the balance between proliferation and cell death is tightly regulated to ensure the integrity of organs and tissues. But sometimes mutations in the DNA disturb the orderly process and leads to the uncontrolled and often rapid proliferation of cells. This leads to either a benign tumor or a malignant tumor (cancer). Benign tumors do not spread to other parts of the body or invade other tissues, and they are rarely a threat to life. Malignant tumors can invade other organs, spread to distant locations (metastasize) and become life threatening. Cancer is the second leading cause of death in United States exceeded only by heart disease, with an estimate of 1.6 million new cases and 571,950 deaths in 2011.[29] Symptoms and signs of cancer depend on the type and location of the cancer, but more often the symptoms do not start until the disease has reached an advanced stage. Most cancers are diagnosed by biopsy, and depending on the

location of the tumor the biopsy may be simple procedure or a serious operation. So an efficient cancer detection technique needs to develop which can diagnose the disease at an early treatable stage. The principal treatment approach followed these days is surgery; if the tumor is accessible and/or chemotherapy and radiation therapy that can eradicate the tumors located deep inside the body.[28] Both chemotherapy and radiation therapy suffers from their non-specific mode of actions leading to adverse side effects.[30-33] For example, the most common chemotherapeutic agents such as paclitaxel and doxorubicin exhibit anti-cancer effects by inducing apoptotic death of rapidly dividing cells, but they can also kill several types of normal cells that divide rapidly in ordinary circumstances.[34-37] Since the current chemotherapy is mainly based on a whole-body treatment with the chemotherapeutic agents, it is inevitable to cause many dangerous side effects associated with the non-selective cytotoxic effect of the medications. Thus, drug delivery in cancer is important for optimizing the effect of drugs and reducing the toxic side effects. Significant advances have been made in the treatment of many cancer subtypes, but the therapies currently available, lack the patient compliance.[38] The National Cancer Institute (NCI) launched the alliance for nanotechnology in cancer for improving cancer mortality defined the path of opportunities in the following areas:[39]

1. Research tools that makes it possible to rapid identification of new biological targets for clinical developments.

2. Agents that can monitor predictive molecular changes to identify precancerous cells and prevent them from becoming malignant.

3. Imaging agents and diagnostics that can allow clinicians to detect cancer in the earliest, most easily treatable, pre-symptomatic stage.

4. Multi-functional targeted systems that can deliver multiple therapeutic agents directly to cancer cells.

5. Systems that can provide real-time assessments of therapeutic and surgical efficacy.

6. Novel methods that can manage the symptoms that reduce quality of life

The use of nanocarriers as DDS for anticancer therapeutics has great potential to revolutionize the future of cancer therapies. In addition nanocarriers with imaging agents offer opportunities to exploit optical imaging or magnetic resonance imaging (MRI) for cancer imaging and guided hyperthermia therapy.[40] Inorganic nanoparticles have emerged as viable candidate as imaging, diagnostics and sensing agents for cancer treatments.[41] The nano sized metal and semiconductor nanoparticles possess unique electronic, optical and catalytic properties that very significantly from the properties of their bulk counterparts. Nanoparticles based on gold, semiconductor metals and iron oxide have been extensively studies as imaging and diagnostic agents.[40] When applied to biological systems this metallic nanoparticles have the potential to improve the imaging techniques such as X-ray imaging, near infrared (NIR) imaging, position emission spectroscopy (PET) and magnetic resonance imaging (MRI). Metallic nanoparticle probes can enhance the signal sensitivity, and spatial resolution thereby improving the sensitivity of the imaging techniques. Of all the metallic nanoparticles, the focus has been on iron oxide nanoparticles due to their biocompatible nature and their superparamagnetic property. These iron oxide nanoparticles are responsive to externally applied electromagnetic radiations and will produce heat by magnetic hysteresis and will be discussed in detail in chapter 3. In this dissertation the focus would be on the encapsulation of the iron oxide nanoparticles with the active agent into a polymer matrix of choice. The encapsulated nanoparticles can be inductively heated by hyperthermia principals to obtain enhanced drug release profiles.

1.5. Nanocarriers for cancer imaging and therapy

The use of drug delivery systems (DDS), composed of a nanocarrier and its active agent (imaging and therapeutic agent), dramatically changes the physicochemical properties of the drug as well as its bio-distribution. It is particularly relevant in the case of very active drugs whose use in the clinic has been limited due to their toxicity on vital organs such as heart, kidneys, bone marrow and it may also provide new delivery options for the existing drugs available. The most common examples of nanocarriers are prodrugs, dendrimers, liposomes, micelles, hydrogels, carbon nanotubes, implantable systems, and polymeric composites.[42-48] Figure 1-4 shows the different types of nanocarriers used as drug delivery systems. Nanocarriers have the potential to improve the therapeutic index of the drug by increasing the drug payload within the carrier and achieve desired drug release, there by reducing the drug toxicity. Nanocarriers can also improve the solubility and stability of the drug, allowing a higher drug payload.

Prodrugs are pharmacological substances that are administered in the inactive form and are metabolized in vivo into the active form.[49,50] Prodrugs are used when the drugs have unattractive physiochemical properties. They are generated through the chemical conjugation of an active agent with a carrier molecule, which could be a polymer or lipid. Dendrimers are highly branched macromolecules of very small size, and mono-distributed molecular weight that can be used to deliver high payloads of drugs through conjugation of the active agent with the numerous surface or interior functional groups.[51-53] The term originates from 'dendron' meaning a tree in Greek. Dendrimers are generally prepared using either a divergent method or a convergent one. Both prodrugs and dendrimers have the disadvantage of chemically modifying

the active agent, possibly affecting its *in vivo* activity.[53-56] Liposomes are artificially prepared vesicles consisting of vesicles formed by phospholipids bilayers, and which deliver the drug into cells by fusing with cellular membranes.[48,57,58] Liposomes can be prepared by disrupting biological membranes, for example by sonication. Micelles consist of self-assembled vesicles formed by lipids or other amphiphilic molecules (including polymers), which can be used for encapsulation and isolation of hydrophobic molecules from the surrounding hydrophilic physiological environment.[47,59,60] A typical micelle in aqueous solution forms an aggregate with the hydrophilic "head" regions in contact with surrounding solvent, and the hydrophobic "tail" regions in the micelle center. Liposomes and micelles offer advantages such as prolonged circulation time, altered pharmacokinetics, and the ability to encapsulate highly hydrophobic drugs, but do not usually provide controlled release over time.[61-64] Hydrogels are materials capable of uptaking significant amounts of water and swelling in result to changes in the surrounding environment, resulting in increased pore sizes that allow controlled release of its contents.[65,66] Drug delivery systems based on hydrogels have been shown to result in low drug burst effects, but do not usually provide long term drug release.[62] Carbon nanotubes are allotropes of carbon (graphene) with a cylindrical shape.[67,68] Carbon nanotubes have many structures, differing in length, thickness, and in the type of helicity and number of layers. Although they are formed from essentially the same graphite sheet, their electrical characteristics differ depending on these variations. Carbon nanotubes in higher concentrations can interact with the body fluids and alter the function of the immune systems.[69-71] Implantable systems can provide long term drug release, but require invasive interventions for implantation and removal, thus resulting in lower patient acceptability.[72,73] Polymeric composites encapsulate drugs in either a reservoir or matrix arrangement, in which the drug is either localized to the center of the

particle and surrounded by a polymer layer, or dispersed throughout a polymeric matrix, respectively.[74,75]   Polymeric nanocomposites have shown advantages over nanocarriers in term of stability, storage, desired drug release kinetics, toxicity and in-vivo activity.
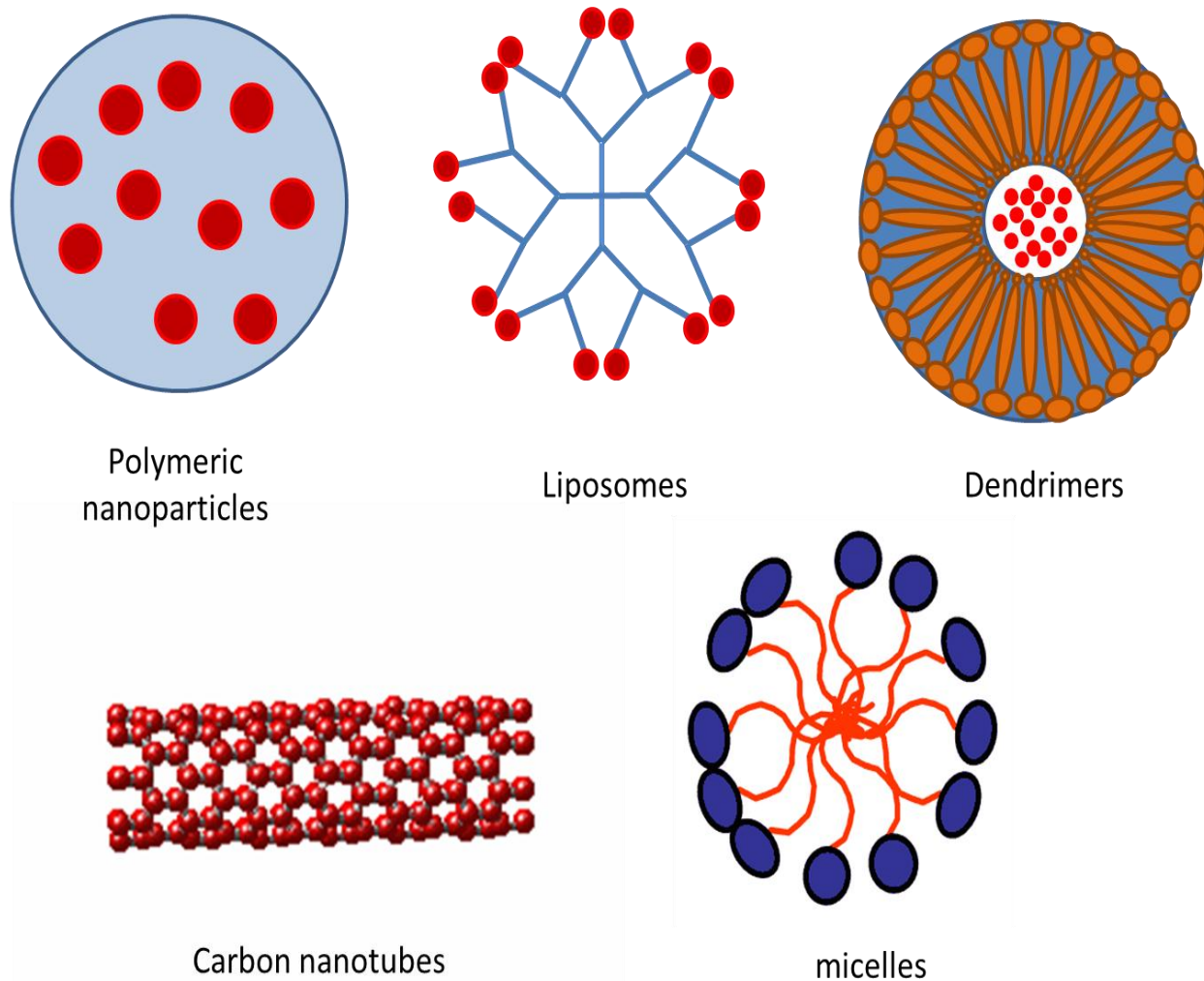
Figure 1-4: Types of nanocarriers

1.6. Polymeric composites

Polymeric composites are attractive for medical purpose due to their relatively large functional surface which can carry, bind or absorb other chemical materials like drugs, proteins, genes, and imaging probes.[43,44] Depending on the conformation, and on the material used to fabricate the polymeric composites various drug release kinetic profiles including constant (zero-order) release can be obtained by the combined effects of drug diffusion and polymer degradation. Polymeric composites can be classified into nano-composites and micro-composites based on their sizes. The micro-composites range in diameter from 1 to 250μm, while the nanocomposite ranges between 10 to 1000nm. Polymeric composites can be synthesized from number of different natural and synthetic polymers.[76] Some of the naturally occurring polymers used are dextran, cellulose, chitosan.[76] Synthetic polymers used for composite synthesis are poly (methyl methacrylate) (PMMA), poly (styrene-co-vinylbenzyl chloride-co- divinyl benzene) (PSVBDVB), polylactic acid (PLA), poly glycolic acid (PGA), poly (lactic-*co*-glycolic acid) (PLGA)[76-78]. Non-biodegradable synthetic polymers like PMMA, PSVBDVB are used for synthesizing composites but are not suitable for *in-vivo* applications as they need to be removed surgically.[79] The polyesters like PLA, PGA, and PLGA are approved by Food and drug administration (FDA) for human applications due to their biodegradability, biocompatibility, and lower toxicity and will be discussed in detail in chapter 5.[28,78] Polymeric composites, in addition, because of their small size, are able to circulate through capillaries, preferentially escape into tumor tissue because of the enhanced permeability and retention effect (EPR), and may be taken up by cells for intracellular drug delivery, and will be discussed in the

"targeted drug delivery" section. It is these properties of nanoparticles that have been exploited for the development of the targeted delivery system in this project.

1.7. Preparation of Polymeric nanoparticles

Polymeric composites can be prepared either by directly from the monomers by conventional polymerization processes or can be fabricated from the pre-synthesized polymer. The conventional polymerization approach uses the monomer as the starting point. Precipitation polymerizations and emulsion polymerization are some of the examples of conventional polymerization approach.[76,79,80] The preparation of the polymeric composites from the pre-synthesized polymers can be achieved by techniques such as emulsification solvent evaporation technique, salting out, spray drying, and nanoprecipitation to name some.[78,81-84] The selected method determines the characteristics of nanocomposites, including the size, as it the most important property because it is strongly related to the administration mode.[85] Another property influenced by the preparation process is the ability to interact with active principles contained in the drugs formulation. As a consequence, a deep knowledge of the experimental parameters like the solvents, temperature, kind of stabilizer, and stirring rate involved in each method are crucial and can bring on the characteristics change in the resulting composites.

1.7.1. Precipitation polymerization

Precipitation polymerization is a type of conventional approach for the preparation of the nanocomposites. Precipitation polymerization is a heterogeneous polymerization process that starts with a homogeneous system in the continuous phase, where the monomers and initiator are completely soluble, but upon initiation the formed polymer is insoluble and thus precipitates outs.[79][86] After precipitation of the polymer the polymerization continues with the adsorption of

the monomer and initiator on the surface of the formed polymeric particle leading to the growth of the particle. Encapsulation of the active agent (therapeutic agent/ imaging probe) can be achieved by adding it along with the monomer initiator assembles. In this technique it is difficult to obtain control over the size and morphology of the formed nanocomposites.

1.7.2. Emulsion polymerization

Emulsion polymerization is also a type of conventional approach used for the preparation of composites. Emulsion polymerization is a type of radical polymerization where in the polymerization process starts within the emulsion formed by the monomer, initiator and water.[86-88] Encapsulation of the active agent can be achieved by adding it along with the monomer initiator assembles. Polymerization is initiated by diffusion of a free-radical into the emulsion. The monomers continuously diffuse from the aqueous phase into the emulsion droplets. Due to the small dimensions of the droplets, diffusion of another free-radical into the droplets leads to quick termination as a result of coupling of the free-radicals. Thus, the polymerization occurs via a single growing chain. Hence, the molecular weight of the polymer bead can become very high before termination.[87,88]

1.7.3. Emulsification solvent evaporation technique

Emulsification solvent evaporation is the most promising technique employed for the preparation of polymeric nanocomposites. The method is based on the emulsification of an organic solution of the polymer in an aqueous phase followed by the evaporation of the organic solvent.[89-91] The polymer is dissolved in a suitable solvent such as ethyl acetate, chloroform, methylene chloride. The organic phase or aqueous phase is poured into the continuous phase (aqueous or organic phase) to form the emulsion, which is stabilized by dissolving a surfactant

into the continuous phase. Emulsification is carried out under high-shear stress to reduce the size of the emulsion droplet which is directly related with the final size of the nanocomposites. The process of emulsification is followed by evaporation of the organic solvent under vacuum, which leads to polymer precipitation and nanoparticle formation. This method has two alternatives depending on the nature of the active agent to be entrapped within the nanocomposites: normal emulsions-oil-in-water (o/w) and double emulsions-water-in-oil-in-water (w/o/w) techniques.[90]

1.7.3.1. Oil-in-water emulsion technique:

The technique is based on the emulsification of an organic solution containing the polymer and the active component in an aqueous phase, followed by the evaporation of the organic solvent. Different surfactants such as poly vinyl alcohol (PVA), sodium dodecyl sulfate (SDS) or Pluronic F68 can be dissolved in the aqueous phase to stabilize the emulsion formed. The size reduction of the emulsion droplet is done by sonication or homogenization to achieve nanosized composites. The evaporation step is required to eliminate the organic solvent present in the organic phase and leads to the precipitation of the polymer as nanocomposites with a diameter in the nanoscale range. This technique is suitable for considerable number of hydrophobic agents that are soluble in variety of water immiscible solvents and, are poorly soluble in water. Figure 1-5 represents the schematic representation of the oil-in-water emulsification technique. Important parameters to be considered for the o/w emulsion are: molecular mass and the concentration of the polymer used, co-polymer ratio and end groups employed to functionalized the polymer, type and concentration of the surfactant used, phase ratio, solvent nature, evaporation rate, drug entrapment, additives used, and the shear stress

applied.[92] o/w emulsion technique has been employed to prepare the PLGA nanocomposites in this project and will be discussed in depth in the following chapters.
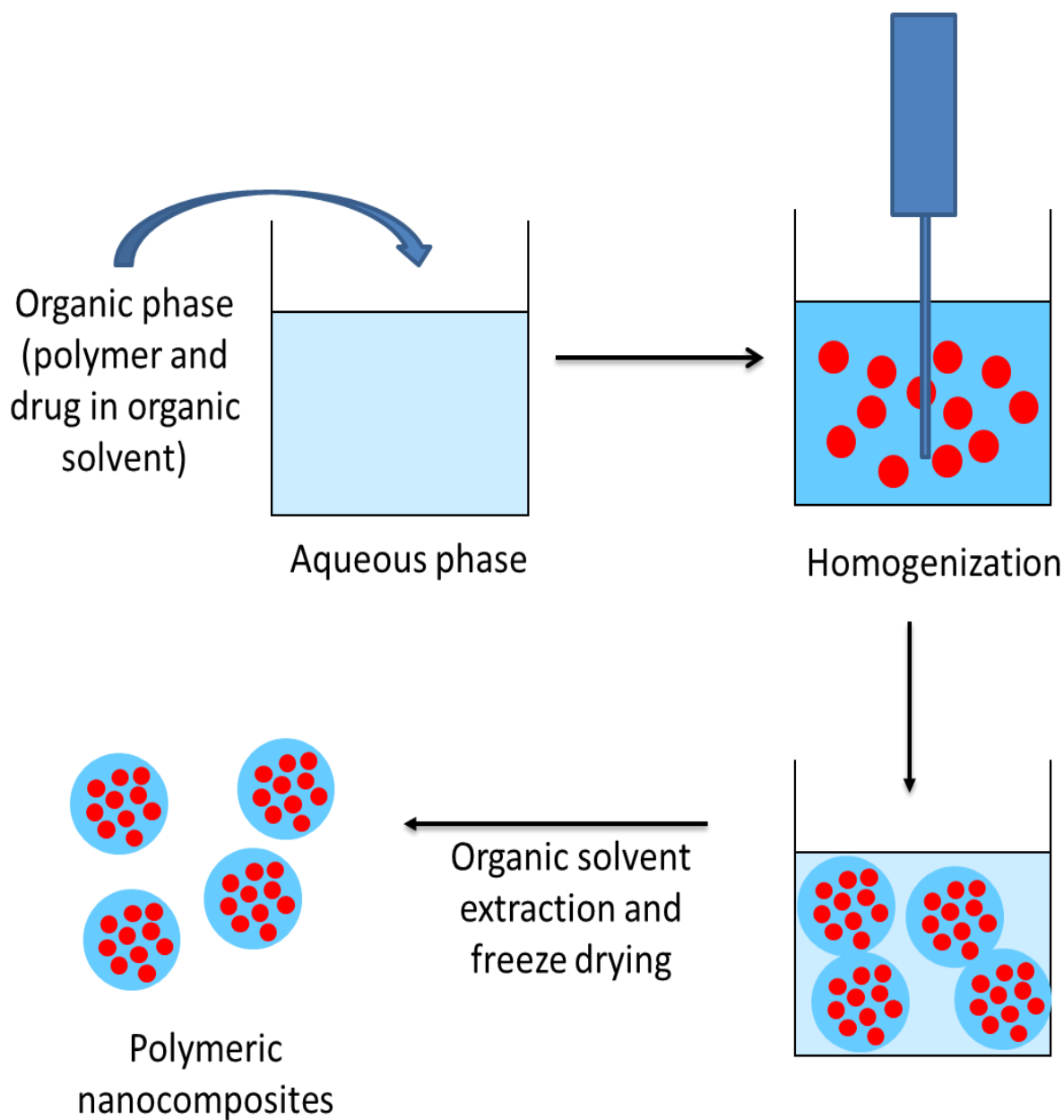
Figure 1-5: Schematic representation nanocomposite preparation by oil-in-water emulsion

1.7.3.2.Double emulsion (w/o/w) technique

Double emulsion technique is most often used to encapsulate hydrophilic compounds. The initial step of the double emulsion technique is the formation of water-in-oil (w/o) emulsion. The hydrophilic agent is dissolved in small volume of aqueous phase and this is emulsified in an organic phase containing the polymer. The w/o emulsion formed is further dispersed into larger volume of aqueous phase to form the double w/o/w emulsion.[93,94] The w/o/w emulsion formed is sonicated or homogenized for droplet size reduction. The size reduction carried out under strong shear stress has to be carried out carefully to minimize the hydrophilic drug diffusion to the external aqueous phase. The final step is the evaporation of the organic solvent which is carried out under vacuum to avoid polymer and component damage. The important parameters that need to be considered are: type and concentration of the polymer used, surfactant nature, polymer/surfactant ratio, solvents used, shear stress applied, evaporation and most important the ratio of the first/second phase.

The main drawback of the double emulsion technique is the large particle size and low entrapment efficiency of the drug.[93,95] The mechanism responsible for the poor entrapment efficiency is the diffusion of the hydrophilic active agent through the organic phase. Also, the application of intense shear stress may cause degradation of the drug component.[93]

1.7.4.Salting out technique
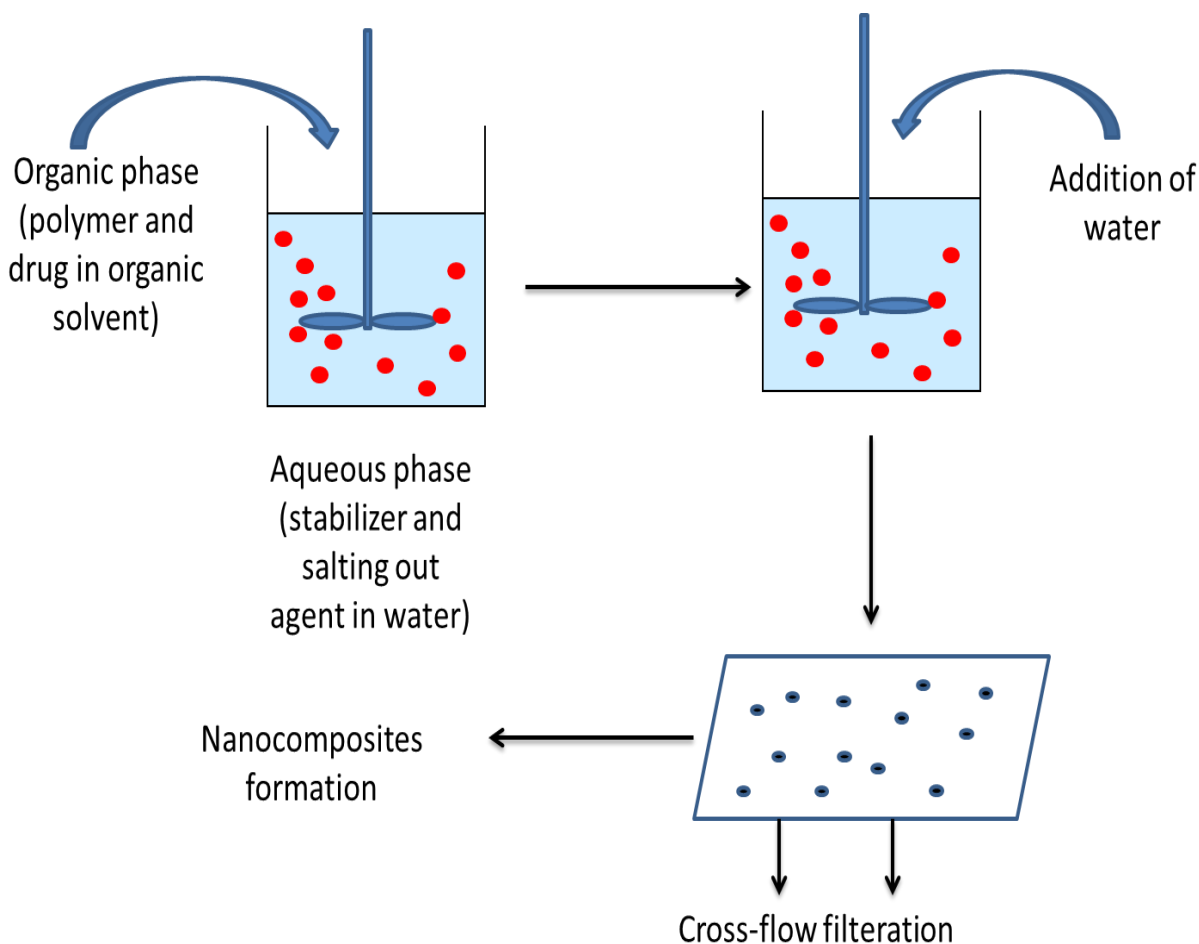
Figure 1-6: Schematic representation of nanocomposites preparation by salting out technique

In the salting out technique the polymer of choice and the active component are dissolved in water miscible solvents such as acetone, ethyl acetate or tetrahydrofuran. This organic solution is emulsified under vigorous mechanical stirring in an aqueous phase containing high concentration of the salting out agent and the colloidal stabilizer. This o/w emulsion is diluted with sufficient volume of water, under mild stirring. This reduces the ionic strength of the solution leading to the diffusion of the water miscible solvent into the aqueous phase, inducing the nanocomposites formation. The final step is the purification by cross-flow filtration to

remove the salting out agent.[96,97] Common salting out agents used are electrolytes like sodium chloride, magnesium chloride or magnesium acetate and non-electrolytes like sucrose.[96] Figure 1-6 represents the schematic representation of the salting out technique for nanocomposite preparation. Important parameters to be considered are: molecular mass and concentration of the polymer used, mechanical stirring rate and time, nature of surfactant use, nature of the salting out agent used, type of water miscible solvent.

The main drawback of the salting out technique is the requirement of and added purification step for the removal of the salting out agent used which is in high concentrations. Also the salts used are at times not compatible with the active agents. Furthermore, this technique is suitable for the encapsulation of the lipophilic drugs only.[98]

1.7.5. Nanoprecipitation technique

In the nanoprecipitation technique the polymer and the active agent are dissolved in a water miscible organic solvent such as acetone or ethyl acetate. The organic phase is then slowly poured in a controlled manner into an aqueous phase containing the surfactant such as PVA or poloxamer 188 under mild stirring. Nanocomposites are instantaneously formed due to immediate reduction of the interfacial tension with rapid diffusion of the water miscible into the aqueous phase. The organic solvent is removed by evaporation and the nanocomposite suspension is concentrated under reduced pressure, centrifuged and freeze dried to obtain nanocomposites.[99,100] Important parameters to be considered are: polymer concentration, nature of the surfactant used, polymer/surfactant ratio, nature of the solvent used, and the phase addition.[100]

Nanoprecipitation technique is only suitable for hydrophilic agents because of their poor interaction with the polymer which leads to a considerable leakage of the drug into the aqueous phase during preparation. Also, the active agent to be encapsulated needs to be highly soluble in the polar solvent and slightly soluble in water.[101]

1.7.6. Spray drying
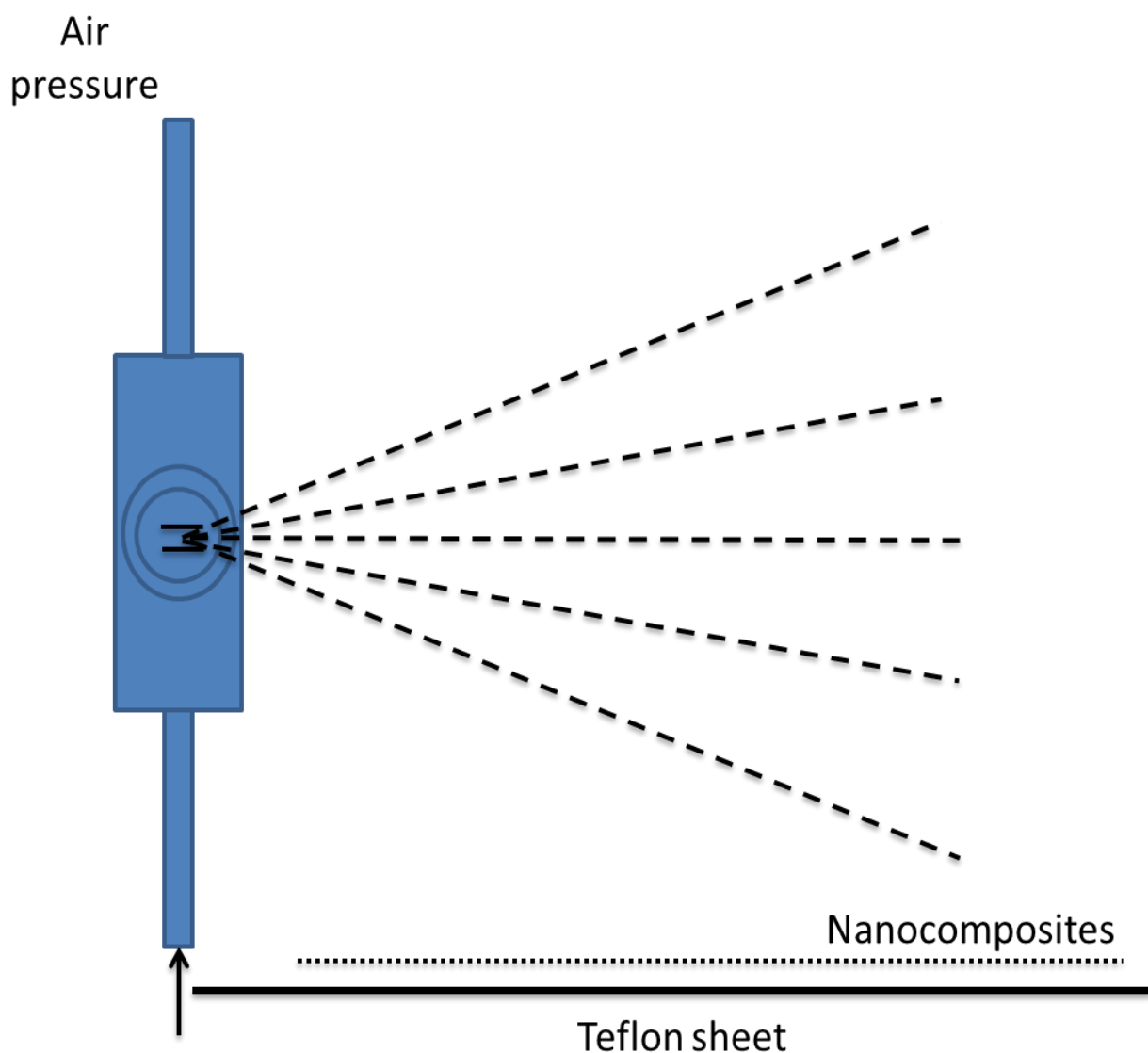
Figure 1-7: Schematic representation of nanocomposite preparation by the spray drying technique

Spray drying technique enables the transformation of feed from a fluid state into dried particulate form by spraying the feed into a hot drying medium. It is a continuous particle processing drying operation as shown in Figure 1-7. The feed can be a solution, suspension, dispersion or emulsion. The dried product can be in the form of powders, granules or agglomerates depending upon the physical and chemical properties of the feed, the dryer design and final powder properties desired. Large batch sizes are typically required as compared to emulsion techniques; therefore spray drying technique is often problematic.

1.8. Targeted drug delivery of the polymeric nanocomposites to the tumor sites

There are several targeting strategies that can be used to concentrate nanocomposites selectively at tumor sites by exploiting differences between malignant and normal cells. The two main drug targeting strategies employed are- passive targeting and active targeting.[18]

1.8.1. Passive targeting:

Passive targeting takes advantage of the anatomical difference between the normal and tumor tissues to deliver the drug at the tumor site. As the tumor grows (~2mm in diameter) the normal tissues are displaced. The growing tumor activates the angiogenic process, to generate new blood vessels towards the tumor to supply oxygen and nutrients. The newly formed tumor blood vessels vasculature is very different from normal blood vessels, as they are dilated, irregular in shape and leaky or defective due to poorly organized endothelial cells.[21] The disorganized pathology of angiogenic tumor vasculature with a discontinuous endothelium leads to hyperpermeability to circulate the nanocomposites and lack of effective tumor lymphatic

drainage leads to subsequent accumulation of the nanocomposites. This increased permeability of the tumor vasculature is the key feature in passive targeting of the nanocomposites. This is popularly known as enhanced permeability and retention effect (EPR) which results in the accumulation of macromolecular drugs and polymeric nanocomposites at the tumor site and thus increasing the drug concentration.[3,102] By taking the advantage of the EPR effect the DDS can progressively but selectively build up within the tumor cells and deliver drugs with higher drug concentrations compared to the normal cells. Figure 1-8 illustrates the enhanced delivery of the drug through the ERP effect with less normal cell targeting.

Localized delivery is another approach in which the drug loaded nanocomposites can be directly delivered to the target site thus minimizing the circulation of the drug and lowering toxicity.[25] This method is only suitable for the tumors that are easily accessible.
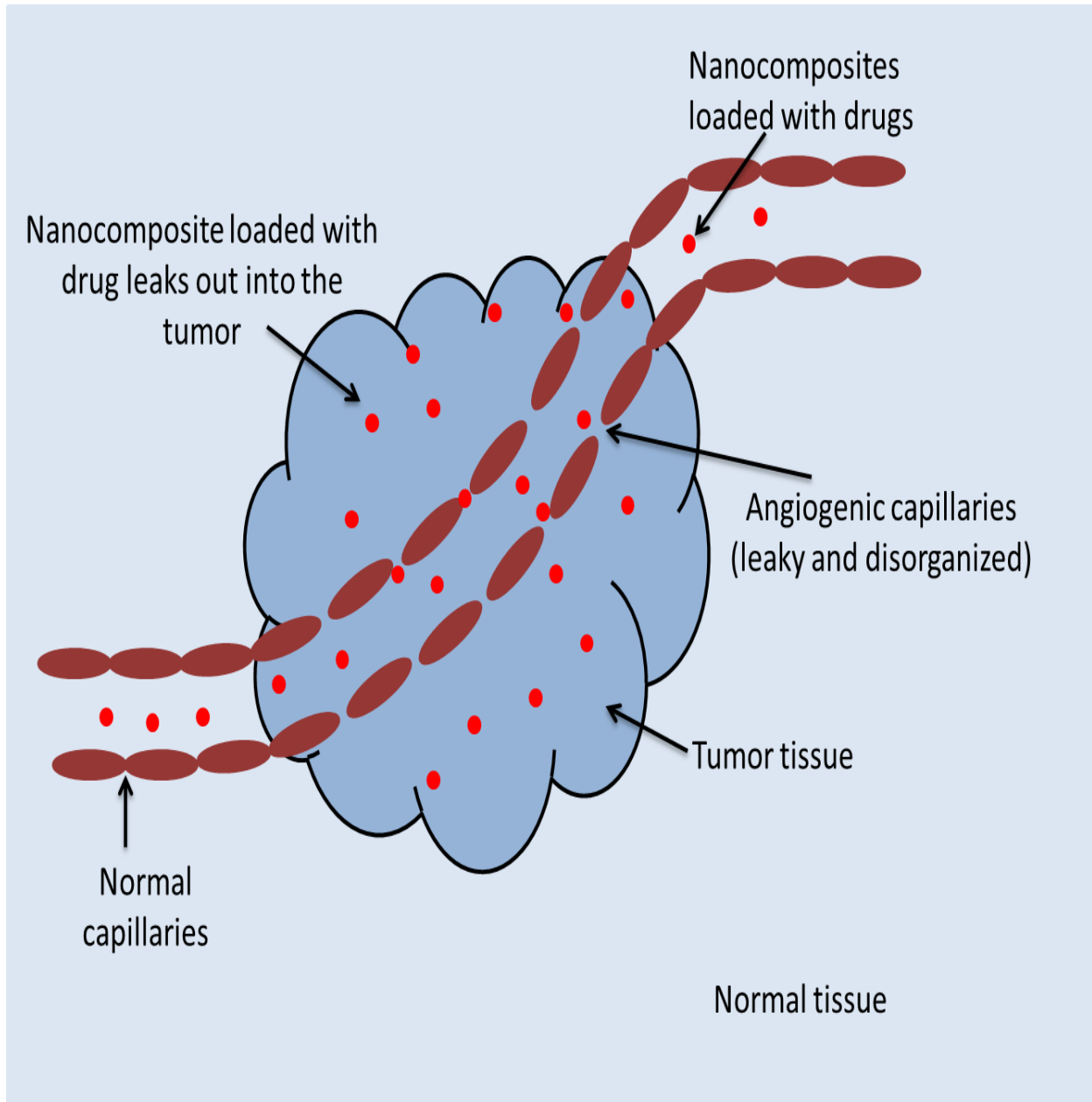
Figure 1-8: Illustration of the passive targeting approach with enhanced delivery of the drug to the tumor site due to the ERP effect

1.8.2. Active targeting:

Active targeting strategy exploits the specific binding affinities of targeting ligands that are bound to the nanocomposite system used to bind to the target site receptor functionalities, thereby allowing preferential accumulation of the drug within the tissue or cells.[3,18,102] This strategy also takes the advantage of the EPR effect for the accumulation of the nanocomposites into the interstitial fluid of the tumor and is illustrated in Figure 1-9. The main parameter to be kept in mind is the proper selection of the targeting agent, which should be available in abundance, should have high affinity and selectivity of binding to the cell surface and should be apt to chemical changes on conjugation. The identity and characteristics of the targeting agent are also important for longer circulation time, cellular uptake, affinity, and removal of the nanocomposite. Therefore, a specific binding capacity of the targeting agent to tumors is essential in the success of the drug delivery system. An increased site specificity and internalization can improve the efficacy of treatment and decrease the possibility of the serious side effects. Ligands such as antibodies, saccharides, aptamers, hormones, lectins and low molecular compounds binds to their specific receptor on the cellular surface and trigger the internalization process of the drug by means of receptor-mediated endocytosis (REM). Surface receptors like folate receptor (FR), the transferrin receptor (TfR) and the epidermal growth factor reseptor (EGRF) have been highly investigated for site specific targeting.[103-105]
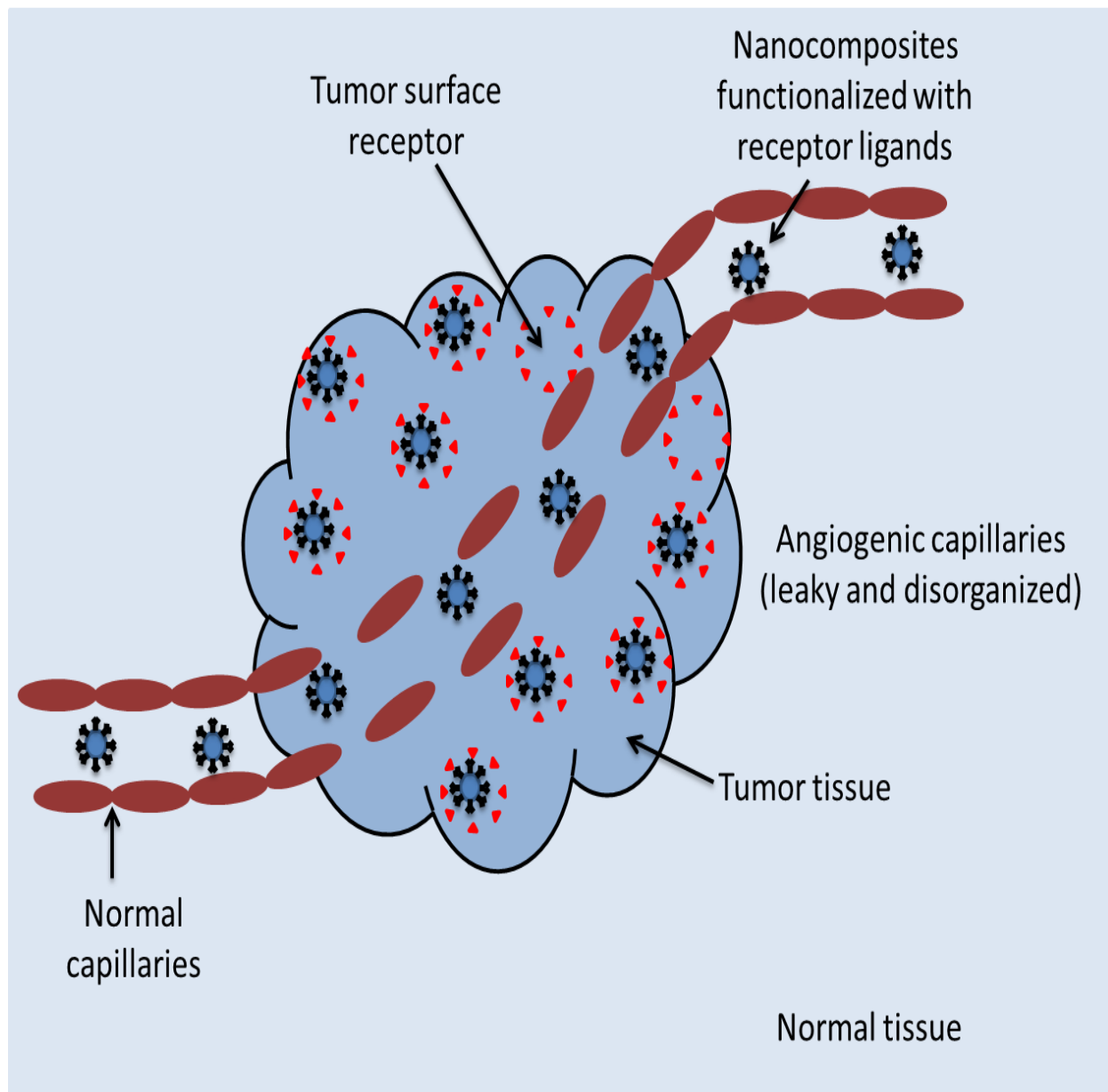
Figure 1-9: Active targeting strategy for the delivery of drugs through ligand-receptor interaction.

1.9. Folate receptor

Folic acid (FA) also known as folate or vitamin B9 is a low molecular weight (MW-441) water soluble vitamin required by all living cells for nucleotide biosynthesis and for normal metabolic maintenance of 1-carbon pathways. Cellular uptake of folates are facilitated by either a low affinity reduced folate carrier which is present in virtually all cells of the body, or a

high affinity folate receptor (FR) which exhibits highly limited distribution within the body cells. The folate receptor is a 38 kDa glycosyl-phosphatidylinositol-anchored glycoprotein that has the affinity for both folic acid and folate linked cargos. [106] Two membranous forms of FR-alpha (α) and beta (β) have been identified. Both α and β forms have high FA binding affinity, however they display some difference with respect to their affinity for antifolates.[107,108] The reduced folate carrier is selective in facilitating transport of reduced forms of folic acid only while the FR has the ability to transport both folic acid and folate-linked cargos. Once the folate linked cargos are conjugated to the cell surface FR they are internalized into the cells through a process called receptor-mediated endocytosis.
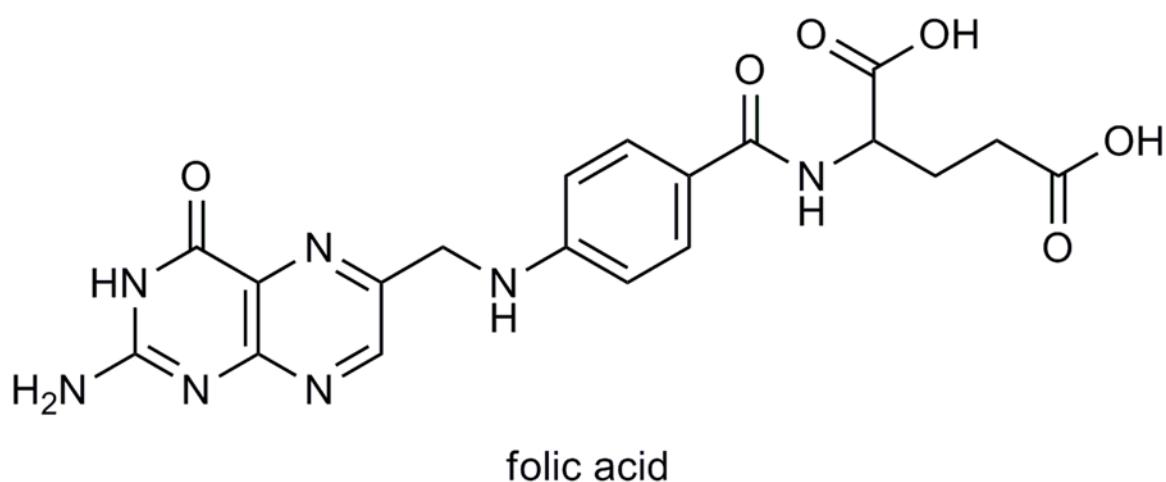
folic acid

Figure 1-10: Structure of Folic acid

It has been found that FR is up-regulated in more than 90% of non-mucinous ovarian carcinomas. It is also found at high to moderate levels in kidney, brain, lung, and breast carcinomas while it occurs at very low levels in most normal tissues. The FR density also appears to increase as the stage of the cancer increases.[18,106] In addition, folic acid is required for essential cell function, therefore the cargo attached to the ligand are retained within an endocytic vesicle. While, the cargos attached to antibodies, hormones, and other related ligands

are normally internalized to clear the ligand from the receptor. Exploiting the above-mentioned facts, it can be hypothesized that **folic acid conjugation to polymeric nanocomposites will improve drug selectivity and decrease negative side effects.** Folic acid has emerged as an attractive ligand for drug targeting due to its low molecular size, which allows for good tissue penetration. The structure of folic acid (FA) is shown in Figure 1-10. Also folic acid can be easily attached to the polymeric composites through carbodiimide chemistry and will be discussed in detail in chapter 6.

1.10. Summary of Objectives

The overall goal of this dissertation work is to develop and design a novel controlled release drug delivery system (DDS) with imaging and therapeutic capabilities. The polymeric coating used helps reduce the toxicity of the active agent. Some of the main objectives of this dissertation work are:

1. Study the synthetic variation upon encapsulation of the magnetic iron/iron oxide nanoparticles by synthetic polymer. Also, study the dilution effect of the saturation magnetization of the iron/iron oxide nanoparticles due to the polymer coating.

2. Develop nano sized mono-dispersed biodegradable poly (lactic-co-glycolic acid) (PLGA) composites containing the iron/iron oxide nanoparticles as dual modal imaging and therapeutic drug delivery carrier.

3. Study the release of the drug analog from the magnetic polymeric composites upon heating due to magnetic hyperthermia phenomenon with electromagnetic radiations.

Chapter 2. Characterization techniques

2.1. Introduction

The characterization of the synthesized nanomaterials is a very important stage for the advancement of quality scientific research. From the development of the nanomaterial's synthesis technique to the quality control testing of the already established techniques, characterization of the nanomaterial is essential. The characterization of the material aids in the precise identification of phases, size, morphology, material impurities, and surface chemistry effects of the material. Characterization of the nanomaterials synthesized plays an important role in the scientific research development; hence this chapter will be focused on some of the principal characterization techniques used in this research work.

Characterization technique	Application
X-ray Diffraction (XRD)	Phase Composition, crystal shape and crystallite size
Scanning electron microscopy (SEM) and Transmission electron microscopy (TEM)	Nanomaterial size and morphology
Thermogravimetric analysis (TGA)	Mass change in materials associated with dehydration, decomposition, and oxidation
Vibrating sample magnetometry (VSM)	Magnetic property and corecivity measurements
Fluorescence spectroscopy	Track (bio-) chemical reactions
Fourier transform infrared spectroscopy (FTIR)	Functional group analysis
Ultraviolet-visible spectroscopy (UV-vis)	Characterization and quantitative determination of analytes

Table 2-1 Principal characterization techniques used

2.2. X-ray Diffraction (XRD)

X-ray powder diffraction (XRD) is an instrumental technique that is used to identify crystalline materials and it is a fast and a reliable tool for material identification. X-rays are electromagnetic radiation with energies in the range of 100 eV - 100 keV. For diffraction applications, only short wavelength x-rays (hard x-rays) in the range of a few angstroms to 0.1˚A are used. As the wavelength of x-rays is equivalent to the size of atoms, they are ideally suited for probing the structural arrangement of atoms and molecules in a wide range of materials. The energetic x-rays can penetrate deep into the materials and provide information about the bulk structure. X-rays primarily interact with electrons in the atoms. When x-ray photons collide with sample, a portion of the beam will be scattered in all directions from the material and constructively interfere in distinct directions based upon the symmetry of the repeating crystal structure associated with the sample material. The angle where the peaks in the x-ray diffraction spectrum occur is given by Bragg's law (Eq.2.1):

$$n\lambda = 2d_{(hkl)}\sin\theta \qquad\qquad 2.1$$

Where λ is the wavelength of the x-ray beam, $d(hkl)$ is the spacing between the (hkl) crystallographic plane contributing to the diffraction peak, θ is the angle of incident x-ray, and *n* is an integer for the order of reflection. This phenomenon creates diffraction patterns as you scan the incident angles, which are typically reported and graphed as 2θ. This diffraction patterns have been calculated and experimentally tabulated into data bases for easier matching and sample crystal structure determination. Figure 2-1 represents the diffraction of the x-rays by plane of atoms. It is important to note that the d-spacing provides a unique fingerprint of the sample materials under investigation.
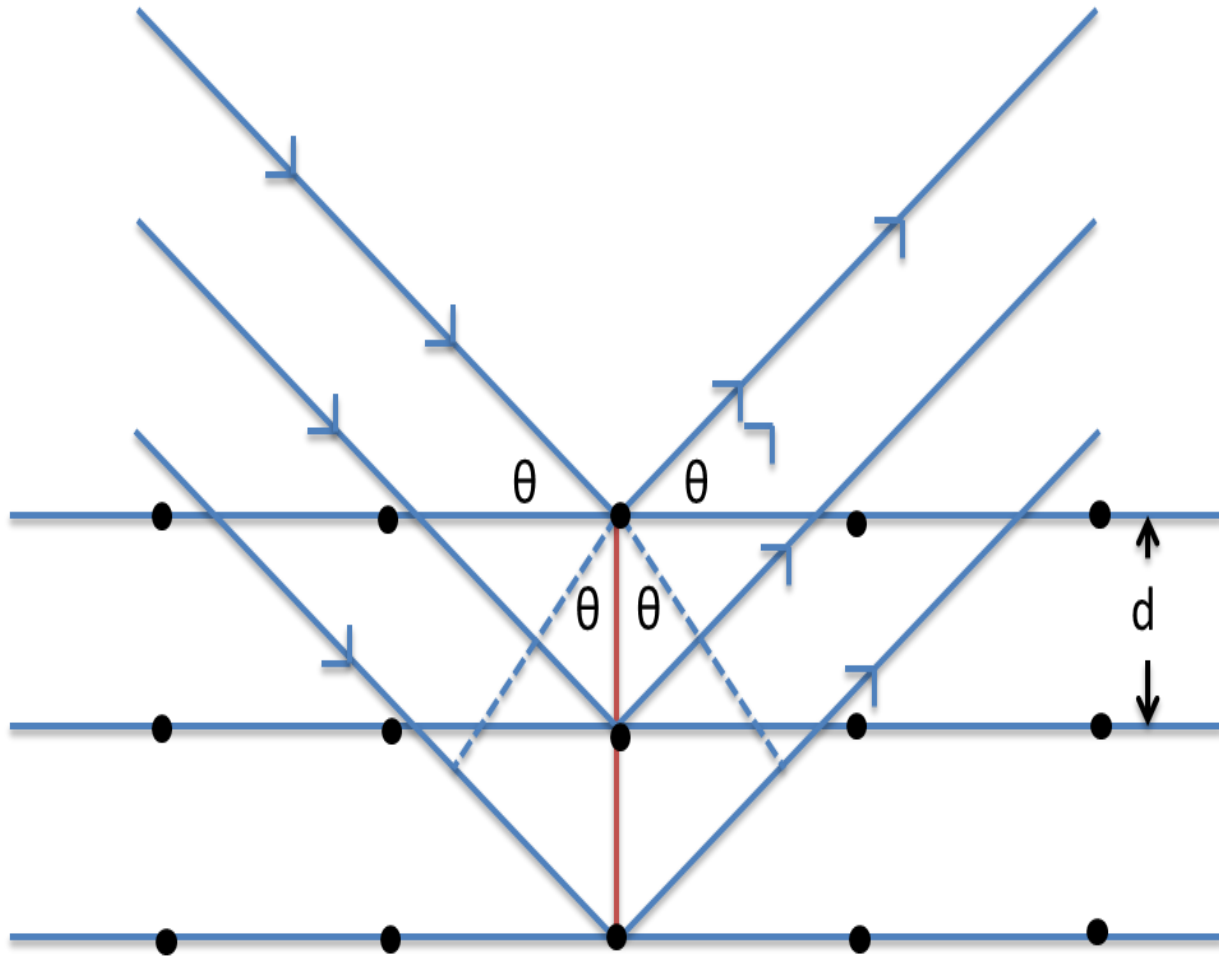
Figure 2-1: Diffraction of the x-rays by plane of atoms

The primary application of XRD is to investigate the structural nature of the material, for example, the size and crystallinity of the sample material. A material's structural nature can be crystalline or amorphous. In crystalline materials a higher degree of constructive interference will occur, thereby producing sharp constructive diffraction lines in the XRD pattern. While in amorphous materials there are edges, mild distortions, and finite crystalline planes that will cause a broadening affect in the diffraction pattern. There are many factors that may also contribute to the broadening of diffraction lines, for example, instrumental broadening, micro-strain (lattice strain), powder inhomogeneity, and temperature. Broadening in the diffraction pattern can also

occur with a reduction in particle or crystallite size. Peak width due to crystallite size varies inversely with crystallite size. So as the crystallite size gets smaller, the peaks get broader. Paul Scherrer, first observed that small crystallite size could give rise to peak broadening. He derived a well-known equation for relating the crystallite size to the peak width, which is called the Scherrer formula (Eq.2.2)

$$B(2\theta) = \frac{K\lambda}{L cos\theta} \qquad\qquad 2.2$$

For this equation, λ is wavelength of the incident x-ray and θ is the angle of the incident x-ray obtained from the center of the diffraction peak, B refers to the peak width, typically referred to as the full width at half maximum (FWHM) of the diffraction peak, L the crystallite size and K is the Scherrer constant, typically 0.94 for spherical particles with cubic symmetry. The Scherrer equation is limited to nano-scale particles and is not applicable to grains larger than about 0.1 μm. A small impurity in a sample is enough to overwhelm the diffraction pattern and gives a size value much larger than would be representative of the majority of the sample in question. This is a major reason that other particle size determining methods such as TEM, SEM are required for nanomaterials research. Another reason for utilizing other size determining methods is that only crystalline materials are apparent in the XRD diffraction pattern. This means that amorphous regions, say on the surface of nanoparticles would not be included in the sizes determined by XRD. Also band broadening becomes a major factor in nanoparticles research. Even for crystalline materials, once below 5-10 nm the diffraction pattern peaks appear more as broad humps than spikes. As the peaks broaden it becomes more difficult to separate the background, sample, and impurities.
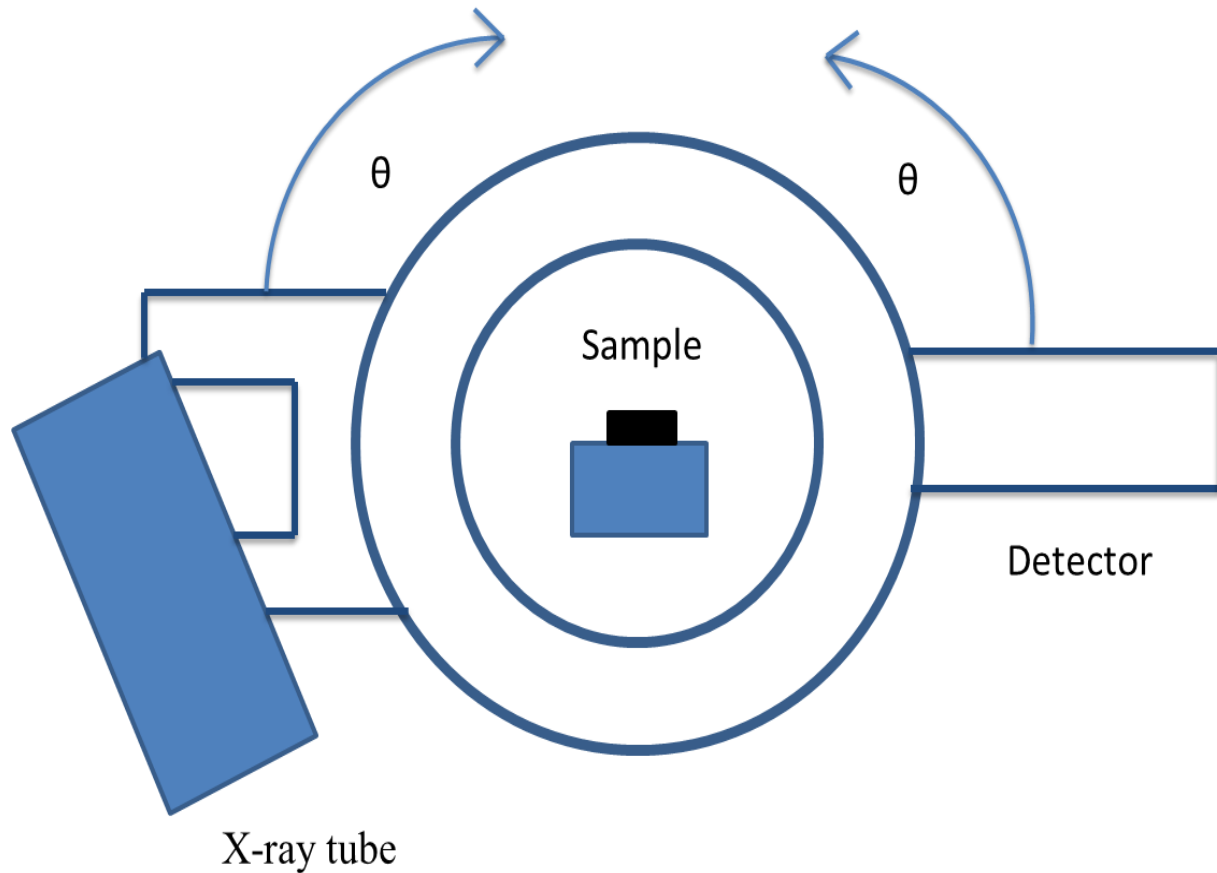
Figure 2-2: Schematic representation of the X-ray diffractometer

Figure 2-2 shows the schematic of the θ: θ x-ray diffractometers. In the θ: θ x-ray diffractometers the sample is stationary in the horizontal position, and the X-ray tube rotates at a rate -θ°/min and the detector rotates at a rate of θ °/min. The other type of x-ray diffractometer is θ: 2θ in which the X-ray tube is stationary, the sample moves by the angle θ and the detector simultaneously moves by the angle 2θ. The drawback of θ: 2θ x-ray diffractometer is that at high values of θ small or loosely packed samples may have a tendency to fall off the sample holder. In the commercial x-ray diffractometer the X-rays are generated from an X-ray tube under vacuum when the filament within the tube is heated by the application of a current. The numbers of electrons emitted from the filament are directly related to the amount (voltage) of the

applied current. The high voltage accelerates the electrons towards a target, typically made of copper or molybdenum; the wavelength of the X-ray is dependent on the type of the target. Next, these x-rays are directed towards the finely ground sample and finally, the detector detects the signal which will be processed either electronically or by microprocessor to a count rate.

For the purposes of this work, powder X-ray diffraction (XRD) was taken on a Panalytical X'pert pro diffractometer. A copper anode was used as the source of x-rays with a current of 45 mA at an accelerating voltage of 40 kV. As described previously, the copper source emits x-rays with Kα1 and Kα2 wavelengths of 1.540 ˚A and 1.544 ˚A respectively. The dried powder samples were gently ground using a mortar and pestle and then pressed onto a zero background, low volume silicon sample holder. The sample holder was then placed in the instrument for XRD analysis. Upon completion of the run, the data were analyzed in the Highscore plus program, which has a built-in diffraction library to compare the samples diffraction pattern to the diffraction patterns in the JCPDS-ICDD database. XRD was used for phase identification, identifying the purity of samples, and determining the crystallinity of products.

2.3. Scanning electron microscopy (SEM)

Scanning electron microscope (SEM) uses a focused beam of high-energy electrons to generate a variety of signals at the surface of solid sample. The signals derived from electron-sample interactions reveals information about the sample including external morphology (texture), chemical composition, and crystalline structure and orientation of materials making up the sample. The combination of higher magnification, larger depth of focus, greater resolution, and ease of sample observation makes the SEM one of the most heavily used instruments in research areas today.
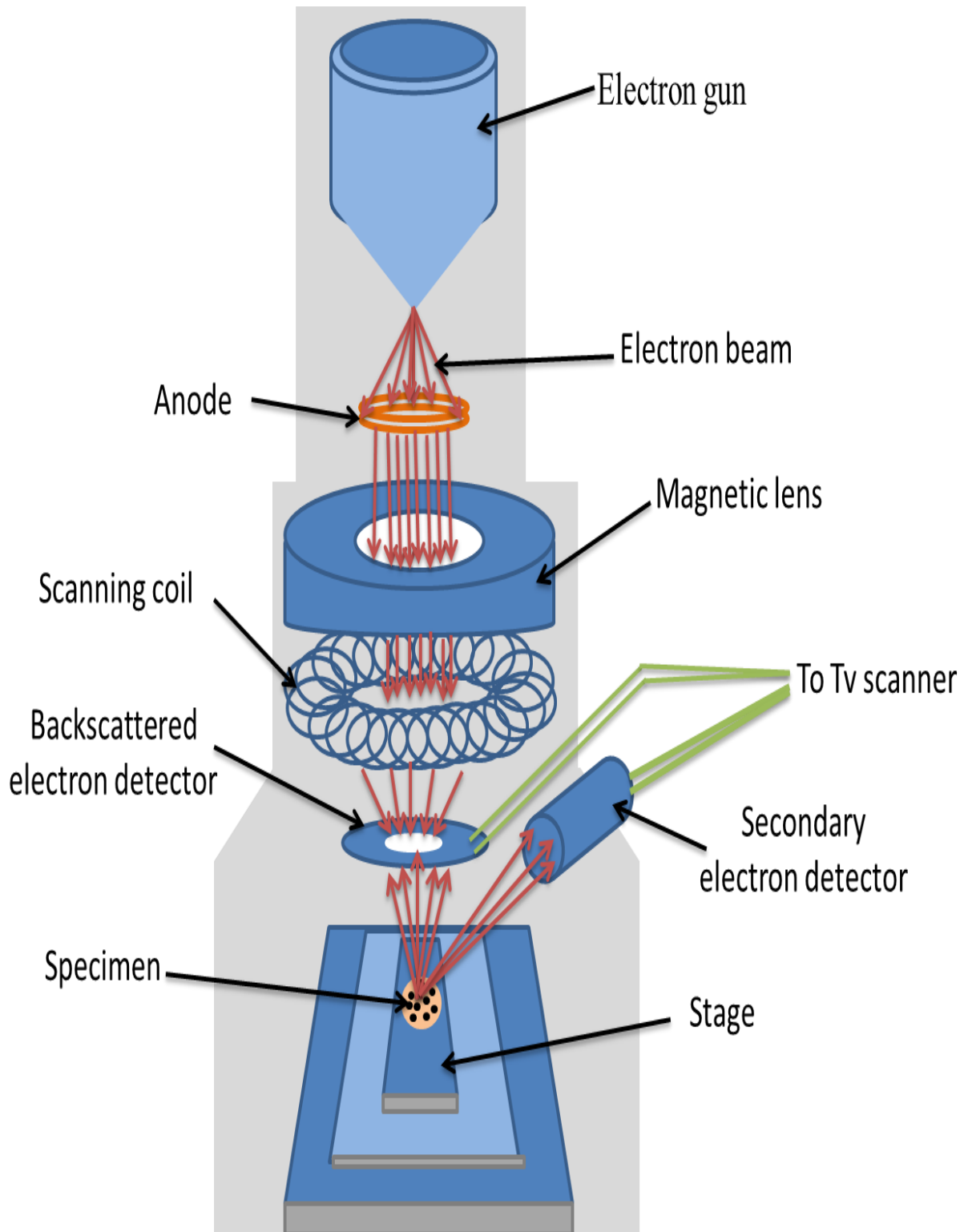
Figure 2-3: Schematic of the main components of SEM

Figure 2-3 shows a schematic of the main components of the SEM. The electron beam, which typically has an energy ranging from 0.5 keV to 40 keV, is focused by one or two magnetic lenses to a spot about 0.4 nm to 5 nm in diameter. The beam passes through pairs of scanning coils or pairs of deflector plates in the electron column, which deflect the beam in the x and y axes so that it scans in a raster fashion over a rectangular area of the sample surface. The electron beam interacts with the sample and emits out a variety of signals. These signals include secondary electrons (SE) which are emitted from the surface as they are knocked out of the valence orbitals of the surface atoms, backscattered electrons (BSE) which are scattered off the surface, and photons (characteristic X-rays that are used for elemental analysis and continuum X-rays) as depicted in Figure 2-4

The secondary electrons are used to create an image of the surface, which has a 3D quality as the angle of the secondary electron projection depends on the angle of the incoming beam. Thus steep surfaces and edges tend to be brighter than flat surfaces, which results in images with a well-defined 3D appearance. A backscattered electron profile is also collected as the number of backscattered electrons increases with atomic number, so atoms of a higher atomic number appear brighter in the image. The photons are produced by inelastic collisions of the incident electrons with electrons in discrete orbitals (shells) of atoms in the sample. As the excited electrons return to lower energy states, they yield X-rays that are of a fixed wavelength. Thus, characteristic X-rays are produced for each element in sample material that is "excited" by the electron beam. The SEM is routinely used to generate high-resolution images of shapes of objects and to show spatial variations in chemical compositions. Precise measurement of very small features and objects down to 50 nm in size can be accomplished using the SEM. Also the SEM analysis is considered to be "non-destructive"; that is, x-rays generated by electron

interactions do not lead to volume loss of the sample, so it is possible to analyze the same materials repeatedly.
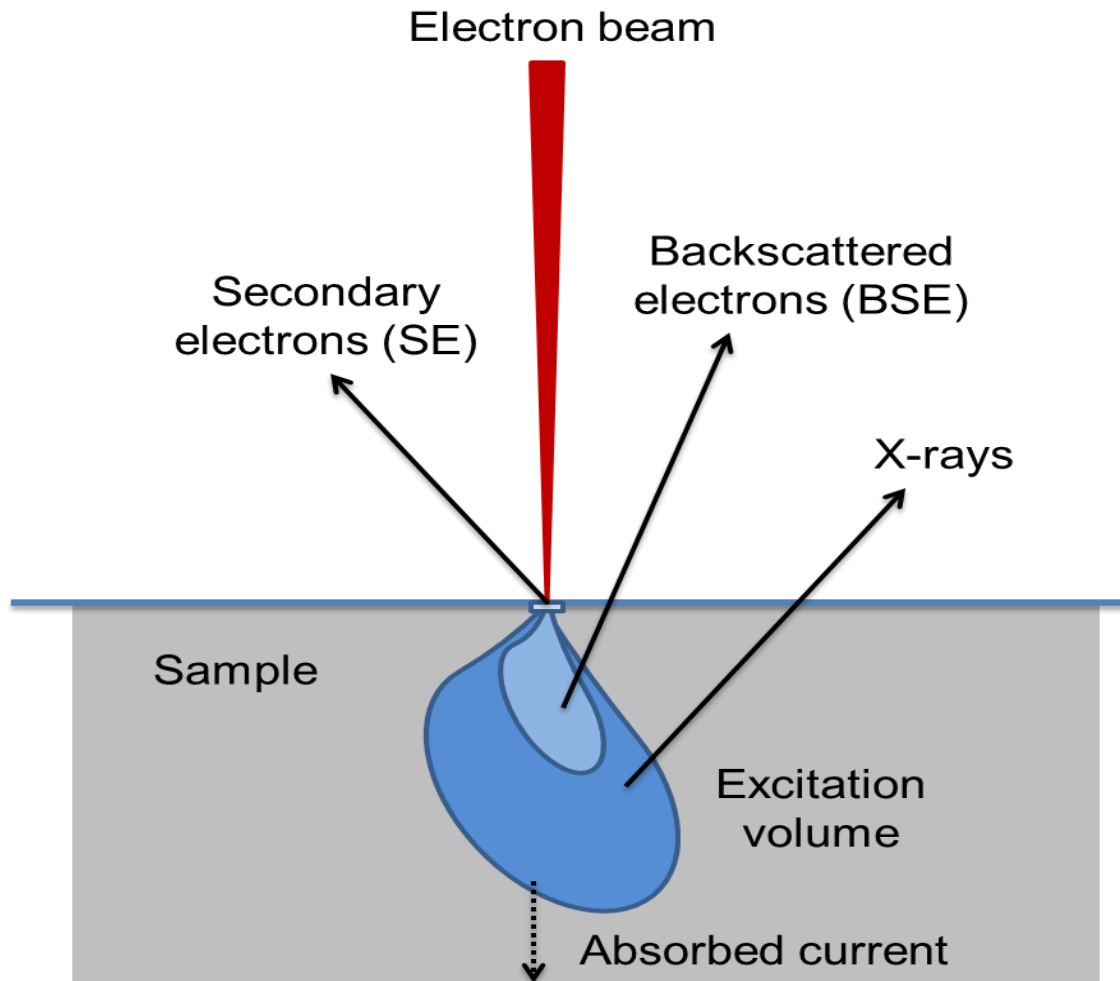
Figure 2-4: Origin and information depth of secondary electrons (SE), backscattered electrons (BSE), and x-rays in the diffusion cloud of electron beam into the sample

In this research work the size, size distribution, and morphology of the samples were determined using Hitachi SU-70 field emission scanning electron microscope (SEM) equipped with digital image acquisition, EDX, WDX, EBSP, STEM, BSE, CL detectors. The morphology of the nanomaterial sample is represented in the SEM image by dark and grey areas. The contrast is due to the interaction of the electron beam with the sample. The SEM samples are

prepared by lightly sprinkling the powdered sample on a conductive carbon tape mounted on the sample holder. The sample is then lightly pressed to seat and then sprayed with canned air to remove any loose sample from top. The sample was then sputtered with gold to make it conductive and reduce charging. Charging is a buildup of excess of electrons (charge) on the surface of the non-conductive sample, which causes an undesired electron beam deflecting leading to an increase in the brightness of the image. The sample holder is then placed in the sample compartment of the microscope and the images are obtained as described above.

SEM can provide precise resolution around ±50 nm and has ±200,000 X resolution power, but for nanoparticle research higher resolution up to few angstroms is desirable. For this purpose transmission electron microscopy (TEM) is utilized which has a resolution around ± 0.2 nm. Both TEM and SEM utilize electron beams to detect the size and morphology of sample materials. In a SEM image is produce from electrons detected after scattering off the surface of the sample where as in a TEM image is produced by electrons passing through the sample placed on a grid. The electron density of the solid nanomaterial sample scatters some of the electrons, with the remaining electron beam passing by to produce a silhouette of the material on a screen for imaging. The TEM image provides information about the size, shape, size distribution, and uniformity. Also the core-shell nature of the nanomaterial sample can also be determined by the difference in the electron density. High resolution TEM can see lattice fringes and can be used for electron diffraction which will give insight into the crystal structure similar to XRD. In this work the TEM was performed on Carl Zeiss Libra 120 Plus Field Emission Transmission Electron Microscope (TEM) to evaluate the size and morphology of the synthesized nanoparticles.

2.4. Thermogravimetric analysis (TGA)

Thermogravimetric analysis (TGA) is an instrumental technique where in the mass of the sample in a controlled atmosphere is recorded continuously as a function of temperature or time as the temperature of the sample is increased linearly with time. The thermogravimetry instrument consists of a sensitive analytical micro balance, furnace, purge gas system for providing an inert atmosphere and a computer and processor for instrument control and data recording. Figure 2-5 represents the schematic representation of the components of a thermal gravimetric balance.

TGA provides quantitative measurement of mass change in materials associated with transition and thermal degradation. TGA records change in mass from dehydration, decomposition, and oxidation of a sample with time and temperature. The most important application of thermogravimetric technique is found in the study of polymers. Thermograms provide information about the decomposition mechanism for various polymers. Also the uniformity in the polymer can be known. A tactic polymer would have fewer number of decomposition events as compared to an atactic polymer. The application of TGA in nanomaterial research is to determine the amount of organic ligands/impurities that are adsorbed onto a nanoparticle surface formed during the synthesis procedure. This percentage of organics associated with the total mass of the nanoparticle is important information for magnetization mass correction as it is dependent on the mass of the magnetic material and not the total mass of the system. It also provides information about the mass percentage of the organics in the sample. This information can give indication of how well a surface is coated with a functional ligand, and in some way give insight to the surface area to volume ratio of the sample.
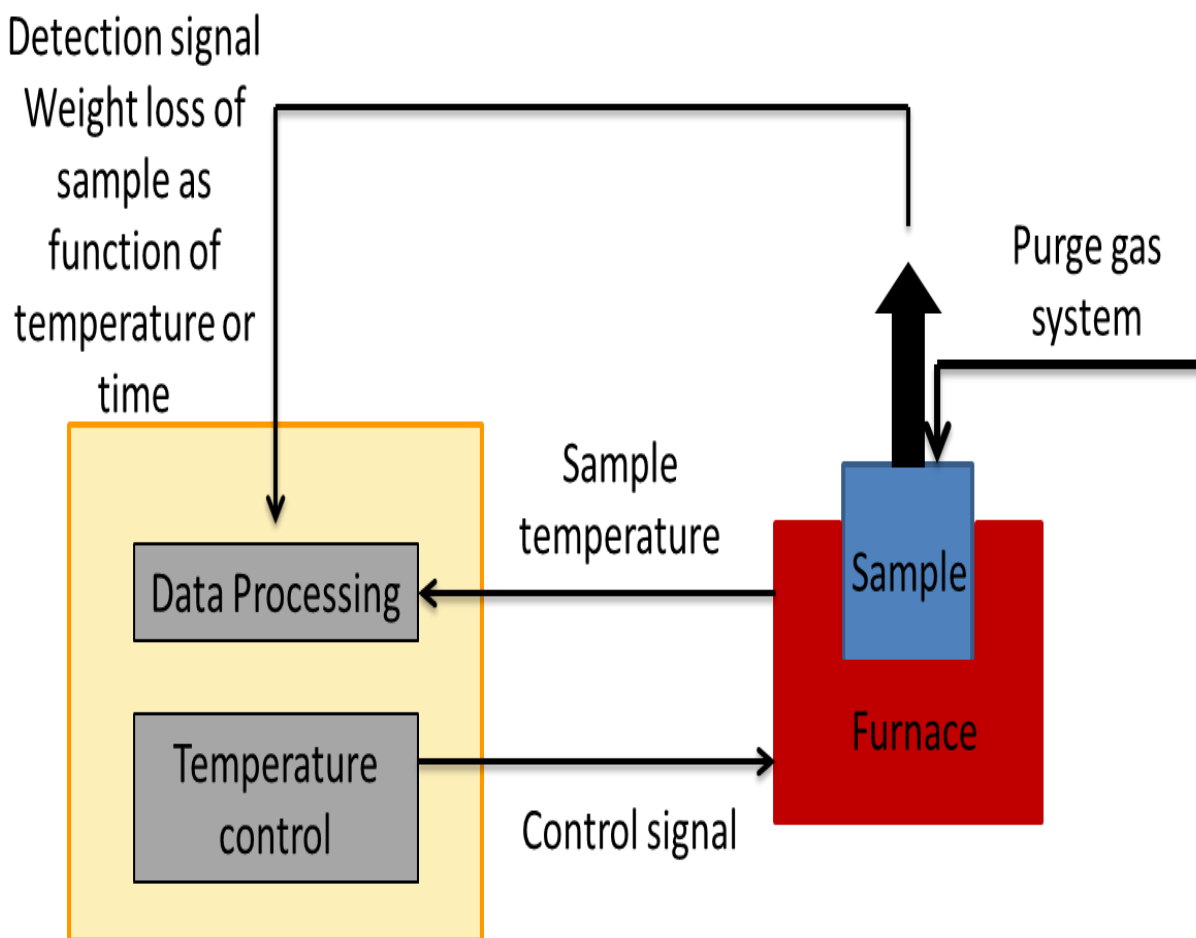
Figure 2-5: Block diagram of the Thermogravimetric analyzer

TGA also offers an easier way of annealing samples where in the sample size is critical. This use may not be as common, but has the advantage of working with smaller sample size than a traditional heating furnace, such as a tube furnace. It also allows for the monitoring of mass loss of a sample under different gaseous atmosphere. In this work the thermogravimetric analysis was performed on a TA instruments Q5000 thermogravimetrtic analyzer. The sample is positioned on a platinum pan that is supported on an analytical balance which located outside the furnace chamber. After the balanced is zeroed, the sample is heated and the weight signal is stored as a function of temperature and time.

2.5. Vibrating sample magnetometry (VSM)

The vibrating sample magnetometer is an analytical instrument employed for determining magnetic properties of a large variety of materials: diamagnetic, paramagnetic, ferromagnetic, ferromagnetic and antiferromagnetic. This experimental technique was invented in 1956 by Simon Foner, a scientist of the MIT. A vibrating sample magnetometer (VSM) operates on Faraday's Law of Induction, which states that a change in magnetic field will produce an electric field. This electric field can be measured and provides information about the changing magnetic field. As shown in Figure 2-6 VSM operates by first placing the sample in a constant magnetic field. If the sample is magnetic, this constant magnetic field will magnetize the sample by aligning the magnetic domains or magnetic spins with the applied field. If the sample vibrates in a sinusoidal motion, an electrical signal can be induced between two coils (pick-up coils) according to the Faraday's law. This electric signal has the same frequency of vibration and the amplitude is proportional to the magnetization of the sample. The produced current will be amplified and then using a computer interface that contains a specific software system, information about the magnetization of the sample and its dependence on the magnetic field could be obtained.

The ability to perform measurements at various temperatures is available for the VSM but the resolution and sensitivity is not comparable to that of the SQUID, and thus most of the VSM are set up to measure at room. The main advantage that the VSM offers to material research is that the measurements can be done much more quickly than using a SQUID, and do not require liquid He. A Lakeshore model 7300 room temperature vibrating sample magnetometer was used determine the magnetic properties of materials in this research work. The measuring field was oriented either parallel or perpendicular to the plane of the sample

depending on the sample shape i.e. for example pellets were oriented parallel, while powders were oriented perpendicular to the magnetic field.
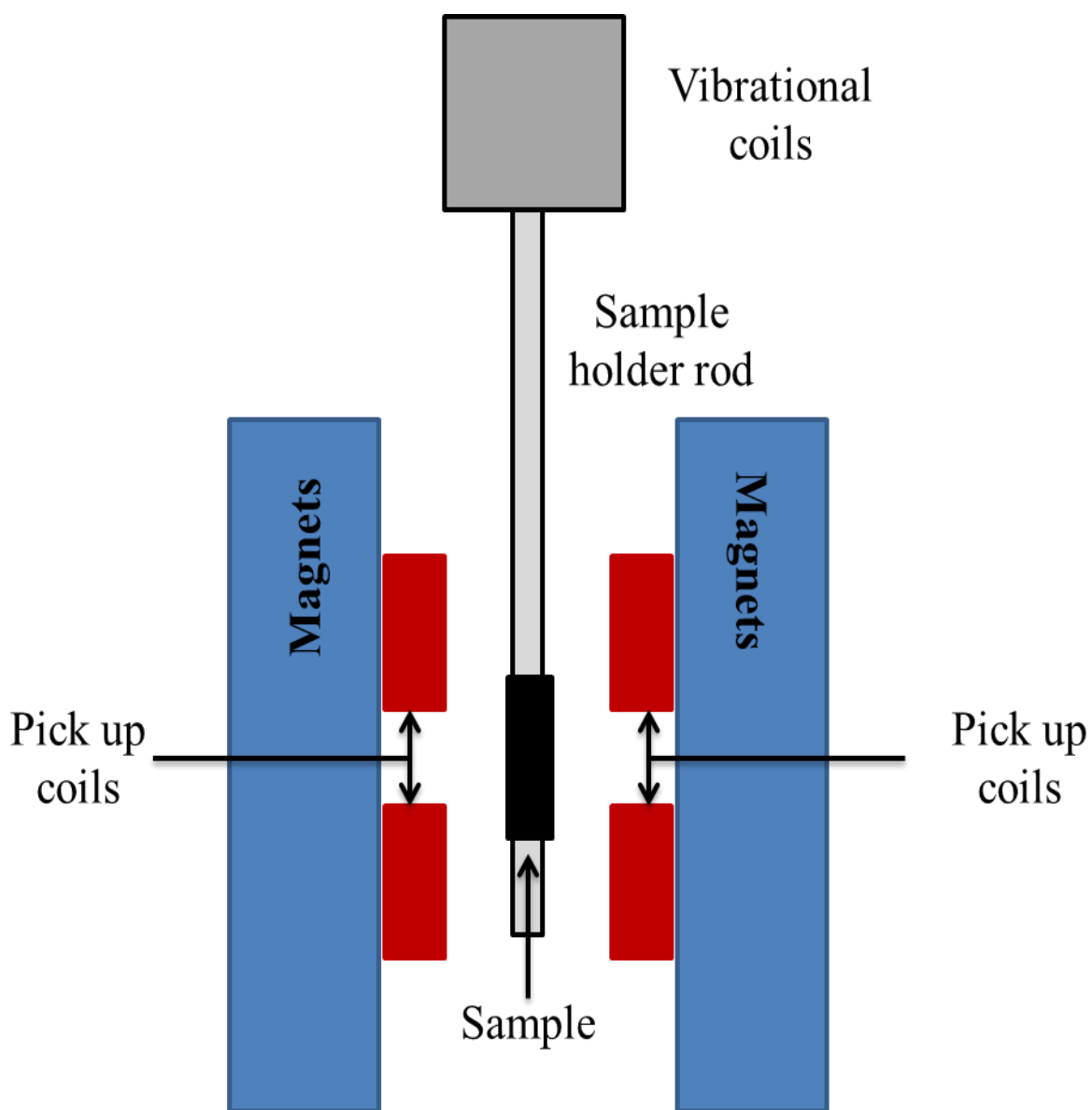
Figure 2-6: Schematic showing the main components of vibrating sample magnetometer (VSM)

2.6.Fluorescence spectroscopy

Fluorescence spectroscopy is a type of electromagnetic spectroscopy where the molecules of the sample are excited by irradiation at a definite wavelength of light (usually ultraviolet) and emit radiation of lower energy (higher wavelength). The emission spectrum provides information for both qualitative and quantitative analysis. When light of an appropriate wavelength is absorbed by a molecule (i.e., excitation), the electronic state of the molecule changes from the ground state to one of many vibrational levels in one of the excited electronic states. The excited electronic state is usually the first excited singlet state, S_1 (Figure 2-7). Collisions with other molecules cause the excited molecule to lose vibrational energy until it reaches the lowest vibrational state of the excited electronic state. The molecule then drops down to one of the various vibrational levels of the ground electronic state again, emitting a photon in the process. As molecules may drop down into any of several vibrational levels in the ground state, the emitted photons will have different energies, and thus frequencies. Fluorescence is one of these processes that correspond to the relaxation of the molecule from the singlet excited state to the singlet ground state with emission of light. The wavelength and thus the energy of the emitted light are dependent on the energy gap between the ground state and the excited state. The fluorescence quantum yield (Φ) gives the efficiency of the fluorescence process. It is defined as the ratio of the number of photons emitted to the number of photons absorbed (Eq. 2.3).

$$\Phi = \frac{k_f}{\sum_i k_i} \qquad \qquad 2.3$$

Where k_f is the rate of spontaneous emission of radiation and $\sum_i k_i$ is the sum of all rates of excited state decay. Other rates of excited state decay are caused by mechanisms other than photon emission and are therefore called "non-radiative rates", which can include: dynamic

collisional quenching, near-field dipole-dipole interaction internal conversion and intersystem crossing as shown in Figure 2-7.
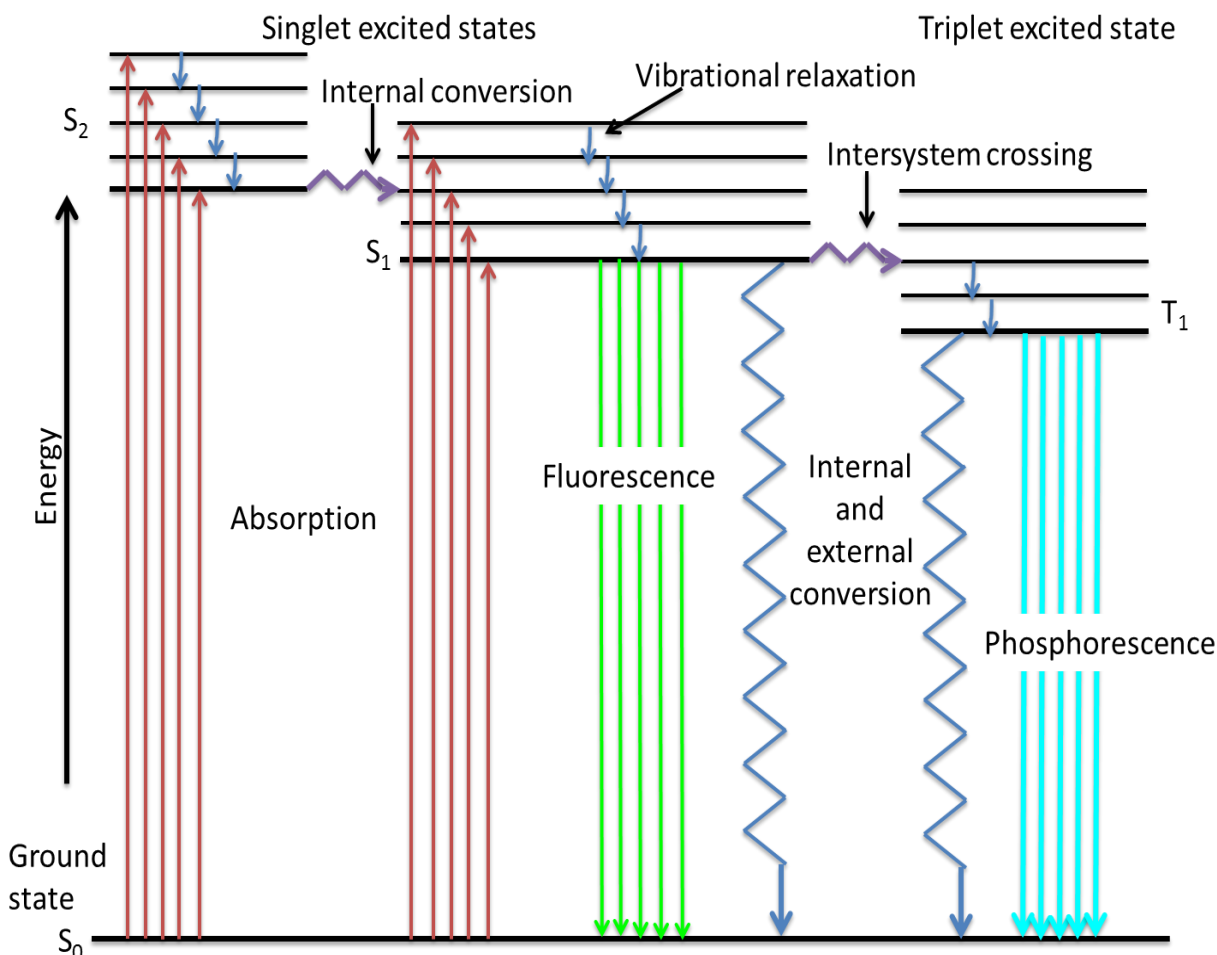
Figure 2-7: Electronic transition energy level diagram

In this research work fluorescent dyes Tris-(2,2'bipyridyl)dichlororuthenium (II), Rhodamine B were used as the drug analog. The release of these dyes from the polymeric composites was determined using the fluorescence spectroscopy. Fluorescence spectroscopy is recognized as one of the most sensitive technique, and it is possible to measure the concentration of the fluorescent substance at nano gram levels. This work was carried out on Cary Eclipse Fluorescence Spectrophotometer equipped with a xenon lamp. Figure 2-8 represents the

schematic representation of the fluorescence spectroscopy. The light from the xenon source that is excited passes through the monochromator and lands on the sample. The sample absorbs a portion of the incident light and the fluorescent molecules in the sample emit the light. A detector is attached at a viewing angle (usually around 90 degrees), which prevents incident light from contaminating the detected fluorescent light.
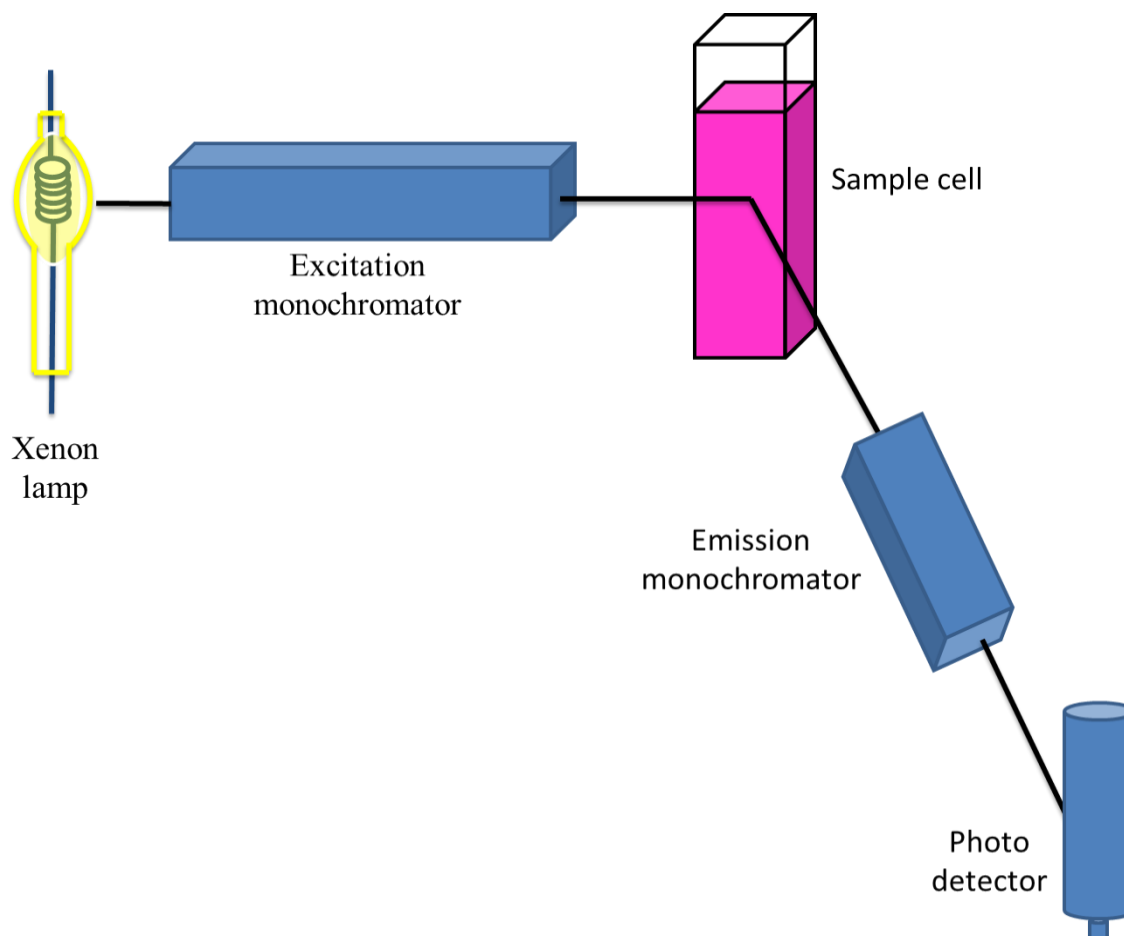
Figure 2-8: Block diagram of a fluorescence spectroscopy

2.7. Fourier transform infrared spectroscopy (FTIR)

Infrared spectroscopic technique utilizes lower energy infrared (IR) radiation (10000 – 100 cm^{-1}) to induce vibrational and rotational excitation of atoms and groups of atoms within a

molecule. When the frequency of the incident light equals to resonant frequencies of the internal molecular vibrations in a material, absorption occurs causing the molecule to vibrate in a higher energy level. Absorption occurs when the incoming IR radiation that is interacting with a molecule has sufficient energy to raise the vibrational energy level of the molecular system to the next allowed level. The frequencies and intensities of absorbed infrared light depend on the specific bond strengths and the geometrical shapes of the molecule. The absorption pattern (called a spectrum) is unique for each material. The infrared spectrum is measured by either absorbance or percent transmittance on the y-axis and by either the wavelength (μm) or wavenumber (cm^{-1}) to measure the position of an infrared absorption on the x-axis. Analysis of this absorption spectrum reveals details about the molecular structure of the sample based on the known symmetric and random vibrational modes of different atomic arrangements. This can be very helpful in functionalization studies for scientific research. For example, the shifting or disappearance of absorption bands in the spectrum of a given functional ligand can be evidence to change in the functional group of the ligand. Although this technique does not typically give conclusive evidence alone, it can be very powerful if used in conjunction with other data.

The main component in the FTIR spectrometer is an interferometer. The interferometer consists of two mirrors and a beam splitter positioned at an angle of 45 degrees to the mirrors which separate it into two beams. One will reflect from a fixed mirror in place and the other will reflect from a moving mirror. The two beams are then reflected back and recombined at the beam splitter with half of the light passing on toward the sampling areas and half travelling back toward the source. The signal at the detector is a cosine wave.
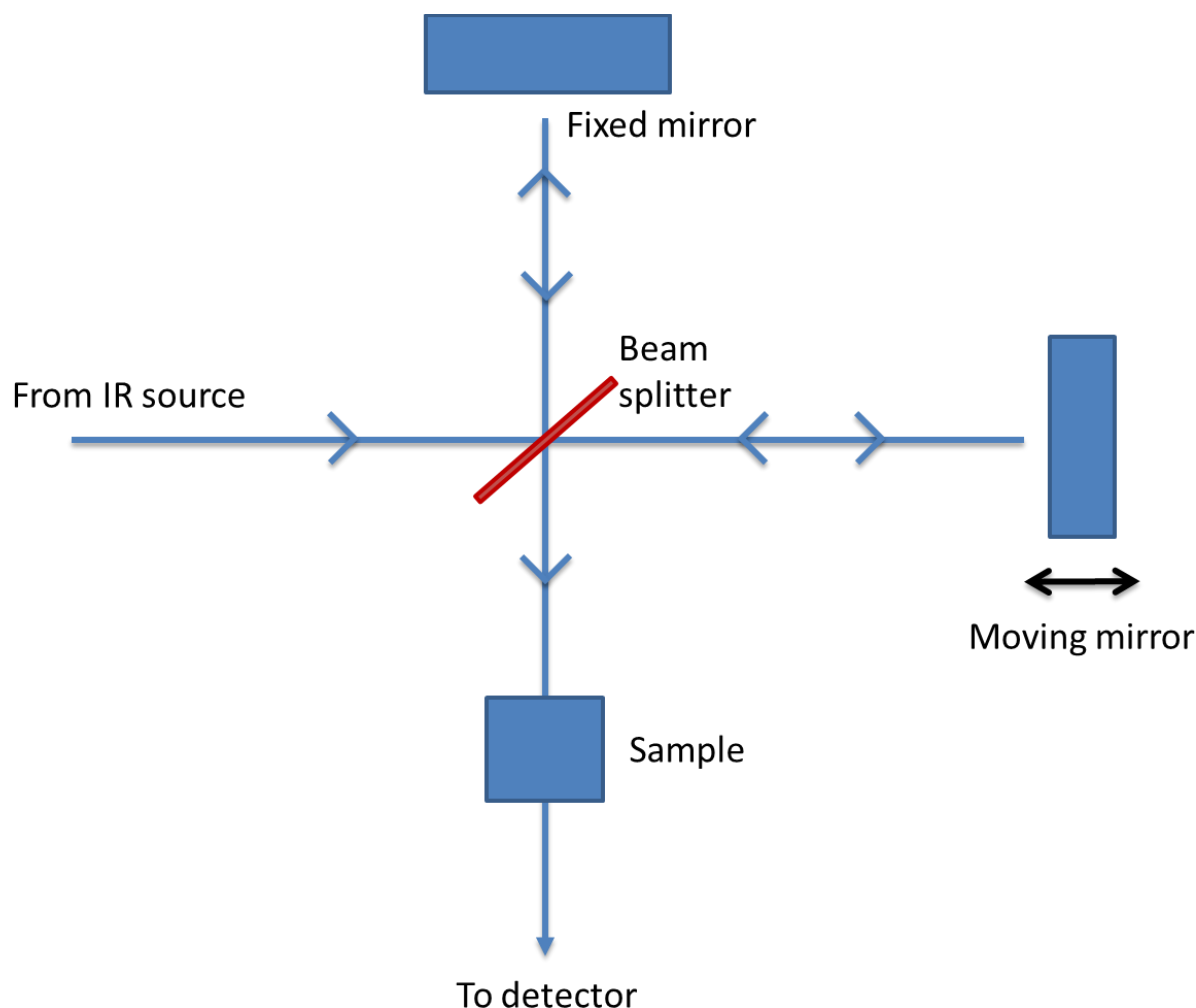
Figure 2-9: Block diagram of FTIR spectrometer

Fourier transform infrared (FTIR) spectroscopy was performed with Thermo Nicolet NEXUS 670 FTIR attached to an attenuated total reflectance (ATR) accessory. ATR was fitted with a single bounce diamond at 45° internally reflected incident light providing a sample area of 1 mm in diameter with a sampling depth of several microns. This accessory provides for the non-destructive measurement of samples with little or no preparation. A small amount of the sample was directly placed on the diamond disk and scanned for absorbance over the range from 4000 to 500 cm^{-1} wave numbers at a resolution of 1 cm^{-1}.

2.8. Ultraviolet-visible spectroscopy (UV-vis)

Ultraviolet visible spectroscopy measures the response of a sample to ultraviolet and visible radiations region of electromagnetic spectrum. When the sample is irradiated with light with wavelength in the UV-vis region, the molecular atoms undergoes electronic transitions from the ground state to the higher excited state. These electronic transitions in organic compounds can be explained by one of the following processes: σ to σ^* transition that is present in compounds containing single bonds. π to π^* transition that takes place in compounds that contain double bonds. n to σ^* and π to π^* transitions are present in compounds containing lone-pair of electrons and a single or a double bond respectively. Also, d-d or f-f transitions in inorganic compounds take place between a ground and an excited state of the d and f orbitals respectively. The wavelength and amount of light that a compound absorbs depends on its molecular structure and the concentration of the compound used.

Figure 2-10 shows the basic setup of the UV-vis spectrometer. A beam of light from a visible and/or UV source passing through the diffraction grating where the light is separated into its component wavelengths. Then the monochromatic light beam travels through the aperture, which is an opening that determines the cone angle of the light rays that comes to focus in the image plane. Finally the light passes through the sample before the materials absorption is detected. In this work UV-vis spectroscopy was used to determine the folic acid conjugation to the PLGA polymer. The UV-vis spectroscopy was performed on Hewlett Packard 8453 UV-visible Spectroscopy Systems.
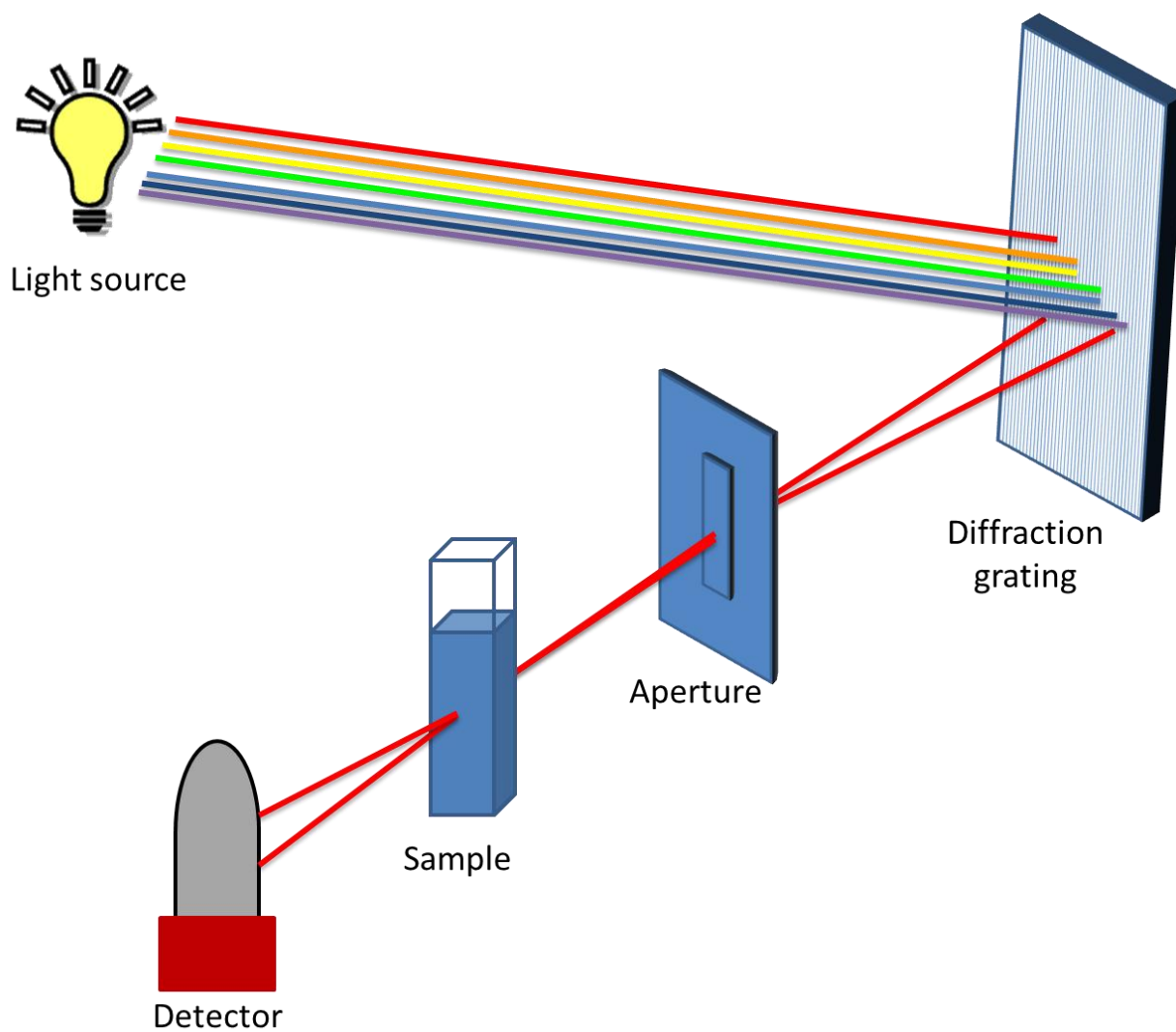
Figure 2-10: Block diagram of the UV-vis spectrophotometer

Chapter 3. Iron oxide nanoparticles and their properties

3.1. Iron oxide nanoparticles

Magnetic iron oxide nanoparticles are iron oxide particles with diameters between 1-100 nanometers (nm). There are several different forms of iron oxide; however the three main forms in which the iron oxide nanoparticles exist are magnetite ($Fe^{II}Fe^{III}_2O_4$, ferrimagnetic), maghemite (α-Fe_2O_3, ferrimagnetic), and hematite (γ- Fe_2O_3, weakly ferromagnetic or antiferromagnetic).[109,110] Magnetite has an inverse spinel structure with the divalent Fe^{2+} ion in tetrahedral (A sites) coordination and the trivalent Fe^{3+} ions in octahedral (B sites) coordination with oxygen as shown in Figure 3-1.[111] Maghemite also have an inverse spinel structure like magnetite in which each cell contains 32 oxygen ions, 21 1/3 Fe^{3+} ions and 2 1/3 vacancies.[110] It differs from magnetite in that all or most of the iron are in the trivalent Fe^{3+} state and cations are distributed randomly over the 8 tetrahedral and 16 octahedral sites. Hematite has a rhombohedral crystal structure with the trivalent Fe^{3+} ions in octahedral coordination with oxygen.[110] These nanoparticles can be synthesized using a variety of synthetic techniques such as the sol-gel process, reverse micelles technique, chemical precipitation, hydrothermal synthesis, polyol technique, and physical vapor deposition, and pyrolysis.[112-117] All these methods are well used procedures for nanoparticles preparation; however, the particles produced by these techniques differ in the size, morphology, size distribution and magnetic properties.[110,116,118]
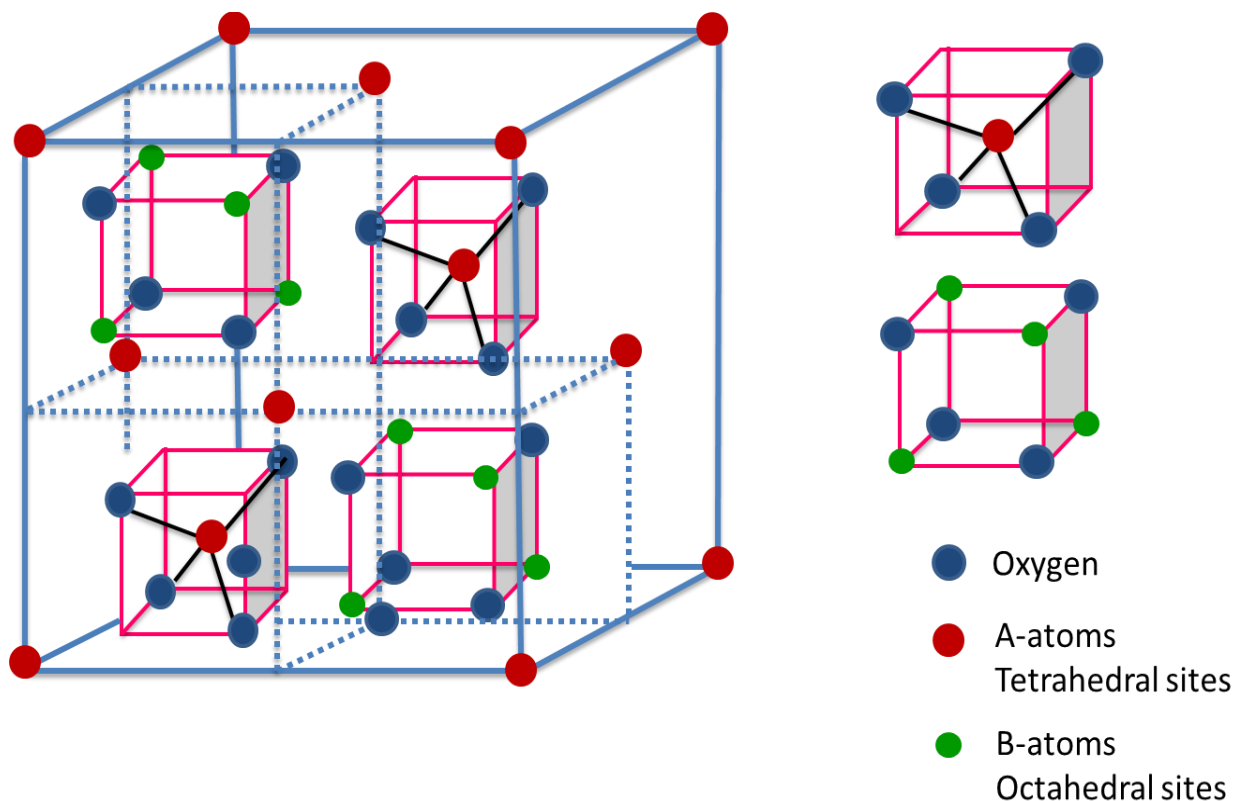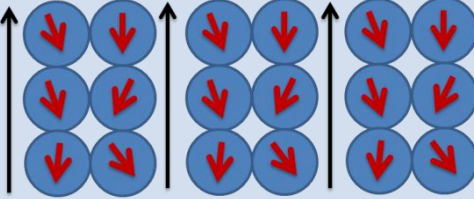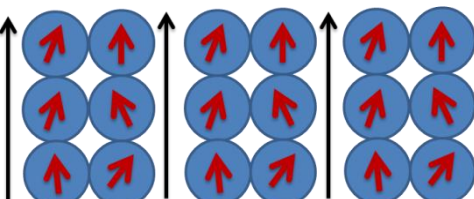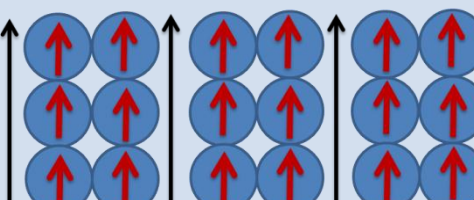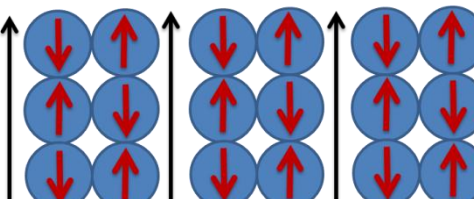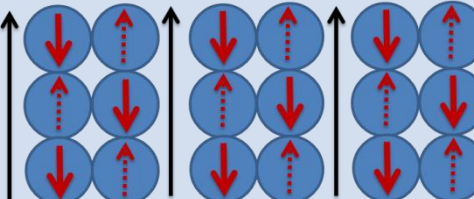
Figure 3-1: Drawing of the spinel structure illustrating the octahedral and tetrahedral sites

3.2. Magnetism

Magnetic property in general sense arises from unpaired electron spins in outer shell, or valence electrons of an atom. An Iron atom with 4 unpaired electrons in 3d shell has a strong magnetic moment. Ions Fe^{2+} has also 4 unpaired electrons in 3d shell and Fe^{3+} has 5 unpaired electrons in 3d shell. Therefore, when nanoparticles are formed from iron atoms or ions Fe^{2+} and Fe^{3+} they can be in ferromagnetic, antiferromagnetic, or ferrimagnetic states. A better understanding of magnetism in general is an essential step on the way into understanding the magnetism of these nanoparticles. The magnetic behavior of materials can be classified into five major groups as shown in Table 3-1

Types of Magnetism	Applied magnetic field	Resultant effect
Diamagnetism		• Repel the field • Negative magnetic susceptibility
Paramagnetism		• Align from the field • Small positive magnetic susceptibility
Ferromagnetism		• Align with the field • Large positive magnetic susceptibility
Antiferromagnetism		• Half of the spins align with the field • Divergence observed in the magnetic susceptibility
Ferrimagnetism		• Some spins align with the field and some did not • Positive magnetic susceptibility

Table 3-1: Schematics of the five main types of magnetism seen in a material and their response to the applied magnetic field. Paramagnetic, Ferromagnetic, and Ferrimagnetic materials have net positive magnetic moment in the direction of the applied field. Diamagnetic and Antiferromagnetic materials have a zero net moment.

3.3.Diamagnetism and Paramagnetism

Diamagnetism refers to materials that are repelled from an applied magnetic field. Diamagnetic material has paired electrons in their valence shell, leading to a net zero magnetic moment. When an external field is applied a force is generated by the field that leads to speeding up or slowing down of paired electrons. This leads to the change in the magnetic moment of the orbital in a direction opposite to the external field. The spins in diamagnetic materials align in an opposite direction to the field leading to negative magnetic susceptibility.

Paramagentism is the direct opposite of diamagnetism which takes on an alignment in the direction of the applied magnetic field i.e. they are attracted to a magnetic field. In a paramagnetic material, the spins of the electrons are not coupled and will have a resultant magnetic moment. This moment tend to align with the applied magnetic field leading to a small positive magnetic susceptibility. Paramagnetic materials have short range magnetic order because they relax back to their original random state in the absence of magnetic field. The other basic forms of magnetism- ferro, ferric and antiferro magnetism like paramagnetism possess magnetic moment. The only difference to paramagnetic material is in the ability of these magnetic materials to interact and couple with the applied magnetic field through exchange coupling.

3.4. Exchange coupling

Exchange coupling is a quantum mechanical phenomenon arising due to the relative orientation of the spins of two electrons. There are three types of exchange coupling by which atomic spins in a material can interact. These are direct exchange, indirect exchange, and superexchange that may produce either parallel or antiparallel exchange coupling. Direct exchange occurs due to quantum mechanical coupling between electrons of adjacent atoms.

For example if a system involves two atoms, each with one electron and if the interatomic distance is relatively small, the electrons will spend most of their time between the nuclei to minimize Coulomb interactions. Pauli's exclusion principle states that electrons in the same space and time must possess opposite spins, as illustrated in Figure 3-2. This gives rise to antiparallel alignment and therefore negative exchange.
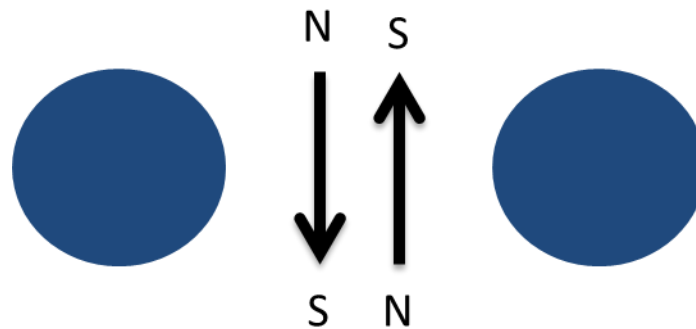
Figure 3-2: Direct exchange coupling between the neighboring atoms leads to an antiparallel alignment of the electrons. This is due to Pauli's exclusion principle when the electrons are located in the same space and time.

Indirect exchange coupling takes place when the interatomic distances are larger. The electrons then tend to be away from each other to minimizing electron-electron repulsion. This results in the parallel alignment or positive exchange as shown in Figure 3-3.

Figure 3-3: Indirect exchange coupling takes place due to larger interatomic distance between the adjacent atoms leads to a parallel alignment

Superexchange occurs between two atoms that are too far apart to be connected by direct coupling, but are connected by some other nonmagnetic atom, such as oxygen. Fig. 3.4 shows a simple representation of superexchange between two spins connected by a common nonmagnetic atom. Parallel or anti parallel alignment of the coupled electrons is dependent on the distance and orientation or bond angles of the exchange. For example, the tetrahedral sites in the spinel ferrite structure align anti-parallel to the octahedral sites via this superexchange mechanism. The metal cations in the ferrites and metal oxides interact through superexchange.
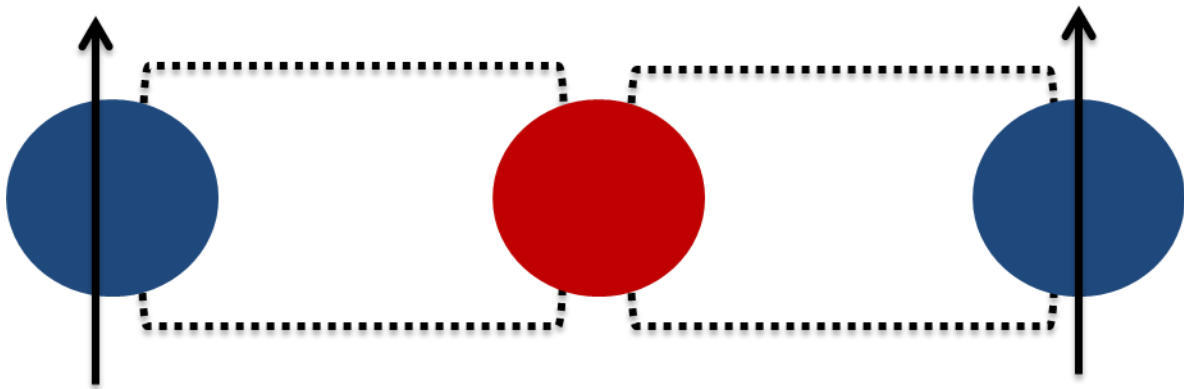
Figure 3-4: Superexchange between two magnetic atoms through a nonmagnetic atom

3.5. Ferromagnetism, Ferrimagnetism and Antiferromagnetism

Ferromagnetic materials exhibit parallel alignment produced due to indirect coupling of the electron spins. The electron spins in ferromagnetic materials align parallel to each other within small regions of the material to form domains. In an un-magnetized state, the domains are aligned at random so there is no overall magnetic effect. When an external magnetic field is applied to the material, the domains align to point in the same direction, producing a strong overall magnetic effect. Ferromagnetic materials tend to have long range ordering and show high positive magnetic susceptibility. While in antiferromagnetic materials the magnetic

moments of atoms that are related to the spins of electrons, align in opposite direction to each other due to direct exchange coupling. Antiferromagnetic materials have zero net magnetization as the magnetic moments equal in magnitude are aligned in opposite directions. Ferrimagnetic materials magnetic moment is aligned antiparallel to each other as in antiferromagnetic materials but the moments are unequal in magnitude and spontaneous magnetization remains. The substances behave like ferromagnetic materials. Ferrimagnetism is exhibited by ferrites and magnetic oxides.

Figure 3-5 represents the curve of the magnetization (alignment of the spins with magnetic field) versus the applied field curve, commonly known as the M-H curves of diamagnetic, paramagnetic, and ferromagnetic materials. Diamagnetic materials show an inverse relation between the applied field and the magnetization because the spins oppose the direction of the applied field. While a direct relationship between the applied field and the magnetization is seen for paramagnetic materials as their spins align with the field. As the paramagnetic materials have short range magnetic ordering, no saturation magnetization (M_s) is observed. Saturation magnetization (M_s) is described as the alignment of all the spins of the particles with the applied external magnetic field. Consequently they have zero remnant magnetization (M_r) and zero corecivity (H_c). Remnant magnetization (M_r) is the retention of magnetization in the absence of an applied magnetic field and zero coercivity (H_c) is defined as the intensity of the applied magnet field required to reduce the magnetization of that material to zero after the magnetization of the sample has been driven to saturation. The M-H curves for ferromagnetic forms a hysteresis loop. High magnetization saturation is reached in ferromagnetic materials as the magnetic domains align with the applied field. Thus, ferromagnetic materials have a coercivity value higher than zero, because a certain amount of

energy is needed to randomize the highly aligned domains.   They also retain magnetization after the applied field is removed giving a positive remnant magnetization value.
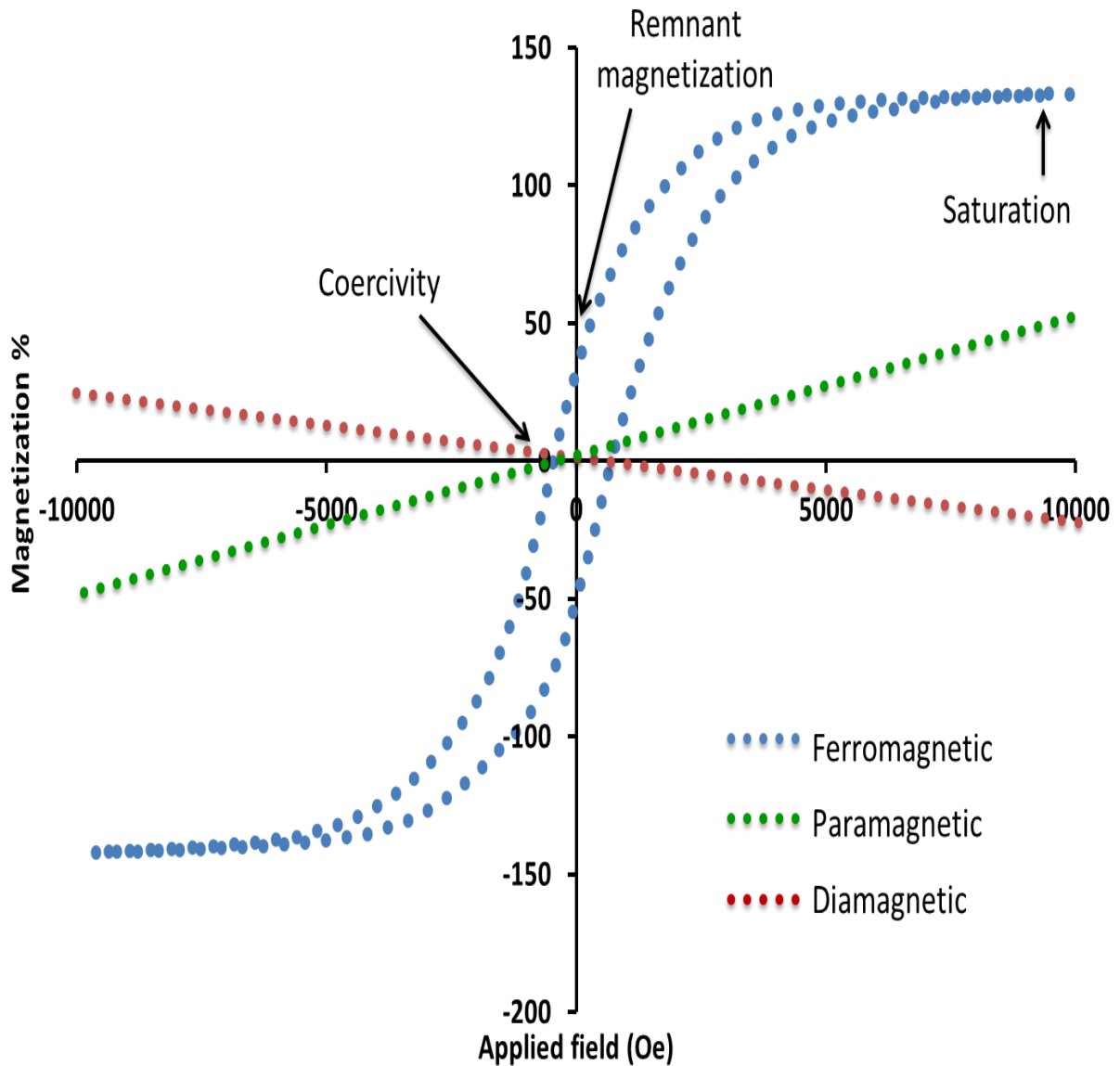
Figure 3-5: The expected plot of magnetization vs. applied field for diamagnetic, paramagnetic and ferromagnetic materials

3.6. Superparamagnetism

In bulk ferromagnetic materials, when an external magnetic field is applied the magnetic moments exhibit multi domain properties, each domain presents a group in which all the atomic magnetic dipoles are spontaneously aligned. These magnetic domains are separated by domain walls of ~100 nm width. When the bulk magnetic materials are reduced to nanoscale the width of the domain walls also reduces. Magnetic particles below a certain diameter cannot support more than one domain and are thus described as single-domain.[119] This diameter is termed as the critical diameter and is given by Eq. 3.1

$$\frac{2A^{\frac{1}{2}}}{M_S} \qquad \qquad 3.1$$

Where A is the exchange constant, M_S is the moment per unit volume and for typical materials its value is 10–50 nm.[119] At this size all the atomic magnetic moments are rigidly aligned as a single giant spin and the magnetic behavior of the particles is defined as superparamagnetism.[117,119,120] When a high magnetic field is applied however, the spins align with each other resulting in saturation of the magnetic moment (similar to ferromagnetism), but when the magnetic field is removed, the magnetic moments undergoes magnetic relaxation (similar to paramagnetism). The relaxation of the magnetization orientation of each particle is determined by Eq. 3.2

$$\tau = \tau_0{}^{KV/2kT} \qquad \qquad 3.2$$

Where τ is the relaxation time at one orientation, K is the particle's anisotropy constant, V is the particle volume, k is the Boltzmann's constant, and T is the temperature. As the size of the particle decreases to a level where KV (free-energy barriers) becomes comparable to kT

(thermal energy), its magnetization starts to fluctuate from one orientation to another, leaving no coercivity and net magnetic moment.[119,121] At this nanoscale the particle responds quickly to an external magnetic field to reach saturation magnetization, while dropping back to zero when the field is removed.

This superparamagnetic property of the iron oxide nanoparticles makes them very attractive for potential applications in several fields, especially for biomedical applications such as enhanced resolution magnetic resonance imaging (MRI), targeted drug delivery and imaging, hyperthermia, magneto-transfections, gene therapy, stem cell tracking, molecular/cellular tracking, magnetic separation technologies (e.g. rapid DNA sequencing), detection of liver and lymph node metastases.[122-124] The focus of this research is on designing a dual modal imaging and therapeutic drug delivery system, so the role of superparamagnetic iron oxide nanoparticles as contrast agents in MRI and heating agents in hyperthermia will be discussed briefly in sections 3.3 and 3.4.

3.7. Magnetic resonance imaging (MRI) application

Magnetic resonance imaging (MRI) is a powerful tool for the diagnosis of disease and the study of biological processes such as cancer metastasis and inflammation. MRI makes use of the property of nuclear magnetic resonance (NMR) to image hydrogen nuclei inside the body. The MRI image is constructed because of the difference in the rates of equilibrium states of protons that are present in various environments (tissues). The protons in water and tissue will align in a given direction (z-axis) when a static magnetic field is produced by the MRI magnets. A radio frequency (RF) pulse at the resonance frequency (Larmor frequency) is applied to the aligned protons which flips the spin of the aligned protons in the body. Once

the Rf pulse is removed the excited protons begin to relax back to their original spin states through longitudinal relaxation time (T_1) or transverse relaxation time (T_2). The spin lattice or longitudinal relaxation time (T_1) describes the rate that nuclear spins return to equilibrium and the spin–spin or transverse relaxation time (T_2) is the time constant that describes the rate of signal decay. The MRI signal is governed by the concentration of protons and the nuclear relaxation time, T_1 and T_2.[125] The image contrast can be varied by adjusting the instrumental parameters of the imaging process or by taking advantage of the intrinsic parameters such as the local concentration of the hydrogen nuclei, relaxation parameters, and magnetic susceptibility. Above all this the contrast of the image can be enhanced by intravenously injecting contrast agents.[126,127] MRI contrast agents alter the relaxation times of the tissues and body cavities, and depending on the image weighting, it can give a higher or lower contrast signal. Paramagnetic gadolinium (Gd) based particles are the most commonly used MRI contrast agents, which shows a strong T_1 shortening effect.[128] However they have relatively low contrast effects and a very short retention time in vivo. Also the toxicity and biocompability of these Gd based contrast agents are not clearly known.[129] Superparamagnetic iron oxide (Fe_3O_4 and Fe_2O_3) nanoparticles are gaining much attention as MRI contrast agents. [123,130,131] Superparamagnetic iron oxide nanoparticles have high magnetic moment which can cause microscopic field inhomogeneity and can activate the dephasing of the protons. This makes them effective in reducing the T_2 relaxation time, and thereby leading to signal hypo- intensities in T_2 or T_2^* weighted images. The image areas containing iron oxide nanoparticles therefore induce a signal darkening on the MRI images.[109,132] The signal void due to the large magnetic susceptibility of the nanoparticles is much larger than the nanoparticle size, thus enhancing the detectability. Designing these

nanoparticles with targeting specificity, the negative contrast alterations can be harnessed to report abnormal biological activity.

3.8. Magnetic hyperthermia

Hyperthermia can be defined as controlled temperature elevation by targeting the heating field to the malignant tumors as well as the surrounding tissue, organ, part of body or even to the whole body. The use of hyperthermia in the treatment of malignant tumors is well-known since ancient times. Hippocrates, the father of medicine had proposed that surface tumors can be treated by the application of hot iron.[133] Hyperthermia is a promising form of cancer therapy alongside of the typical methods of surgery, chemotherapy and radiotherapy. Hyperthermia takes the advantage of the cancerous cells being more sensitive to higher temperatures in the ranged of 42-45º C than the healthy cells. The tumor cells could be killed by necrosis if the temperature is above 45º C, or could it can help improve the efficiency of chemotherapy if the temperature is raised around 42º C.[134]

Magnetic iron oxide nanoparticles act as mediators and help induce heat to the tumors. When these nanoparticles are exposed to an external alternating current (AC) magnetic field, some heat is generated due to magnetic hysteresis loss. These losses, depending upon the thermal conductivity and heat capacity of the surrounding medium are dissipated in the form of heat; raising the temperature of the surrounding. The amount of heat generated depends on the nature of the magnetic particles and the external field applied. The heat dissipated by a magnetic nanoparticles subjected to an AC magnetic field is given by specific absorption rate (SAR), which is described as shown in Eq. 3.3. SAR is expressed in W/g of nanoparticles.

$$SAR = C \times \frac{\Delta T}{\Delta t}$$ 3.3

Where C is the specific heat capacity of the sample and T and t are the temperature and time, respectively.[135,136] SAR is very sensitive to the material properties. In multi-domain particles the heat is generated mainly due to magnetic hysteresis loss, but it is different for small, single domain particles. As the size is reduced the particles shows superparamagnetic behavior and would not exhibit hysteresis loss. The two main contributing mechanisms of SAR in single domain superparamagnetic nanoparticles are the Néel relaxation and Brownian relaxation. Néel relaxation is the random flipping of the spin without rotation of the nanoparticle and depends on the magnetic property of the nanoparticles. The Néel relaxation mechanism is analogous to the hysteresis loss in multi-domain magnetic particles whereby there is an internal friction due to the movement of the magnetic moment in an applied external magnetic field that results in heat generation. In Néel relaxation the moment alignment occurs via the usual Stoner–Wohlfarth process subject to thermal activation where the relaxation time is given by Eq. 3.4.

$$\tau_N = \tau_0 exp^{(\frac{\Delta E}{kT})} \qquad\qquad 3.4$$

Where τ_N is the Néel relaxation time, τ_0 is the average relaxation time in response to a thermal fluctuation and is typically in the order of a few nanoseconds, k is the Boltzmann constant, T is the temperature and ΔE is the energy.

Brownian relaxation is the rotation of the entire nanoparticle within the fluid medium and depends on the viscosity of the medium as shown in Figure 3-6.[133,136,137] In Brownian relaxation the moment can align with the field by physical rotation with a relaxation time given by Eq.3.5

$$\tau_B = \frac{3\eta V_H}{kT} \qquad\qquad 3.5$$

Where η is the viscosity coefficient of the fluid, k is the Boltzmann constant, V_H is the hydrodynamic volume, T is the temperature, and τ_B is the Brownian relaxation time.
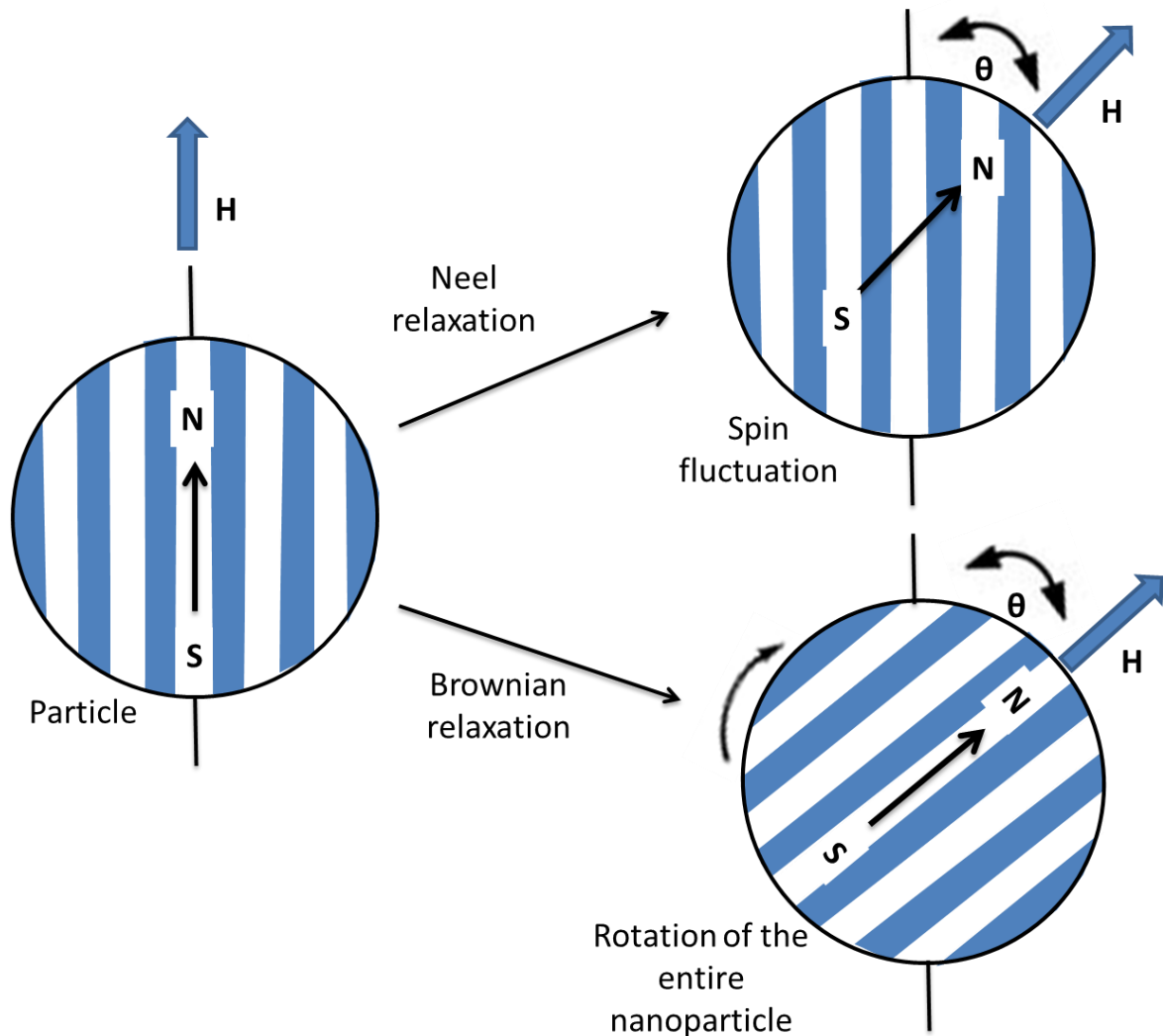
Figure 3-6: Schematic representation of relaxations of magnetic particles either through spin rotation (Neel) or particle rotation (Brownian), when the particles are exposed to an AC magnetic field. Néel relaxation is the random flipping of the spin without rotation of the nanoparticle while the Brownian relaxation is the entire rotation of the nanoparticle in the fluid.

Chapter 4. Poly (styrene-co-vinylbenzylchloride-co-divinylbenzene) (PSVBDVB) composites containing magnetic iron oxide nanoparticles

4.1. Overview

Polymeric nanocomposites have evolved as a potential tool for the design of an ideal drug delivery system (DDS) for cancer treatments. Both imaging and therapeutic agents can be encapsulated within the polymeric nanocomposites through various techniques as discussed in chapter 1. In this project magnetic iron oxide nanoparticles have been used as a dual modal imaging (contrast agents for MRI) and therapeutic agent (heat mediators in hyperthermia), which are encapsulated into poly (styrene-co-vinylbenzylchloride-co-divinylbenzene) (PSVBDVB) polymer.[79]

The key step in the design of a dual modal drug delivery system is the encapsulation of the magnetic iron oxide nanoparticles with polymer of choice. A proper understanding of possible synthetic anomalies that arise from the inclusion of nanoparticles within the polymer during synthesis is necessary. It is also very important to investigate the dilution effect of the saturation magnetization of the iron oxide nanoparticles due to the polymer coating. Different types of polymer coating have been investigated and the choice of the appropriate one depends on many factors and principally on the clinical purposes of the functionalized nanoparticle. The most commonly polymer coating used for biocompatible iron oxide nanoparticles is derivatives of dextran.[138,139] The association of dextran with iron oxide has led to its widespread use as a coating for iron oxide NPs for many decades. However, either dextran or nanoparticles made with dextran can cause anaphylactic reactions. Also the dextran coating is found to be biologically unstable and leads to sedimentation and aggregation of the iron oxide nanoparticles.[140] Therefore it is desirable that the magnetic nanoparticles be efficiently encapsulated into a robust polymer.

To study these synthetic variations upon encapsulation with a polymer, the magnetic iron oxide nanoparticles were encapsulated into a robust poly (styrene-co-vinylbenzylchloride-co-divinylbenzene) (PSVBDVB).[79]   PSVBDVB is a copolymer of styrene, vinylbenzylchloride (VB) and divinylbenzene (DVB) and their structures are shown in Figure 4-1. Polystyrene copolymer is biocompatible, cheap, well-known, and can be easily functionalized by copolymerization. Also the polymerization process for the synthesis of polystyrene is very well established.[141] Furthermore the encapsulation of iron oxide nanoparticles within the polymer can be carried out by polymerization process, which ensures a homogenous distribution of the nanoparticles within the composites.   The cross linking agent divinylbenzene (DVB) was used to impart better mechanical strength to the polymeric composites, as compared to styrene alone. Vinylbenzylchloride (VB) confers a hydrophilic group to the composites which makes it possible for use in a wider range of applications like drug delivery, column separation technique. The only difference to styrene is that VB contains chlorine to the para position to the vinyl group so it would not interfere in the polymerization process and good distribution of VB would be obtained. Also addition of VB allows for the functionalization of the magnetic composites at the chlorine site through nucleophilic substitution reactions.
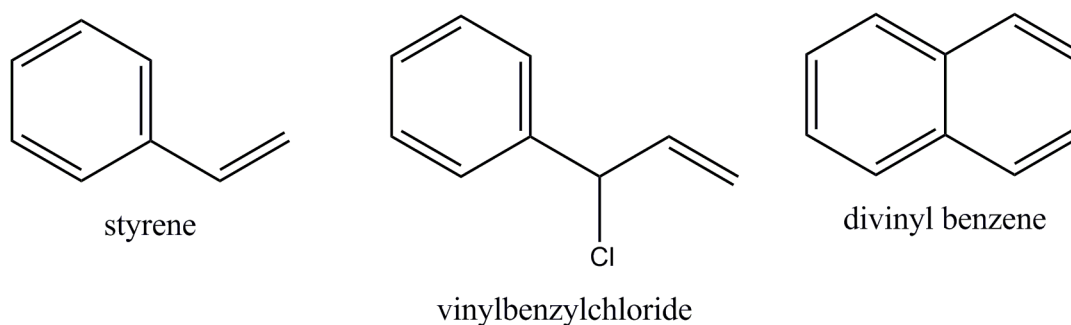
Figure 4-1: Structure of styrene, vinylbenzylchloride (VB) and divinylbenzene (DVB)

4.2. Synthesis

The first step in the synthesis of PSVBDVB composites containing the iron oxide nanoparticles is the synthesis of mono-dispersed iron oxide nanoparticles. In order to prepare iron oxide nanoparticles with uniform size and shape, it is necessary to control the kinetics of their nucleation and growth. The best control is achieved when the nucleation and growth steps are separated. There are numerous methods of iron oxide nanoparticle synthesis such as co-precipitation method, polyol technique, reverse micelles technique, sol gel technique, hydrothermal synthesis, chemical and physical vapor deposition, and pyrolysis.[114,142-144] Polyol technique is a simpler synthetic technique that allows for the control over the nucleation and growth events and will be discussed in detail in section 4.2.1

The next step is the synthesis of the PSVBDVB composites with iron oxide nanoparticles. To properly understand the possible synthetic anomaly that arises from the inclusion of nanoparticles within the polymer during synthesis. A homogenous polymer coating is desirable for magnetic nanoparticle encapsulation. For this reason precipitation polymerization technique was employed for the formations of PSVBDVB composite, where in the polymeric composites are synthesized from its monomers. PSVBDVB as discussed earlier is a copolymer of polystyrene. Conventional methods for the synthesis of the copolymers are dispersion polymerization, suspension polymerization, and emulsion polymerization. Mono-dispersed sub-micron sized polymeric composites with a highly cross linked structure cannot be obtained by these processes. Precipitation polymerization was thus utilized to synthesize highly cross linked polystyrene copolymers.[145,146] It is a very simple and versatile polymerization technique yielding mono-dispersed spherical polymeric composites. Precipitation polymerization will be discussed in detail in section 4.2.2

4.2.1. Synthesis of magnetic Iron oxide nanoparticles by Polyol technique

Iron oxide nanoparticles were synthesized by polyol technique similar to those found in the literature.[115,147,148] The polyol technique refers to the use of a polyalcohol (polyol) to reduce the metal precursor. The polyalcohol used acts as a solvent as well as when coupled with a base serves as a mild reducing agent.[115] In this technique, a solid inorganic precursor is suspended in a liquid polyol along with a base. The suspension is stirred and heated to a given temperature, leading to super-saturation of the solution. Consequently a short nucleation burst will occur followed by a slow growth of the metallic particles.[115] The starting materials can range from metal hydroxides, nitrates, chlorides to acetates. The reduction of metal precursors can be achieved in various polyols such as ethylene glycol, propylene glycol, diethylene glycol, trimethylene glycol, butylene glycol, and trimethylene glycol. The polyol technique produces finely dispersed, non-agglomerated metal nanoparticles with well-defined morphology, narrow size distribution and high crystallinity. The main advantage of polyol technique over other synthetic routes is that the polyol solvent also act as a protective layer preventing particles aggregation and passivates the nanoparticles against oxidation.

The synthesis of the iron oxide nanoparticles was carried out by polyol technique as shown in Figure 4-2. 0.40 g of Iron (II) acetate was slowly added to 25.00 mL ethylene glycol under magnetic stirring. After the metal precursor was completely dissolved 1.00 g of sodium hydroxide (NaOH) was added and the reaction solution was quickly heated to reflux under magnetic stirring for 1 hour. The initial reddish-brown solution turned black at the end of 1 hour reflux. The iron oxide nanoparticles were then magnetically extracted and further washed several times with methanol. In order to prepare the particles for the polymerization coating process, two further washes and extractions were performed with anhydrous acetonitrile and

sonication to remove any surface water, methanol, or glycol. After the last acetonitrile wash, the particles were dried in a vacuum oven and kept under vacuum until further use.
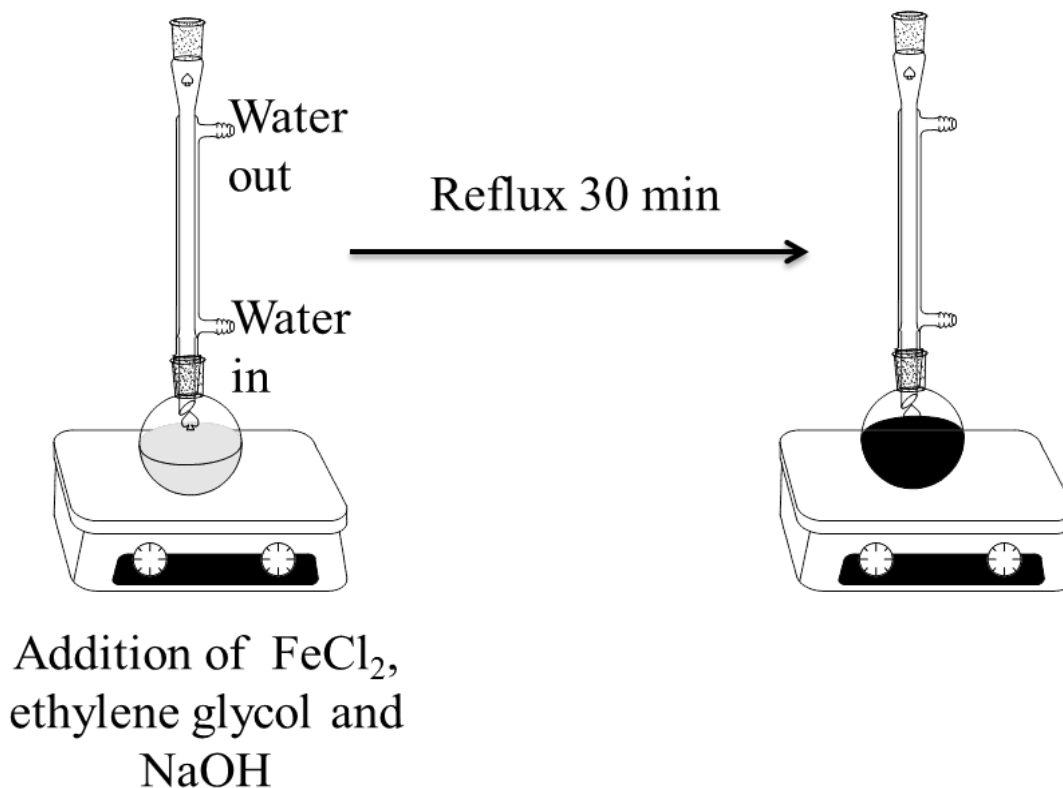
Figure 4-2: Synthesis of Iron oxide nanoparticles by Polyol technique

4.2.2. Encapsulation of magnetic iron oxide nanoparticles with in the Poly (styrene-co-vinylbenzylchloride-co-divinylbenzene) (PSVDVB) composites

Precipitation polymerization was carried out by similar methods used to produce poly (styrene-co-divinylbenzene) microspheres with the addition of vinylbenzylchloride in place of some styrene monomer.[141,149] Precipitation polymerization technique is a heterogeneous polymerization process that starts with a homogeneous system in the continuous phase, where the monomers and initiator are completely soluble, but upon initiation the formed polymer is

insoluble and thus precipitates outs.[150] During polymerization, the growing polymer chains phase-separate from the continuous medium by entropic precipitation as the cross-linking prevents polymer and solvent from freely mixing.[151] The uniqueness of precipitation polymerization is the absence of polymeric stabilizer which is the key element in other polymerization processes. The PSVBDVB composites containing iron oxide nanoparticles were synthesized as below.

Styrene and divinylbenzene (DVB) monomers were treated with 0.10 M sodium hydroxide solution to remove the inhibitor. Vinylbenzylchloride (VB) and azobisisobutyronitril (AIBN) were used as received. AIBN is used as an initiator for the polymerization process to start. The polymer composites were synthesized with monomer percentages of 30% styrene, 25% vinylbenzylchloride, and 45% divinylbenzene as shown in Figure 4-3. The iron oxide nanoparticles were added to 1.00 mL of monomer solution at mass percentages of 0%, 1%, 3%, and 5%, which was then placed under sonication to achieve a homogeneous dispersion of the particles in the monomer solution. The monomer solution or the particle/monomer solution was taken in a 250 mL round bottom flask equipped with a reflux condenser under N_2 atmosphere, and then 50.00 mL of anhydrous acetonitrile was added as the solvent. The reaction mixture was stirred mechanically at the rate of 60 rpm. Then 20.00 mg of AIBN (initiator) was added to the reaction solution and the solution was heated to 75°C to initiate the polymerization process. Once the temperature was stabilized at 75°C, the reflux condenser was capped with a balloon to maintain the reaction under N_2, and the reaction was allowed to age for 24 h. The reaction was then quenched in "cold" methanol (~-20°C) to precipitate the spherical polymeric composites. Vacuum filtration was employed for the polymeric composites without the magnetic nanoparticles and magnetic separation was employed for iron oxide nanoparticle loaded

polymeric composite samples followed by further drying under vacuum to obtain the final product.

Poly(styrene-co-vinylbenzylchloride-co-divinylbenzene
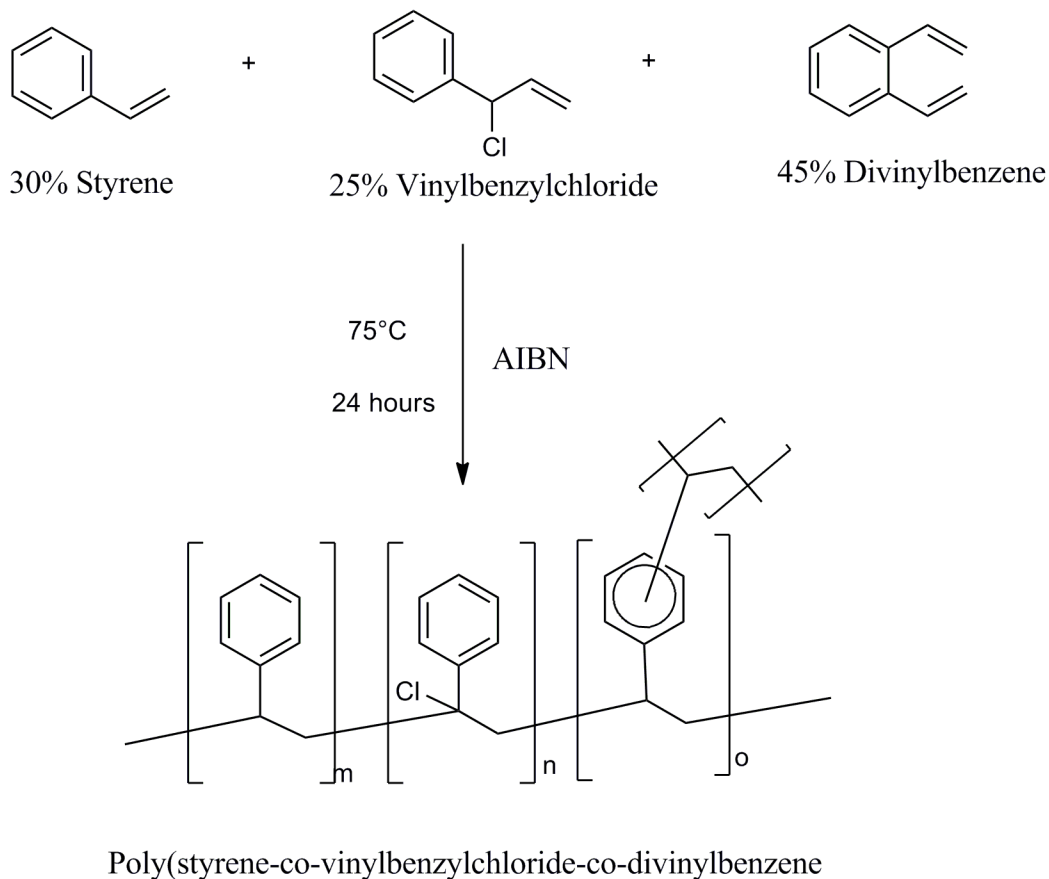
Figure 4-3: Structure of Poly (styrene-co-vinylbebzylchloride-co-divinylbenzene) along with its monomer content

4.3. Result and discussion

The PSVDVB coated magnetic iron oxide nanoparticles were characterized using a variety of analytical techniques including scanning electron microscopy (SEM), thermal gravimetric analysis (TGA), X-ray powder diffraction (XRD), and vibrating sample magnetometer (VSM).

Scanning electron microscopy (SEM) was performed on the polymeric composites, with and without the magnetic iron oxide nanoparticles loading. The SEM samples were prepared by lightly sprinkling the composite powder on a conductive carbon tape mounted on the sample holder. The sample was then sputtered with gold to make it conductive and reduce charging. The PSVBDVB composites without the iron oxide nanoparticle loading were spherical and mainly mono dispersed and had a mean diameter of 3 μm as seen in Figure 4-4 (a). With addition of 1% iron oxide nanoparticles by mass a decrease in the size of the polymeric composites to a mean diameter of 2 μm was observed, as well as an increase in the poly-dispersity of the composites was seen as shown in Figure 4-4 (b). With further increase in the ratio of iron oxide nanoparticles the size of the polymeric composites decreases and poly-dispersity of the composites increases. The difference in these samples can be explained if the particles act as nucleation sites for the polymer chains. In the case without particles, the number of polymer chains should be somewhat proportional to the amount of initiator. Then with a uniform amount of chains being connected by cross-linker (DVB), uniformly sized composites are achieved. When the nanoparticles are added, this gives a site for the monomers and forming polymer chains to orient or nucleate. This causes the DVB cross-linking agent to be used more quickly because the polymer chains are closer together, especially since the DVB has been found to be more reactive than the styrene monomer in the typical polymer synthesis.[152] It also uses more monomers around the surface of the nanoparticles due to their high surface area, thus shortening the overall length of the polymer.
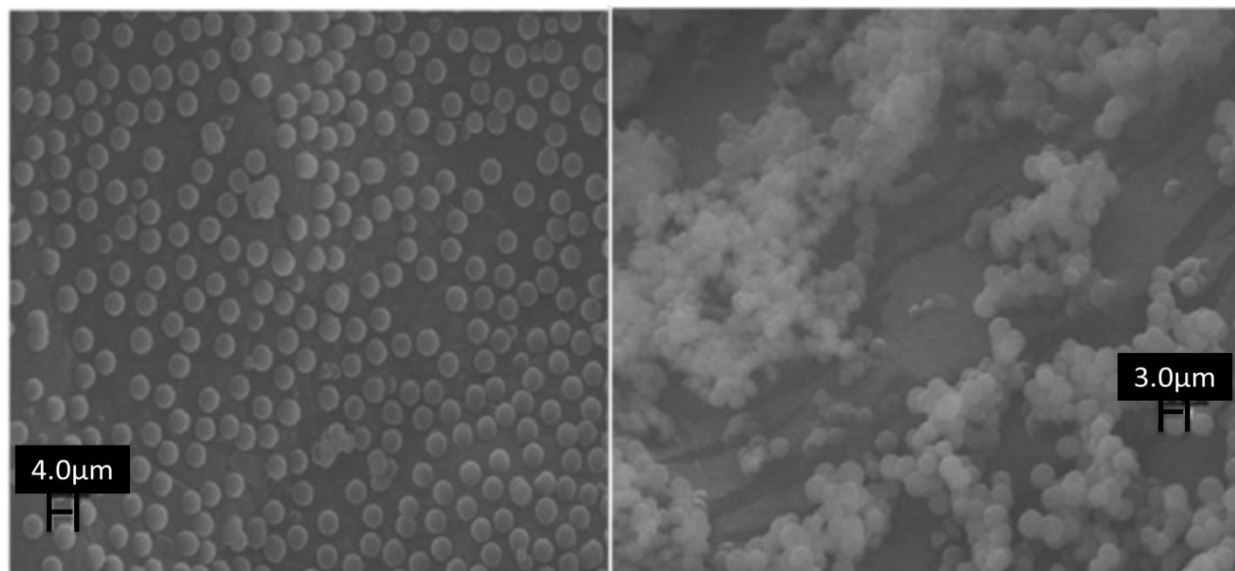
Figure 4-4: (a) SEM image of as synthesized polymer beads without nanoparticle, (b) 1% by mass nanoparticle to polymer reaction
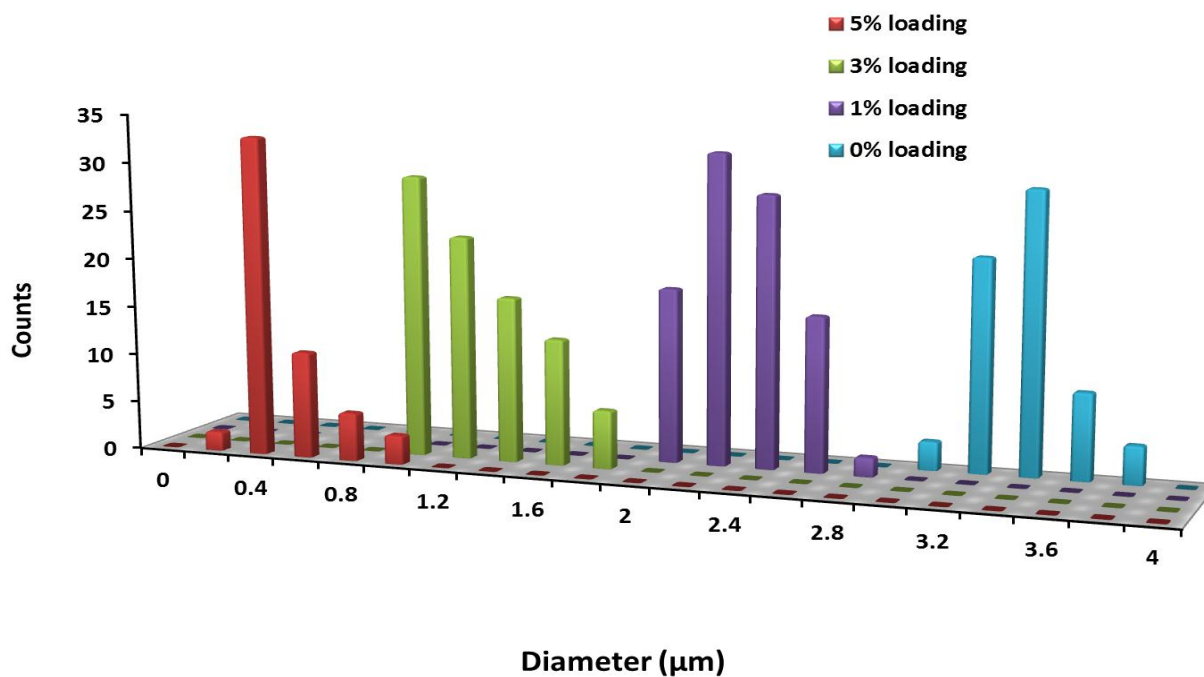
Figure 4-5: Histograms of size measurements from SEM images of nanocomposites with varying nanoparticle loading percentages.

This trend in size reduction is seen to continue as more nanoparticles are added to the system. The diameters of the spheres obtained are 3 ± 0.15 μm for 0% nanoparticles, 2 ± 0.30 μm for 1%, 1 ± 0.35 μm for 3%, and 0.5 ± 0.15 μm for 5%, and are shown in Figure 4-5.
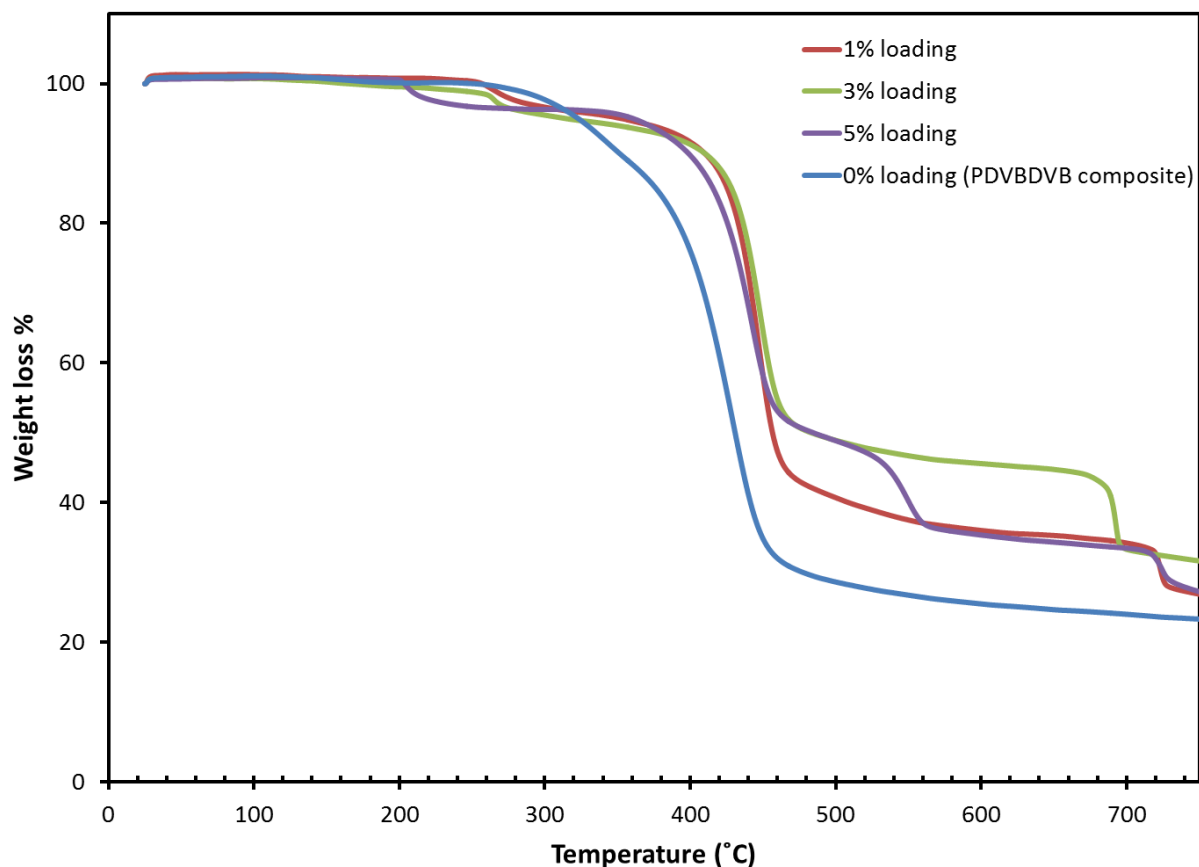
Figure 4-6: TGA plot showing decomposition profiles for the nanocomposites and polymer beads

Thermal gravimetric analysis (TGA) was used to investigate the composition of the composites formed. The PSVBDVB composites without the iron oxide nanoparticle loading show a major decomposition event around 350 ℃ corresponding to the decomposition of the PSVBDVB copolymer. As can be seen in Figure 4-6 the 0% loaded sample has a smooth decomposition profile with one primary decomposition temperature around 350 ℃. As the nanoparticle loading is increased to 1%, the first major decomposition event is observed around

440º C which is indicative of higher levels of cross linking between the monomers or greater density copolymer formation. There is also an addition decomposition event at around 720º C that is not present in the unloaded PSVBDVB composites and is attributed to the decomposition of the sample impurities on the surface of the iron oxide nanoparticles. Increasing to 3% nanoparticles loading the decomposition profile is similar to 1%, with slight differences in the later decomposition event around 700º C again attributed to decomposition of sample inpurities on the surface of nanoparticles.. Then upon increasing to 5% loading, a third decomposition event is observed at around 500º C attributed to the decomposition of the high density PSVBDVB copolymer. The increase in the decomposition temperature and the decomposition events is observed with increase in the nanoparticles loading. As the nanoparticle loading increases, DVB is used up quickly as the nucleation sites increases. This causing a non-uniform composition polymer formation due to the rapid utilization of the monomers, which is evident from the difference in the decomposition profiles.

The powder XRD pattern of the as-synthesized iron oxide nanoparticles shows an inverse spinel iron oxide phase with no impurities. Figure 4-7 shows XRD patterns of the as-synthesized iron oxide nanoparticles with an overlay of the data obtained from the JSPDS reference powder diffraction patterns of maghemite (α-Fe$_2$O$_3$). By comparing the reference diffraction pattern to the collected data, it is clear that the raw data is a representation of maghemite. The most intense peaks at 30.266º, 35.651º, 43.33º, 50.044 º, 53.766º, 57.319º, 62.949º, 71.430º, 74.493º 2θ corresponds to the (220), (311), (400), (421), (422), (511), (440),(620), and (533) planes in the maghemite crystal structure. The peaks were indexed by the JCPDS database for maghemite (p4332, card#01-089-5892)
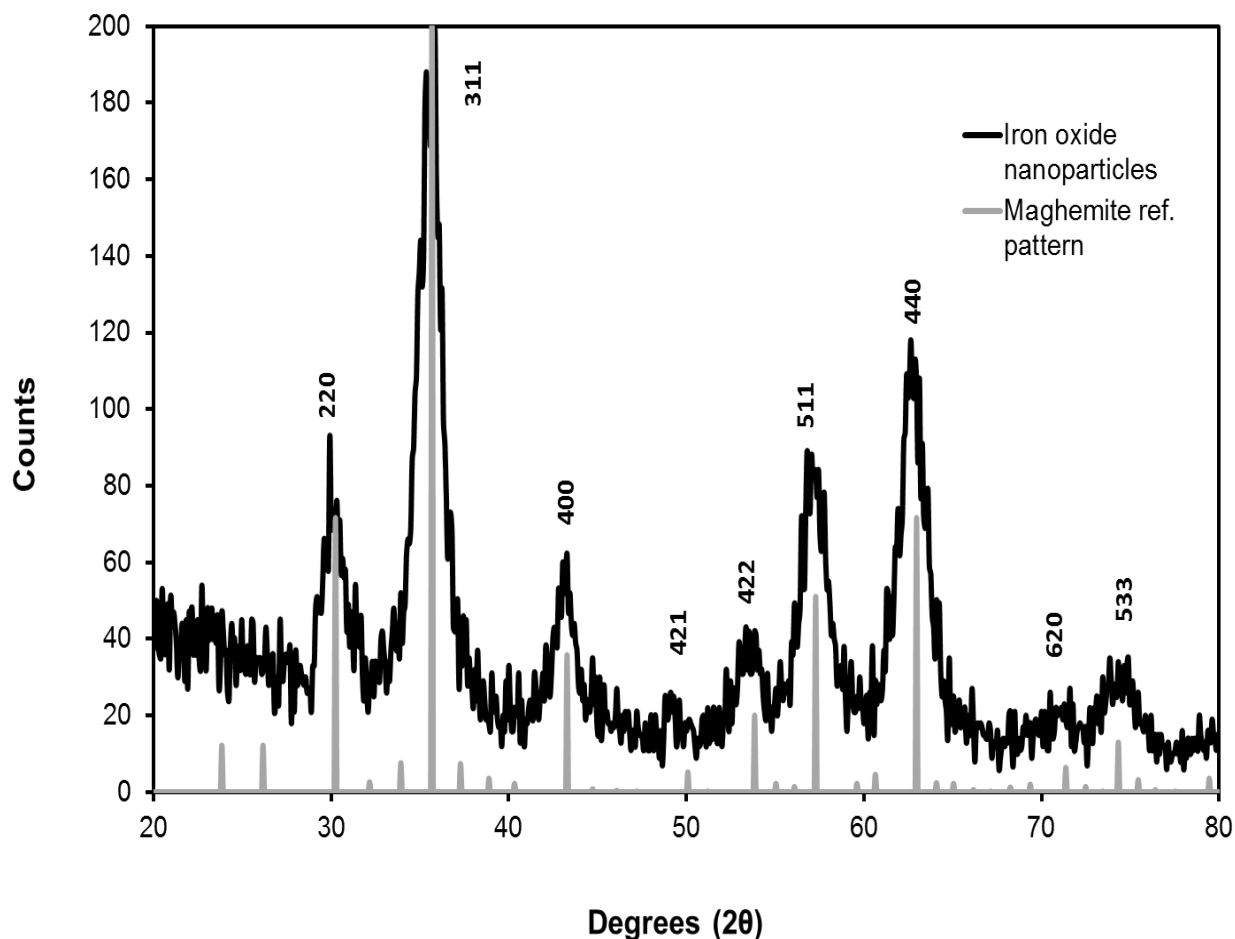
Figure 4-7: XRD pattern of the as-synthesized iron oxide nanoparticles with an overlay of the data obtained from the JSPDS reference powder diffraction pattern of maghemite.

Magnetic characterization was performed by vibrating sample magnetometer (VSM) to confirm that the composites synthesized were indeed magnetic and that the magnetization of iron oxide nanoparticles was retained post polymerization. Figure 4-8 shows a hysteresis plot of the as synthesized iron oxide nanoparticles and the composites with 5% nanoparticles loading, both measured at room temperature. As can be seen, the saturation magnetization of the iron oxide nanoparticles was 62 emu/g and is considered high since bulk maghemite has a magnetization saturation range of 80-100 emu/g. The saturation magnetization of the iron oxide nanoparticles

after polymerization was 6 emu/g and the reduction in the saturation magnetization is due to the magnetic dilution due to the polymeric coating. Utilizing the TGA data for mass correction of the polymer composite sample yielded a magnetization of 60 emu/g of iron oxide in the sample. This shows that the iron oxide nanoparticles remained unchanged during the polymerization process and no significant change is observed on the magnetization of the nanoparticles. Both samples showed a coercivity of roughly 10 Oe at room temperature.
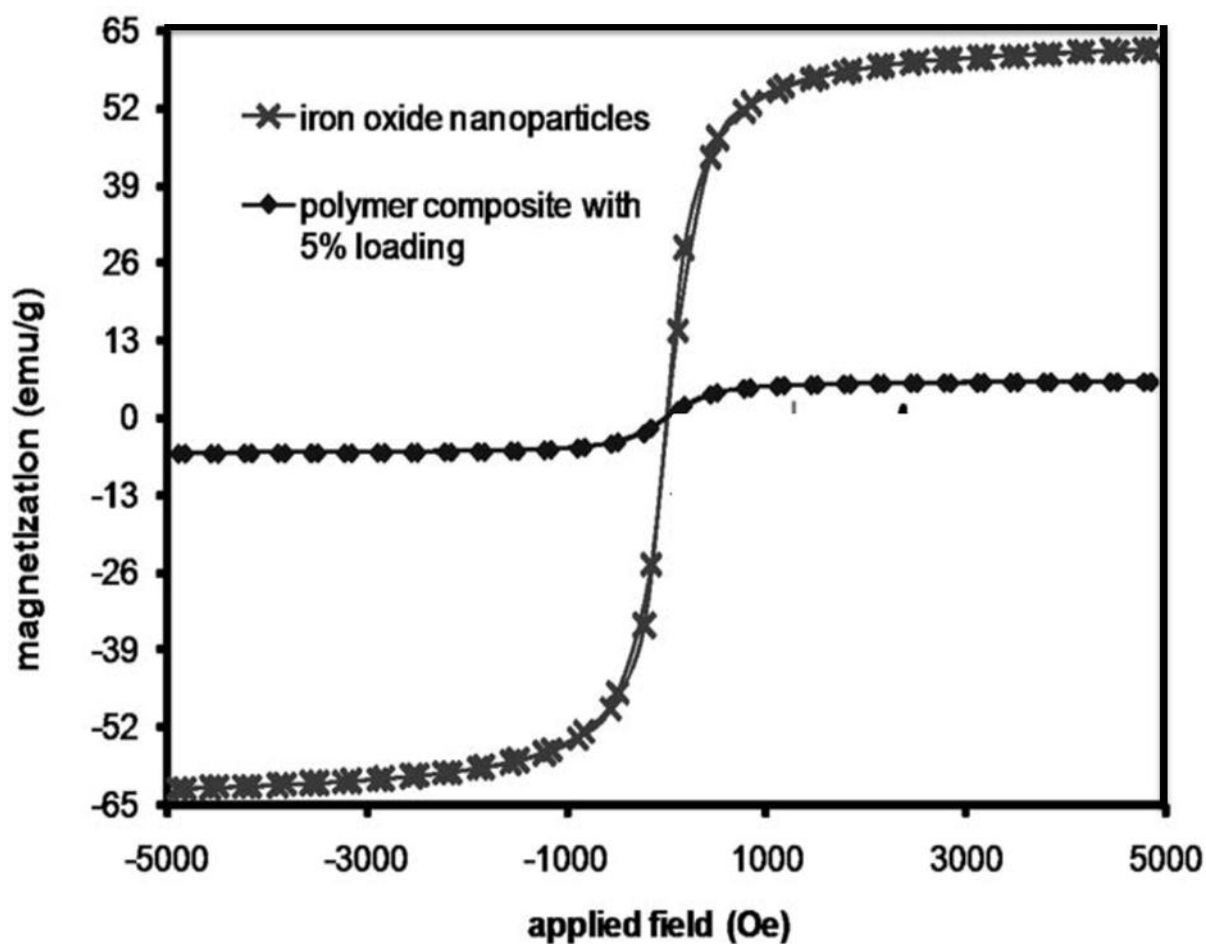
Figure 4-8: Plot of magnetization vs applied field for the as synthesized iron oxide nanoparticles and the nanocomposite synthesized with 5% loading of the iron oxide nanoparticle

4.4. Conclusion

These results discussed indicates that the iron oxide nanoparticles are not just incorporated into the polymer matrix but act as nucleation sites for the polymerization process to begin. Although the polymerization process was found to have no effect on the magnetization of the nanoparticles, the nanoparticles had several effects on the resultant polymer composites size and morphology by decreasing the diameter, increasing the polydispersity, and decreasing the uniformity of the polymer composition. These effects of nanoparticle loading reported give insight into parameters that may need to be adjusted in order to obtain similar polymer sizes, composition, and mechanical properties as nanoparticle loading is increased.

The encapsulation of magnetic iron oxide nanoparticles in the PSVDVB polymer was achieved, but the magnetic PSVDVB composites cannot be utilized for drug delivery applications. PSVDVB polymer is a non-biodegradable polymer. The polymeric composites if introduced parenterally in the body will need to be surgically removed as the polymeric composites will not disintegrate within the body.[153] Due to its non-biodegradability the PSVDVB composites are not suitable for drug delivery applications. Thus, there is a need of a robust biocompatible and biodegradable polymer that can be used for biomedical purposes and will be discussed in chapter 5.

But the PSVBDVB composites with iron oxide nanoparticles can be used for cell separations and as adsorbent for chromatography.[154-156] These application of polymer coated iron oxide nanoparticles will be discussed in chapter 7.

Chapter 5. Poly (D, L-lactide-co-glycolide) microcomposite containing

magnetic iron core nanoparticles as a drug carrier

5.1. Overview

An appropriate selection of the polymer matrix is necessary in order to develop a successful drug delivery system. The polymer can be non-biodegradable or biodegradable. But as discussed earlier the major disadvantage with non-biodegradable polymers is that a surgery is required to harvest these polymers out of the body once they are depleted of the drug. Hence, non-degradable polymers can be used only if removal of the implant is easy.[153] On other hand biodegradable polymers either synthetic or natural, are capable of being cleaved into biocompatible byproducts through chemical or enzyme-catalyzed hydrolysis.[157,158] This biodegradable property makes it possible to inject them into the body without the need of subsequent removal by the surgical operation.[153] Drug delivery systems formulated with these polymers can be released in a controlled manner, by which the drug concentration in the target site is maintained within the therapeutic window. Biodegradation of polymeric biomaterials involves cleavage of hydrolytically or enzymatically sensitive bonds in a polymer, leading to polymer erosion. The erosion of the polymer matrix is usually classified into two categories: bulk (or homogeneous) erosion and surface (or heterogeneous) erosion.[159] Bulk erosion occurs when the rate at which water penetrates into the polymer exceeds the rate at which the polymer is converted into water soluble materials (monomers), resulting in erosion.[160] The size of the polymeric composites remains almost constant in bulk erosion. While surface degradation occurs when the rate at which the polymer penetrates the device is slower than the rate of conversion of the polymer into water soluble materials as shown in Figure 5-1.[160] The rate of degradation of biodegradable polymers is dependent on their hydrophilicity, and on the accessibility of their hydrolytic unstable bonds to water and to specific enzymes that can break these chemical bonds. Consequently, the water uptake capability of the material, its

morphology, crystallinity, and molecular weight are key parameters that determine the degradation kinetics of the polymer.
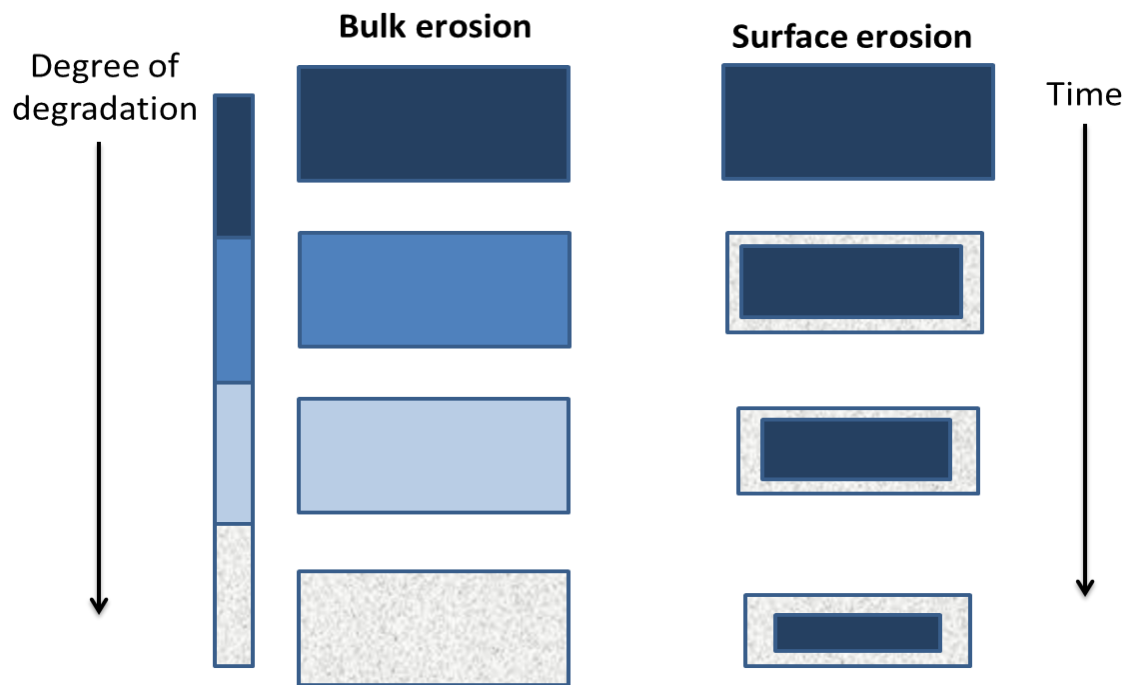
Figure 5-1: Schematic representation of bulk and surface erosion. In bulk erosion the degradation takes place throughout the polymer surface, while surface erosion results in the thinning of the polymeric particle.

5.1.1. Natural polymers

Early research into biodegradable polymeric DDS was mainly focused on naturally occurring polymers like the proteins such as collagen, gelatin, and albumin and polysaccharides such as glucose, dextran, starch, and chitosan.[161] The chemical structures of naturally occurring polymers are shown in Figure 5-2. The application of proteins for drug delivery has been limited due to their low mechanical stability and high cost. On the contrary polysaccharides have attracted researchers as they are commercially available at low cost and can be modified by simple chemical reactions for specific applications. Chitosan a type of polysaccharide has been

much researched as it has shown excellent biocompability, biodegradability, low immunogenicity and biological activity. These naturally occurring polymers mostly undergo degradation through enzymatic bond cleavage.
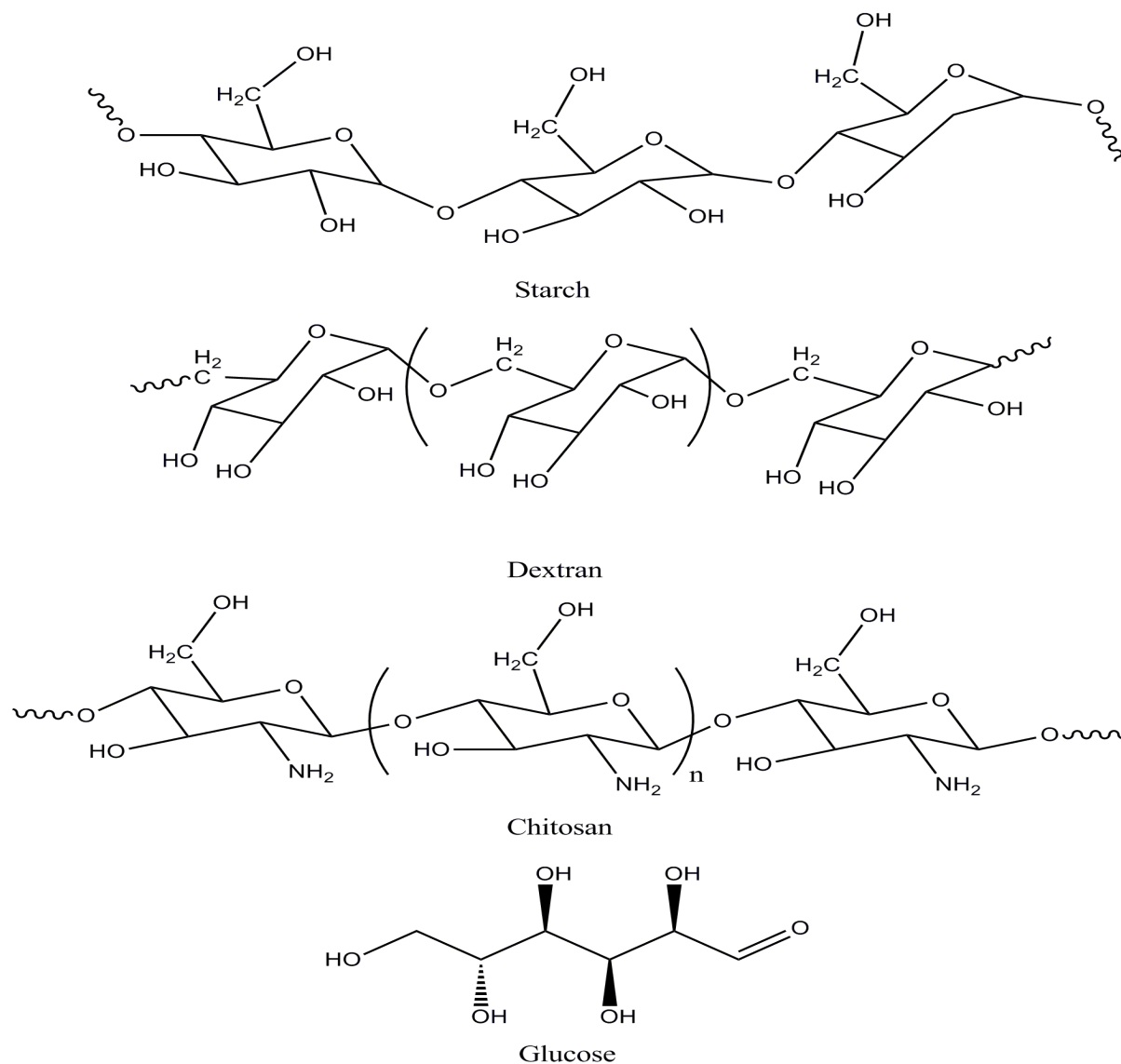
Figure 5-2: Chemical structures of naturally occurring biodegradable polymers

5.1.2. Synthetic polymers

Recently the research focus into biodegradable polymeric DDS has shifted on to synthetic polymers as they offer the advantage of tailoring the degradation process. For synthetic polymers, passive hydrolysis is the primary mode of degradation. In case of degradation by hydrolysis, bulk degradation takes place and can be controlled by applying control over the rate of water penetration and material swelling, which is governed by the hydrophilicity of the polymer.[162,163] Some of the synthetic polymer used for DDS are poly(ortho esters) (POE), polyanhydrides, polyphosphazenes, and aliphatic polyesters.[161]
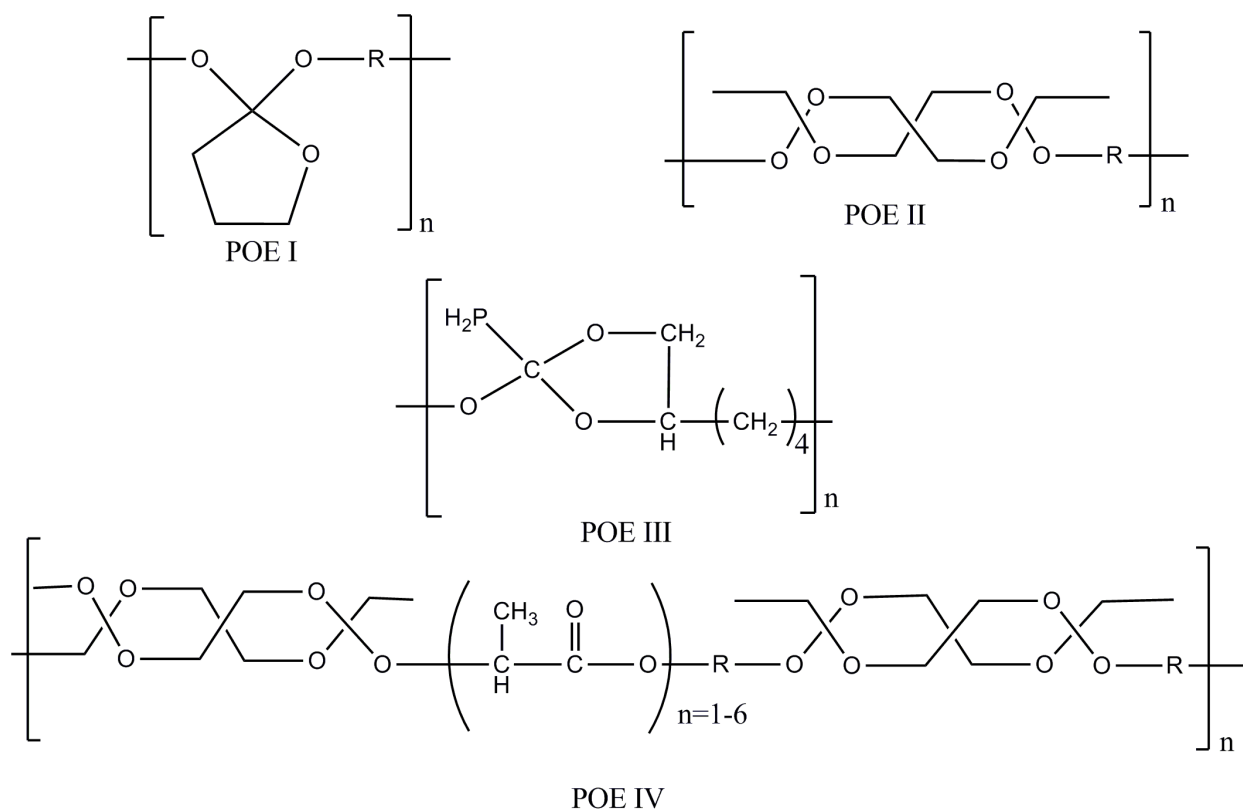
Figure 5-3: Chemical structures of the four generations of poly(ortho)esters (POE)

Poly(ortho)esters (POE) have evolved through four generation as biodegradable polymers and their structures are shown in Figure 5-3.[164] However, only the third and fourth generations

POEs are semisolid and suitable for the manufacturing of a drug delivery system relevant for clinical use. They are easy to manufacture and are characterized by faster degradation rates compared to polyesters.[165] POEs have a degradation span of several days to several months. POEs undergo surface erosion because of high hydrophobicity and water impermeability.[165] In POE composites the drug release and surface erosion of the polymer takes place simultaneously.

Polyanhydrides have been investigated for short term drug release as they undergo rapid degradation *in vivo* and have poor mechanical properties.[166,167] Their main advantage is that they contain the most reactive anhydride groups available for degradation. Polyanhydrides are known to also undergo surface erosion and their degradation rate can be manipulated by varying the polymer composition.[168] The main drawback of these polymers is that they need to be kept frozen under anhydrous conditions because of the dynamic hydrolysis of the anhydride bond. Polyanhydrides have a degradation spam of few days to few weeks.

Polyphosphazenes are liner polymers composed of an inorganic backbone with nitrogen and phosphorous atoms.[169] These polymers can be modified readily by manipulating either the backbone or the side chain, thus enabling the tuning of their degradation rate. These polymers in presence of water cleave into nontoxic, low molecular weight products such as phosphates, and ammonia. Polyphosphazenes can degrade by both bulk and surface erosion depending on the accessibility of the bonds and hydrophobicity of the polymer.[170]

Aliphatic polyesters with hydrolysable backbones are promising candidates for control release DDS. This class of polymers degrades via the hydrolytic cleavage of the ester bonds in their backbone. While the role of enzymatic degradation for this class of polymers is not clearly understood. Some of the widely used aliphatic polyesters are poly(lactide) (PLA), poly(glycolide) (PGA) and the copolymer of PLA and PGA- poly (lactide-co-glycolide) (PLGA)

and their structures are shown in Figure 5-4. These polymers have been used in biomedical

applications for more than 20 years and are known to be biodegradable, biocompatible and non-

toxic, and are approved by FDA (Food and Drug Administration) for human applications.

Poly(glycolic acid)   Poly(lactic acid)

Poly(lactic-co-glycolic acid)
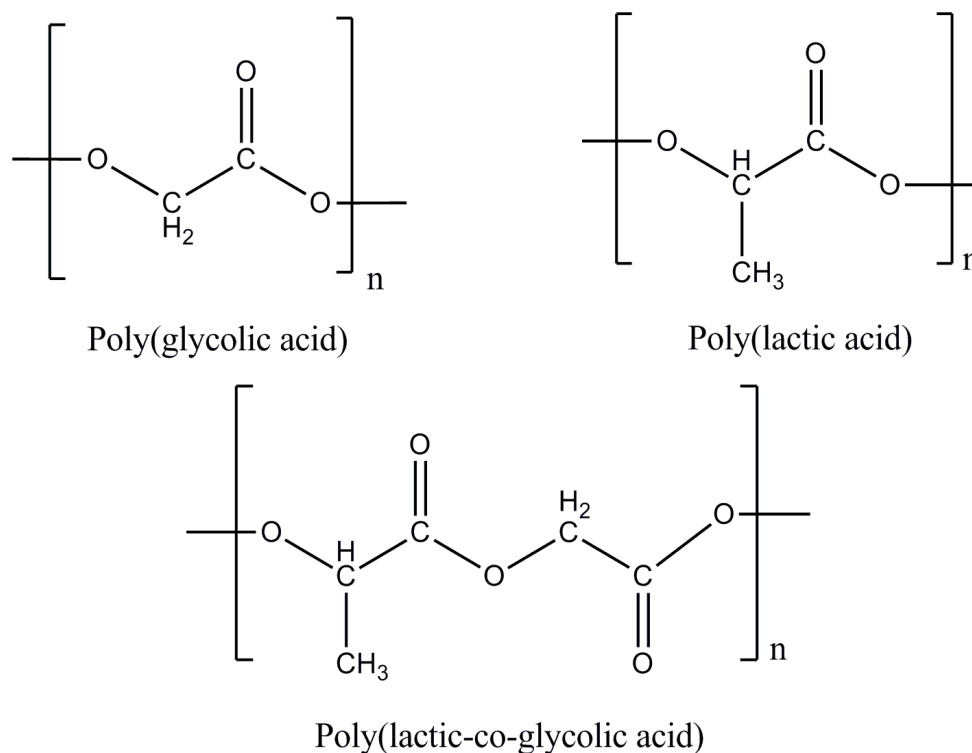
Figure 5-4: Chemical structure of polyesters

Poly(lactide) and Poly(glycolide) are polymer formed by ring opening polymerization of

lactic acid and glycolic acid respectively.[171] They both belong to the α-hydroxy polymer family

and degrade by the hydrolysis of the ester linkage to produce the respective monomers- lactic

acid and glycolic acid. Both of these polymers have been extensively researched as appropriate

candidates for drug delivery matrixes. PLA has three forms due to the presence of a chiral center

D(-), L(+), and racemic (DL) forms.   PGA degrades easily as it is more hydrophilic in nature

due to the absence of the methyl groups while on other hand PLA is found to be more robust in

the body.[172]   PLA takes the longest to degrade biologically, with a biodegradation time of more

than two years while PGA biodegrades relatively quickly, in only two to three month. Because these polymers vary differently in the biodegradation time, their copolymers can be synthesized with a wide-variety of degradation times, depending on the application.

5.2. Poly (lactide-co-glycolide) (PLGA)

Poly (lactide-co-glycolide) (PLGA) is a copolymer of lactide and glycolide, and is synthesized by random ring opening co-polymerization process. Commonly used catalyst for the co-polymerization process are tin(II)2-ethylhexanoate, tin(II) alkoxides, and aluminium isopropoxide. In the co-polymerization process the monomers- lactide and glycolide are linked together by ester linkage yielding a linear, amorphous PLGA polymer as shown in Figure 5-5.
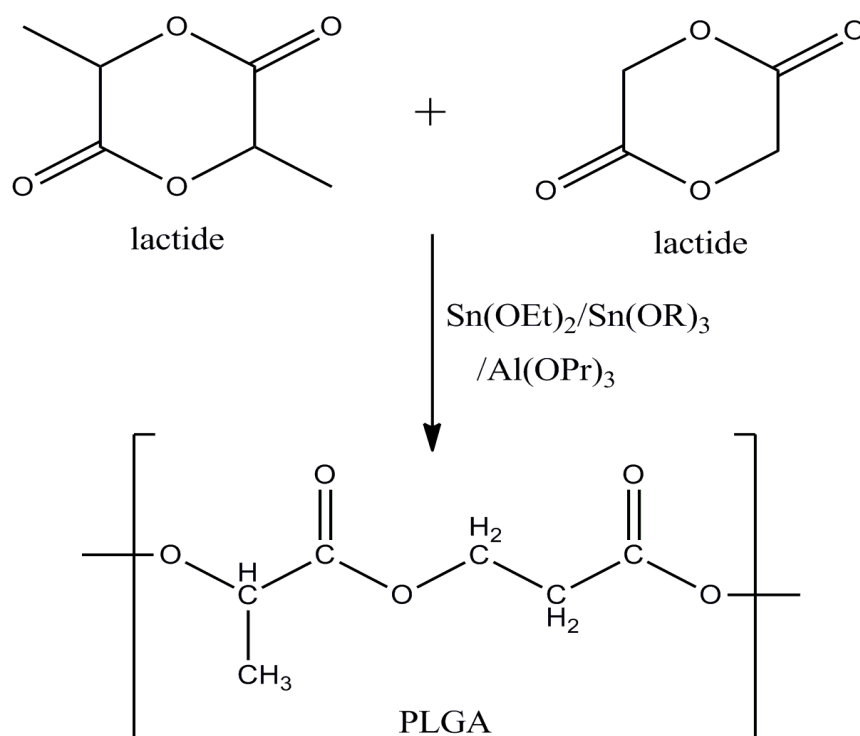
Figure 5-5: Ring opening co-polymerization process of lactide and glycolide in presence of catalyst to obtain PLGA

The forms of the PLGA are identified by the composition of the monomer used such as PLGA 50:50 or PLGA 75:25. The degradation rate and the mechanical properties of the polymer can be influence by varying the monomer ratio (ratio of lactide: glycolide) and by controlling the monomer stereochemistry, molecular weight, and degree of polydispersity. For example PLGA 50:50 has the fastest degradation time of about 50-60 days and likewise PLGA 65:35, 75:25, 80:20, and 90:10 have progressively longer degradation time.[173] PLGA undergoes bulk degradation through random hydrolysis of the backbone ester linkage in presence of water to produce the original monomers. The degraded monomers- lactic acid and glycolic acid are easily metabolized into the body via the Krebs cycle and are eliminated.[174] Thus there is minimal systemic toxicity associated with using PLGA for biomedical applications. Also the original shape and mass of the polymer is preserved until 90% degradation has occurred. The general properties and degradation rate of PLGA, PLA and PGA are summarized in Table 5-1.

Polymer	Crystallinity	Tg (ºC)	Degradation rate
PGA	Highly crystalline	35-40	2-3 months
PLLA	Semi-crystalline	60-65	> 2 years
PDLLA	Amorphous	55-60	12-16 months
PLGA	Amorphous	45-55	1-6 months

Table 5-1: General properties of the polyester polymers- PGA, PLLA, PDLLA, PLGA and their respective degradation rates

PLGA composites can be synthesized by various techniques such as emulsification solvent evaporation technique, salting out, spray drying, nano-precipitation techniques as discussed in chapter 1. The emulsion solvent evaporation technique is the most frequently used

to produce polymeric composites. This technique is simplest of all and encapsulation of the therapeutic and imaging agent can be carried out with ease. The physical properties of obtained composites are strongly dependent on the nature of materials and also on the parameters during the manufacturing of the composites.

This chapter focuses on the preparation of biodegradable and biocompatible PLGA composites for drug delivery applications.[78] For this work the emulsion solvent evaporation technique was used to produce the PLGA composites containing the metallic iron nanoparticles and ruthenium dye as the drug analog. The iron-iron oxide core shell nanoparticles (Fe@FeOx) were used as imaging and heating agents as discussed earlier. Fe@FeOx core shell nanoparticles were used instead of iron oxide nanoparticles as they possess superior magnetic properties due to the formation of metallic iron core. The Fe@FeOx core shell nanoparticles were synthesized by reverse micelle technique and will be discussed in synthetic section.

5.3. Tris-(2,2'bipyridyl)dichlororuthenium (II) [Ru(bpy)$_3$]$^{2+}$ dye
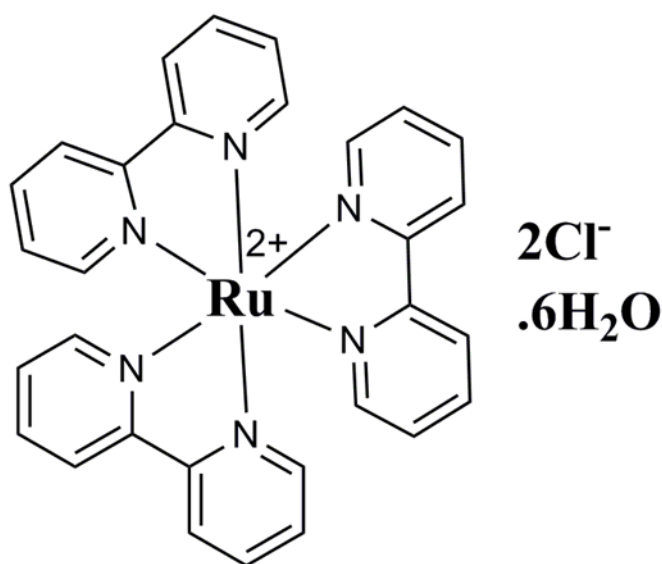
Figure 5-6: Chemical structure of Tris-(2,2'bipyridyl)dichlororuthenium (II) [Ru(bpy)]

Tris-(2,2'bipyridyl)dichlororuthenium (II) $[Ru(bpy)_3]^{2+}$ is a ruthenium based metal complex dye, and its structure is as shown in Figure 5-6. It is a red crystalline salt obtained as a hexahydrate. Ru(bpy) was used as the drug analog, as it is a fluorescent dye so its release from the polymeric composites can be easily monitored through fluorescence spectroscopy. In aqueous solution the $[Ru(bpy)_3]^{2+}$ cation has an excitation wavelength of 470 ($\pm$3) nm. Due to the absorption of visible light by $[Ru(bpy)_3]^{2+}$ leads to the formation of the charge transfer excited state $*[Ru(bpy)_3]^{2+}$ as shown in Eq. 5-1

$$[Ru(bpy)_3]^{2+} + h\nu \longrightarrow *[Ru(bpy)_3]^{2+} \qquad\qquad 5\text{-}1$$
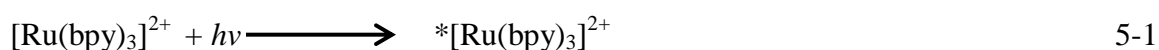
The excited state has a life time of about 890 nano seconds and then relaxes back to the ground state by emission of photons at a wavelength of 610 nm as shown in Eq. 5-2.

$$*[Ru(bpy)_3]^{2+} \longrightarrow [Ru(bpy)_3]^{2+} + h\nu' \qquad\qquad 5\text{-}2$$
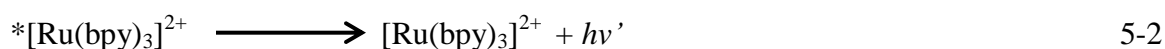
However, if a quencher is present, the excited state will decay to the ground state more rapidly due to the formation of electron transfer complex. The reaction can be shown as in Eq. 5-3.[175]

$$*[Ru(bpy)_3]^{2+} + Q^{(n)+} \longrightarrow [Ru(bpy)_3]^{2+} + Q^* \qquad\qquad 5\text{-}3$$
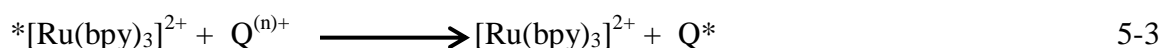
The excited $*Ru(bpy)_3$ can act as both electron donor and electron acceptor species. A variety of inorganic and organic species such as metal ions, and oxygen can act as quenchers.[176] The efficiency of the electron transfer quenching is governed my factors such as distance between the donor and acceptor, degree of quantum mechanical coupling between the molecular orbitals of donor and acceptor as well as the free energy change (ΔG°) for the reaction.[177,178]

In this work the fluorescent Ru(bpy) dye was used as drug analog to study its release from the PLGA composites when irradiated with microwave radiation. The Fe@FeOx nanoparticles quench the fluorescence of the Ru(bpy) dye through charge transfer quenching.

The Fe@FeOx nanoparticles and the Ru(bpy) dye are closely packed within the composites so the donor acceptor distance is reduced thus increasing the rate of charge transfer.

5.4. Synthesis

Iron-iron oxide core shell nanoparticles (Fe@FeOx) nanoparticles were synthesized by reverse micelle technique. Before describing the reverse micelle synthetic technique a brief overview of the technique will be provided in section 5.3.1. The PLGA composites with the Fe@FeOx nanoparticles and the dye were prepared by emulsion solvent evaporation technique and will be discussed in section 5.3.3. PolyD,L-lactide-co-glycolide 50:50 i.v (PLGA) was obtained from Polysciences, Inc. Poly (vinyl alcohol) (PVA) 88% hydrolyzed with an average molecular weight of 88,000 and anhydrous dichloromethane (DCM) were purchased from Arcos organics. Tris-(2,2'bipyridyl)dichlororuthenium (II) [Ru(bpy)$_3$Cl$_2$·6H2O] was purchased from Sigma Aldrich. All chemicals were used as received without further purification

5.4.1. Overview of Reverse micelle technique

Reverse micelle technique has been utilized to synthesis the iron-iron oxide core shell nanoparticles. The main advantage of this technique is that the size distribution can be improved even in room temperature reactions. Normally if the reaction is carried out at room temperature, the nucleation and growth events compete greatly expanding the size distribution of nanoparticles synthesized. It is also cost effective, fast reaction requiring simple equipment and it does not require temperature or pressure control. The reverse micelles isolate reactants from one another, thereby better regulating the nucleation and growth at lower temperatures. A proper understanding of the reverse micelle and the processes involved is essential.
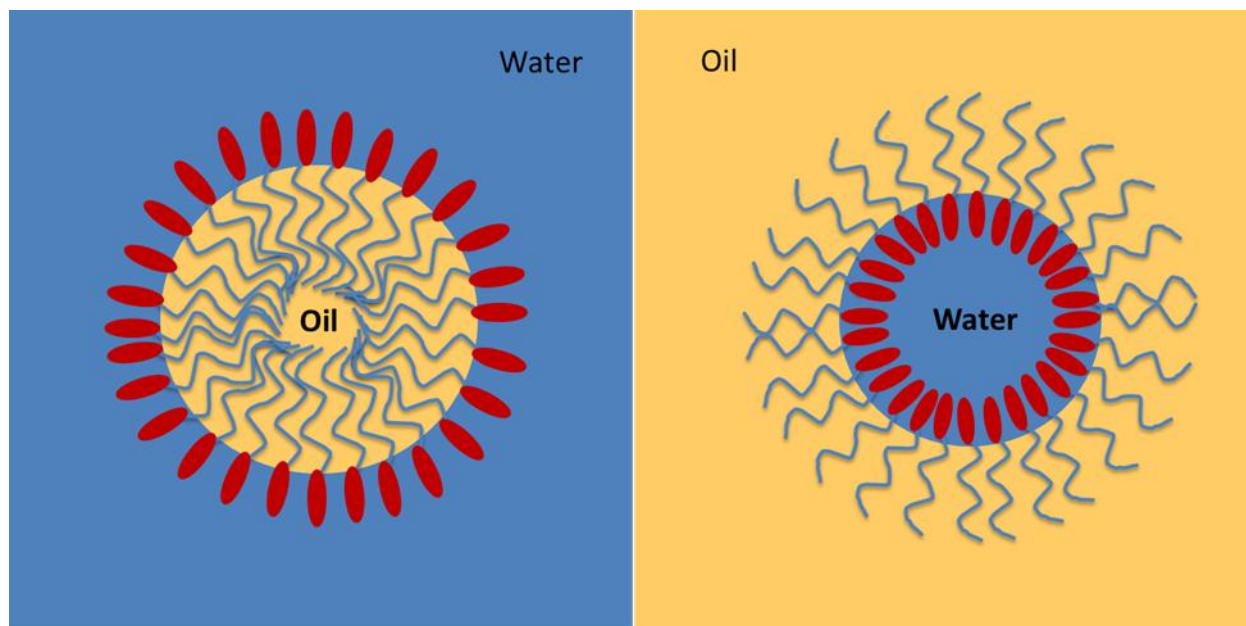
Figure 5-7: Schematic representation of water in oil reverse micelle (right) and oil in water micelle (left)

Micelles are formed when an oil phase, aqueous phase, and the surfactant are mixed in a proper proportion. The surfactant is required to have an affinity for both the aqueous and oil phases, and it acts to provide the barrier between the primarily immiscible phases. Micelles are formed when the concentration of the surfactant exceeds the critical micelles concentration (CMC) in water. There are several types of surfactant used for reverse micelles that can be categorized into four groups: cationic, anionic, nonionic and zwitterionic. In normal micelles the surfactant's hydrophobic tail is directed toward the interior part and the hydrophilic head is directed towards the surrounding aqueous phase. Alternatively, in reverse micelles, the hydrophilic head of the surfactant is directed towards the interior of the micelles and the hydrophobic tail is directed to the oil phase. Figure 5-7 shows the difference between normal micelles (left) and reverse micelles (right). The reverse micelle droplets that are formed act as nano-reaction vessels in which the nanoparticles synthesis can be carried out. The size of the

nanoparticles formed can be controlled by controlling the size of the formed reverse micelles. The reverse micelles can also exist as dimers for nanoseconds during which some exchange of materials between the micelles takes place allowing for sequential synthesis techniques.[179] Also as the reverse micelle reaction takes place in aqueous media, so variety of chemical reactions such as oxidation- reduction, co-precipitation, and substitution reaction can be easily carried out.[114]

5.4.2.Iron-iron oxide (Fe@FeOx) core shell nanoparticles synthesis via reverse micelle

Iron-iron oxide (Fe@FeOx) core shell nanoparticles were synthesized via reverse micelle techniques under nitrogen using Schlenk line techniques as found in the literature.[180,181] The surfactants used for this synthesis were nonylphenoxy poly(ethyleneoxy)ethanols with differing head group repeating units of 9 and 5 as surfactant and co-surfactant (NP9/NP5) sold by Rhodia Incorporated under the name Igepal CO-520 and CO-630 as shown in Figure 5-8. Cyclohexane was used as the solvent.
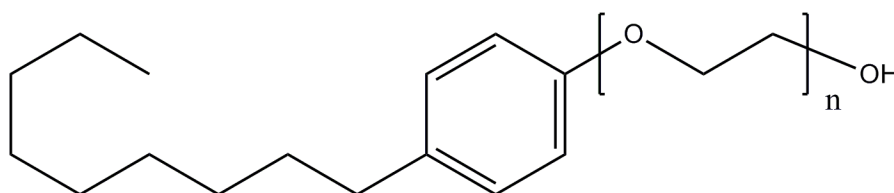
n= 5 & 9, NP5 & NP9

Figure 5-8: Nonylphenoxypoly(ethyleneoxy)ethanols abbreviated as (NP). The "n" represents the number of the ethylenoxy repeating units.

Surfactant solutions were prepared by dissolving 6.85 g of NP5 and 20.57 g of NP9 in 123.23 mL of cyclohexane. In a typical reverse micelle reaction two surfactant solutions are required. The first solution is place into a 1000 mL three necked round bottom flask under

magnetic stirring. The surfactant solution is degassed for about 20 minutes with nitrogen (N_2) utilizing the schlenk line technique. Aqueous metal solutions were prepared by dissolving 0.95 g of $FeCl_2.4H_2O$ in 6.85 mL of water and 0.57 g of $NiCl_2.4H_2O$ in 6.85 mL of water. The other surfactant solution was stirred vigorously while slowly adding the Ni^{2+} solution. Once the solution formed micelles and became clear, it was placed in an addition funnel above the round bottom flask and degassed in the same manner.

Next the aqueous Fe^{2+} solution was added to the first surfactant solution and degassed for 5 minutes. The colorless surfactant solution presented in the reaction vessel turned pale green upon the addition of Fe^{2+} solution. At this point the reverse micelles start to form around the aqueous Fe^{2+} solution. Then 0.36 g of $NaBH_4$ was added to the flask and allowed to react for 20 minutes, at the end of which the micelle solution in the addition funnel containing the Ni^{2+} was added to the reaction for 5 minutes. The addition of second surfactant containing Ni^{2+} aids in the formation of the FeOx shell and passivation of the nanoparticles against further oxidation. The reaction was quenched by the addition of 100 mL of chloroform and 100 mL of methanol and subsequently washed with methanol to remove excess surfactant and cyclohexane, and then, the resultant particles were collected in methanol by magnetic separation. After washing was complete the remaining methanol was decanted and the particles were dried in a vacuum desiccator. As shown in the Figure 5-9, the as synthesized Fe@FeOx core shell nanoparticles were dispersed in 0.50 M sodium hydroxide (NaOH) solution and then treated with equivalent grams of sorbitol and were sonicated for 4 hours. The Fe@FeOx nanoparticles were first coated with sorbitol to provide a negatively charged particle surface for the Ru(bpy) dye adhere to the particle surface. The sorbitol treated nanoparticles were then magnetically separated and 50.00 mg of Ru(bpy) dye in 2 mL of water was added. The nanoparticle dye mixture was further

sonicated for 4 hours and freeze dried to obtain the nanoparticle dye mixture. The next step is the encapsulation of this nanoparticle dye mixture by PLGA polymer. The encapsulation was achieved by emulsification solvent evaporation technique as discussed in chapter 1.
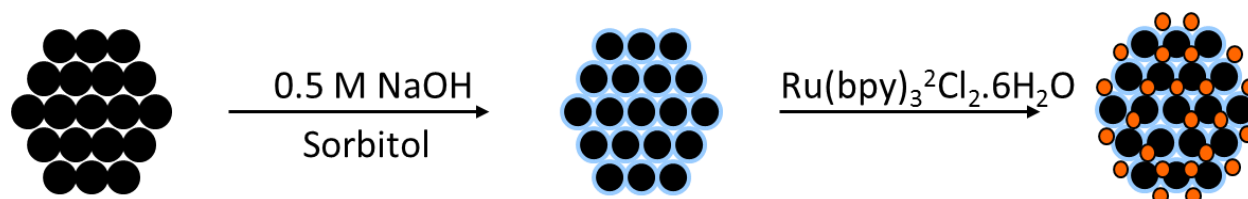
Figure 5-9: Schematic representation of the Fe@FeOx nanoparticle and Ru(bpy) dye mixture

5.4.3. Overview of Emulsification solvent evaporation technique

The encapsulation of the Fe@FeOx nanoparticles and Ru(bpy) dye by PLGA polymer was achieved by emulsification solvent evaporation technique. Emulsification is a process of dispersing two immiscible liquids. For emulsion solvent evaporation there are basically two systems to choose: oil-in-water (o/w) and water-in-oil (w/o). The o/w systems are widely used compared to w/o systems due to the simplicity of the process and easy clean up requirements for obtaining the final polymeric particles. In this process the active agents should be hydrophobic and a water immiscible solvent should be used. In this research work the oil-in-water emulsion solvent evaporation technique was used to obtain PLGA composites containing Fe@FeOx nanoparticles and the Ru(bpy) dye. Dichloromethane (DCM) is the most commonly used water immiscible solvent for preparation of PLGA particles.

The oil-in-water emulsification solvent evaporation technique consists of four major steps. First step is the dissolution of the active agent in an organic solvent (dichloromethane) containing the polymer. Second step is the emulsification of this organic phase, called dispersed

phase, in an aqueous phase called continuous phase followed by extraction of the solvent from the dispersed phase by the continuous phase, accompanied by solvent evaporation, transforming droplets of dispersed phase into solid particles. The final step is the recovery and drying of composites to eliminate the residual solvent.

5.4.4. Preparation of PLGA composites containing Fe@FeOx nanoparticle and Ru(bpy) dye mixture

Figure 5-10 shows the schematic representation of the o/w emulsion solvent evaporation technique used to prepare the PLGA composites. The polymer solution was formed by dissolving 2 wt% of PLGA in dichloromethane (DCM). The organic phase was formed by combining 50.00 mg of the nanoparticle-dye mixture and 3 mL of PLGA solution. This organic phase was sonicated for 5 minutes to achieve uniform dispersion. This organic phase was then added to 50 mL of aqueous phase containing 3% w/v poly(vinyl alcohol) (PVA) as the stabilizer, to form the oil-in-water emulsion. PVA helps to reduce the surface tension of continuous phase, avoids the coalescence and agglomeration of the emulsion droplets formed and stabilizes the emulsion. The emulsion was homogenized with Ultra Turrax IKA T-18 basic homogenizer at 22,000 rpm for 5 minutes. After that 100 mL distilled water was added to the oil-in-water emulsion, which dilutes the organic solvent concentration in water and leads to the hardening of the composites. The solution was stirred overnight to evaporate the organic solvent (DCM) and then freeze dried. The loading efficiency of the iron core nanoparticles and the thickness of the PLGA coating can be controlled by varying the ratios of PLGA, iron nanoparticles, and the fluorescent dye. All characterization and evaluation studies described below were done utilizing the freeze dried PLGA composites.
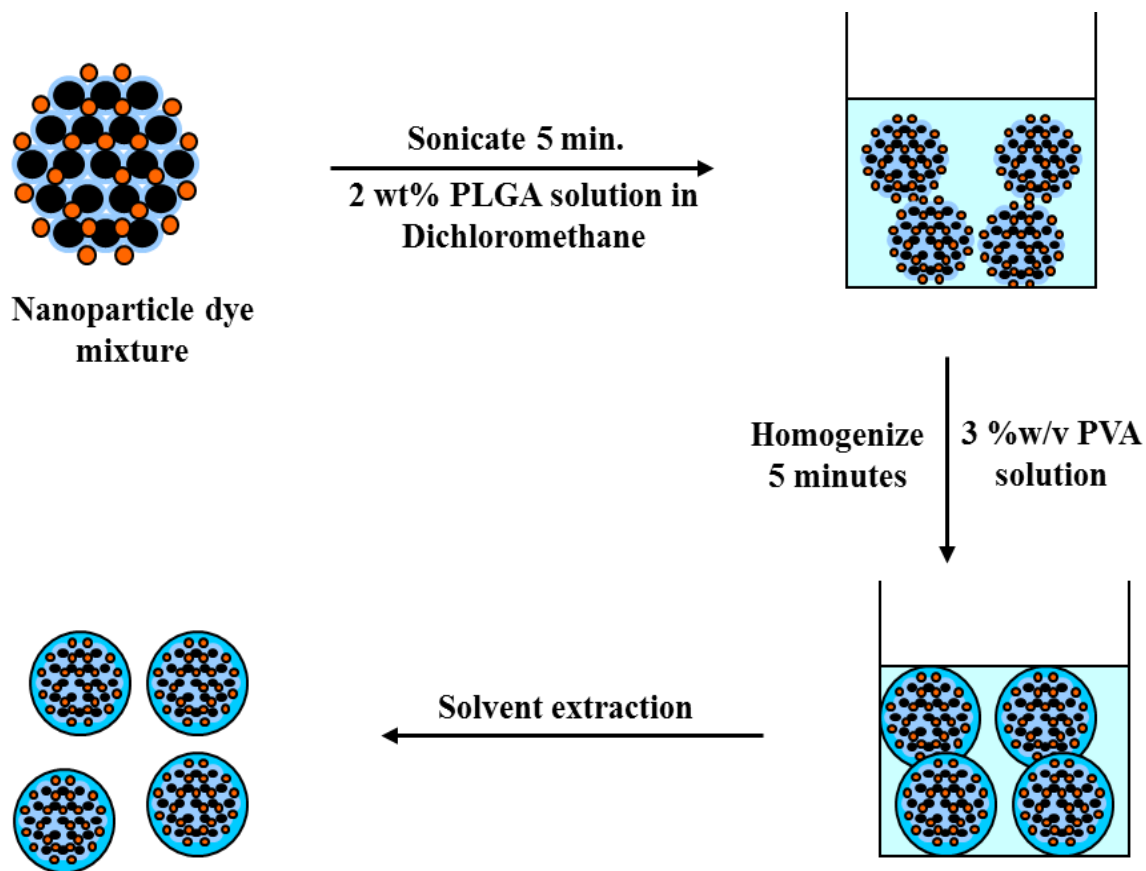
Figure 5-10: Schematic representation of oil-in-water (o/w) emulsion solvent evaporation technique utilized for the encapsulation of the Fe@FeOx nanoparticles and Ru(bpy) dye into PLGA polymer

The size distribution and the morphology of the prepared PLGA composites were determined using a scanning electron microscope (SEM) with a Zeiss EVO 50 (Carl Zeiss, Inc.). The core-shell morphology and size of the nanoparticles were determined by transmission electron microscope (TEM) with a Joel JEM-1230 (Joel Ltd.). The loading efficiency of the iron nanoparticles and the dye, and the release rate of the dye were determined by fluorescence spectroscopy and thermogravimetric analysis (TGA)

5.5. Results and discussion

The size and morphology of the as synthesized Fe@FeOx core shell nanoparticles was confirmed by transmission electron microscopy (TEM). The TEM sample was prepared by re-dispersing the Fe@FeOx nanoparticles in methanol, and then applied to a 300 mesh copper TEM grid with a carbon film. Figure 5-11 shows the TEM image of the Fe@FeOx core shell nanoparticles. A well-defined core shell nanostructures with a size distribution in the range of 10 to 15 nm is observed. The inner dark centers represent the metallic iron core and the outer light color rings represent the iron oxide shell. These results confirm the core shell morphology of the synthesized Fe@FeOx nanoparticles.
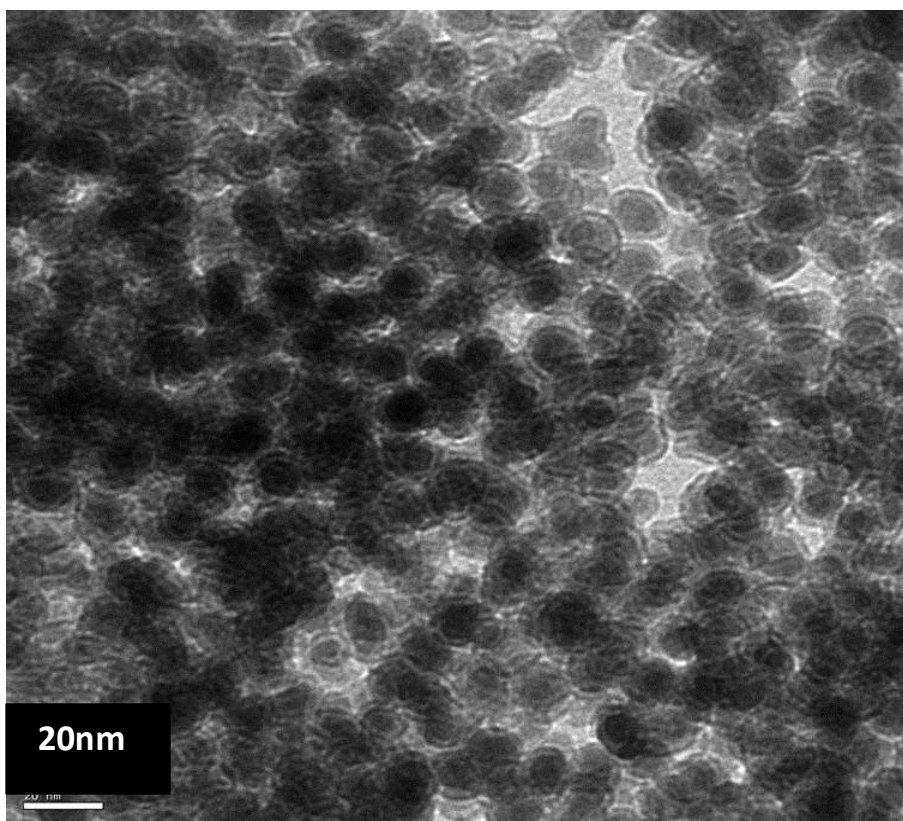
Figure 5-11: Transmission electron microscopy (TEM) image of Fe@FeOx core shell nanoparticles synthesized by reverse micelle technique.

Scanning electron microscopy (SEM) was performed to determine the size distribution and the morphology of the prepared polymeric composites. The freeze dried PLGA composites were re-suspended in water with sonication, mounted onto a carbon conductive tab (Ted Pella, Inc., Redding, CA, USA), and dried at room temperature overnight. The sample was sputter coated with gold plasma prior to SEM imaging. Figure 5-12 shows the SEM image of the magnetic PLGA composites, which are roughly around 200 nm–1.5 μm in size and show fairly spherical structure. The size distribution of the composites is attributed to the oil-in-water droplet formation and the solvent evaporation from the polymer solvent interface. In general, longer homogenization times and higher speed of the homogenizer produces higher shear induced by the homogenizer blade, thus, leading to smaller particle size. Too much loading of the Ru(bpy) dye and the nanoparticles leads to the loss of morphological control and the composites turn into irregular shapes as seen in the Figure 5-12. The most likely explanation to this would be that the Ru(bpy) dye could precipitate in due to lack of water during the Fe@FeOx nanoparticle-Ru(bpy) dye mixture formation. The particle size of the precipitated dye could be bigger than the oil-in-water bubbles formed. Thus disturbing the droplet formation and leading to smear formation. The other speculation is that as the dye content is increased in the organic phase, more dye is likely to get solubilize into the aqueous phase as Ru(bpy) is a water soluble dye. This leads to the disturbance in the formation of the droplet.
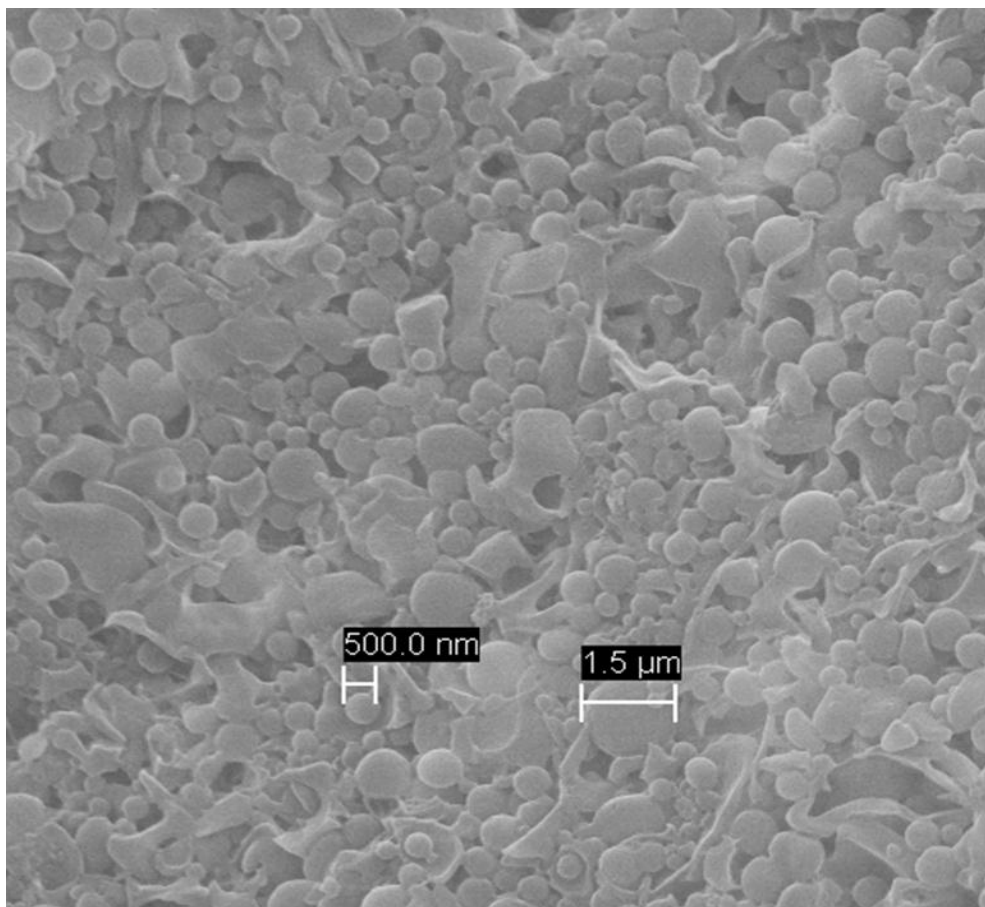
Figure 5-12: Scanning electron microscopy (SEM) image of the magnetic PLGA composites

The loading efficiency of the prepared magnetic PLGA composites was determined using Thermogravimetric analysis (TGA) and fluorescence spectroscopy. 5 mg of the PLGA composite were dissolved in DCM; PLGA is soluble in DCM while the Fe@FeOx nanoparticles and the Ru(bpy) dye fall out in the organic solution. To this DCM solution a known volume of water was added to extract the water soluble Ru(bpy) dye. Fluorescence measurements were performed on the aqueous layer to determine the Ru(bpy) dye content in 5 mg of the composites. Fluorescence intensity of known concentration of Ru(bpy) dye was measured and a linear curve fit was performed which yields around 0.25% w/w fluorescent Ru(bpy) dye loading in the composites as shown in Figure 5-13. Attempts were made to improve the loading efficiency of

the dye but it leads to the loss of the spherical morphology of the composites, as discussed earlier.
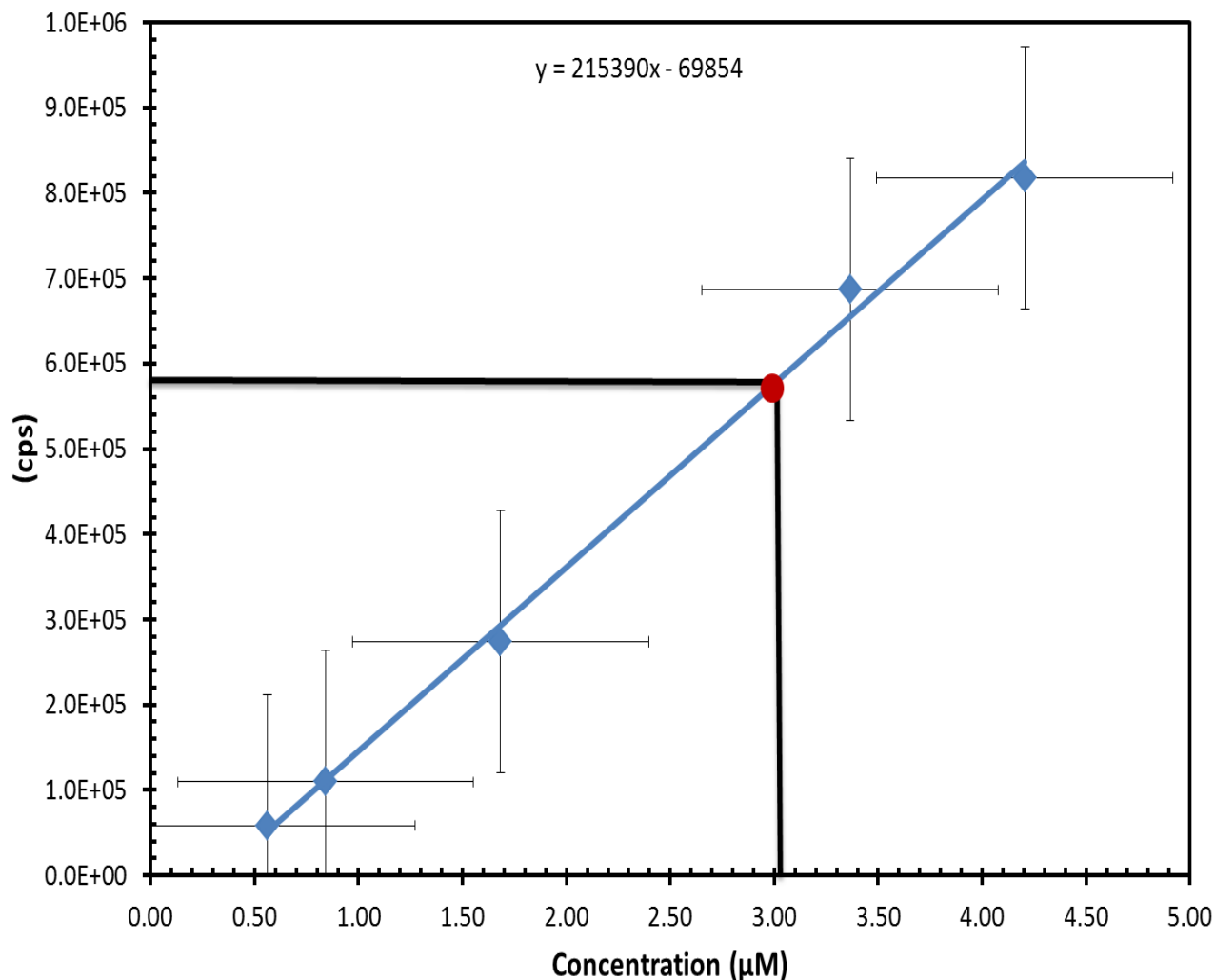
Figure 5-13: Linear regression plot yielding a 0.25% w/w Ru(bpy) loading into the PLGA composites

TGA results also confirmed 0.25% w/w Ru(bpy) dye loading and shows approximately 50% w/w Fe@FeOx nanoparticles loading in the composite as shown in Figure 5-14. The decomposition of PLGA polymer by itself occurs at around 200 ℃, but the PLGA composites start to degrade at around 160 ℃. The PLGA polymer is in a form of amorphous bead but when

the PLGA composites are formed the polymer was dissolved in DCM and re-precipitated out. This causes an increase in the atacticity of the polymer. Two decomposition events around 380 ℃ and 450 ℃ are observed for Ru(bpy) corresponding to the decomposition of the bipyridyl rings. The PLGA composites shows a small decomposition event around 400 ℃ corresponding to Ru(bpy) dye indicating a trivial amount of the dye. The Ru(bpy) dye loading obtained is very less and can be attributed to the loss of the water soluble Ru(bpy) dye during the emulsification process. The Fe@FeOx nanoparticles do not undergo any decomposition till 600 ℃ thus yielding a loading of around 50% in the composite.
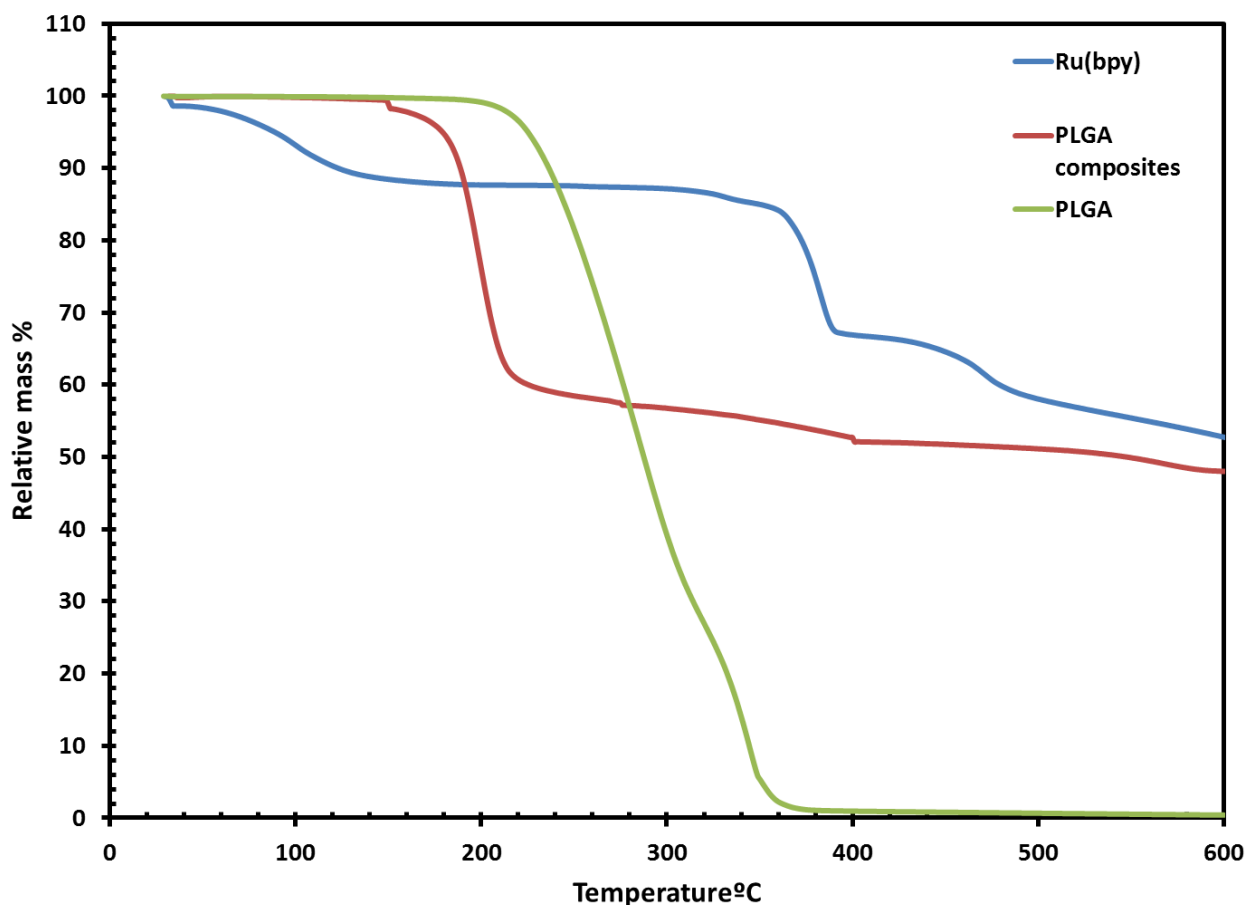
Figure 5-14: TGA plot showing the decomposition profile of PLGA composites containing Fe@FeOx nanoparticles and Ru(bpy) dye, PLGA and Ru(bpy) dye by itself

5.6. Ru(bpy) dye release studies

Fluorescence spectroscopy was performed to study the release kinetics of the Ru(bpy) dye from the PLGA composites. Ru(bpy) dye is a fluorescent dye with excitation wavelength of 470 nm and emission wavelength around 610 nm. Therefore, the PLGA composites were excited at 470 nm using Cary Eclipse Fluorescence Spectrophotometer equipped with a xenon lamp. As the dye is released from the composite, the fluorescence intensity decreases due to the quenching of the Ru(bpy) dye by the Fe@FeOx nanoparticles as discussed earlier, thus allowing for the determination of the release kinetics of the dye as a function of temperature. The PLGA composites were dispersed in water and heated with 2.45 GHz microwave radiations by irradiating with a pulse of 1 second duration each utilizing a commercial microwave unit. The microwave radiations heats up the magnetic nanoparticles by magnetic hyperthermia principle as discussed.
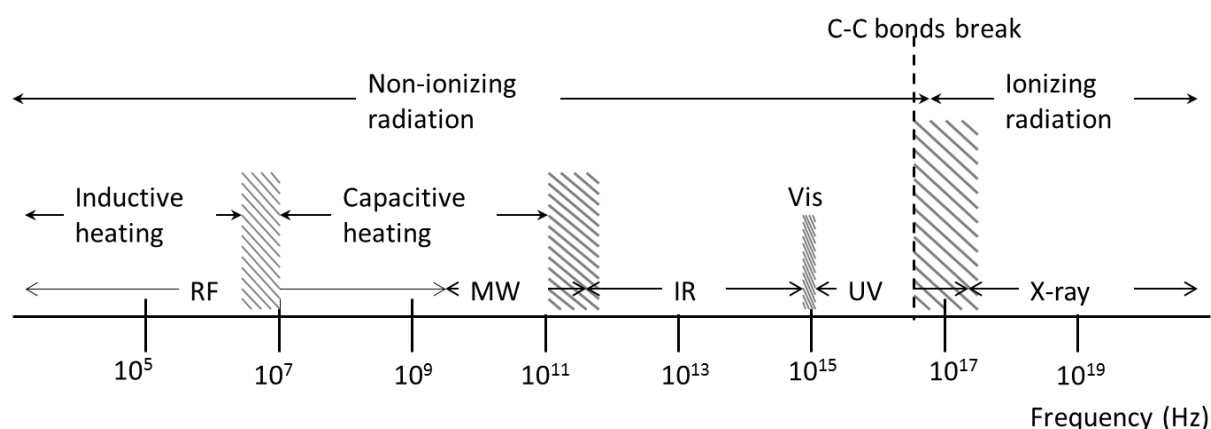
Figure 5-15: Physical mechanism at each frequency range of electromagnetic spectrum range

Electromagnetic (EM) radiation can be classified into ionizing radiation and non-ionizing radiation, based on whether it is capable of ionizing atoms and breaking chemical bonds as shown in the Figure 5-15. Non-ionizing EM radiations propagate within biological tissues with

reduced velocities, and are refracted, diffracted and reflected when encountering in-homogeneities within tissues. For heat generation the non-ionizing radiations of the EM spectrum are widely used by diversified system configurations. Microwave radiations are widely used EM radiation to generate heat within the body. Microwaves are defined as the region of the non-ionizing spectrum from 300 MHz to 30 GHz. Microwaves interact with biological systems by way of ionic conduction and rotation of polar molecules of water. Microwave energy is generated by a magnetron, and transmitted either directly or by means of a waveguide. The Federal Communications Commissions for industrial, scientific, and medical applications has allotted the 0.955 and 2.450 GHz frequency bands for hyperthermia applications.[182] In the 0.915 GHz band, resistive heating is achieved by collision of the freely moving ions within the body while at the 2.45 GHz frequency bands heat is generated but to the dielectric heating of water and fats within the body. Due to this microwave energy leads to overheating of the fatty tissues. Despite these problematic overheating, microwaves are still among the mainstream hyperthermia applications due to several appealing experimental and clinical results. Also the overheating can be controlled by maintaining the exposure time of the microwave radiations as defined by the International Commission on Non-Ionizing Radiation Protection (ICNRP)[183,184]
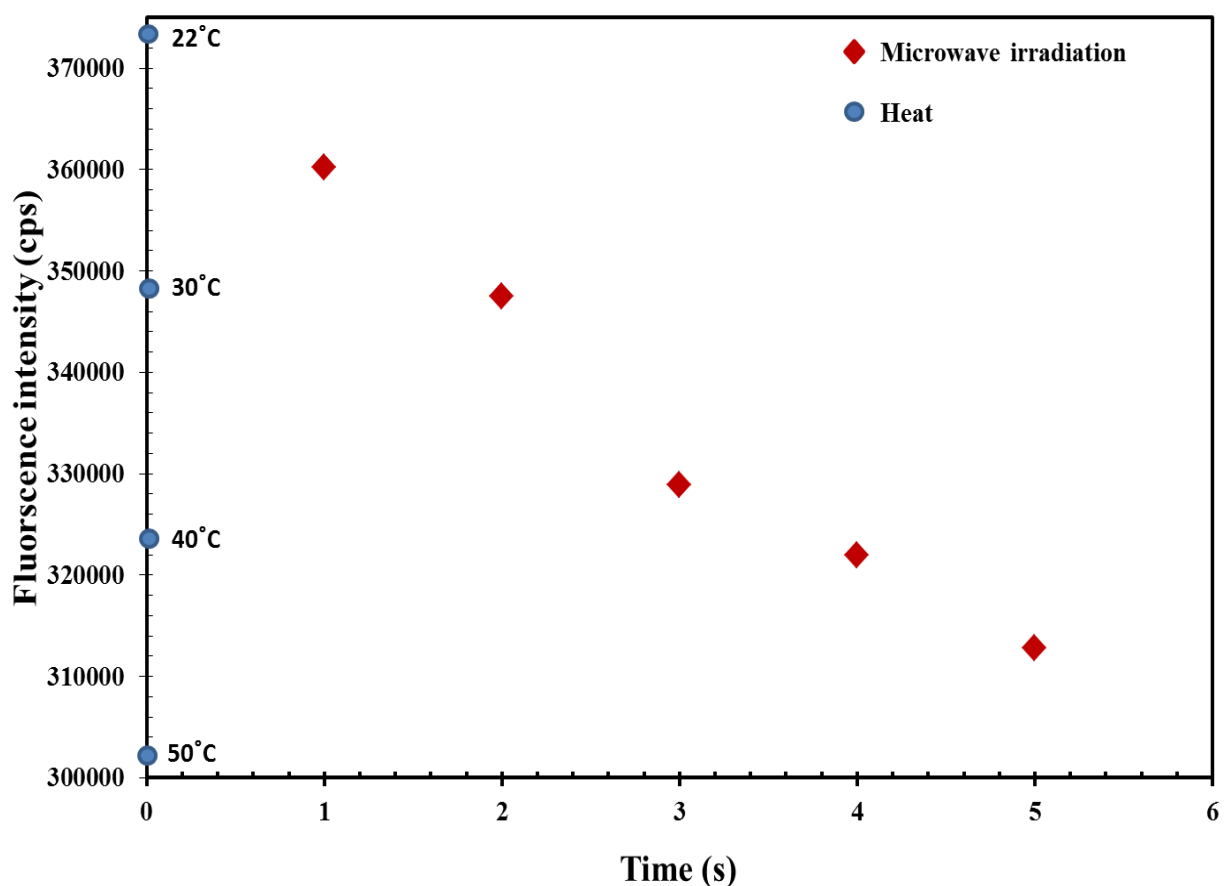
Figure 5-16: Plot of fluorescence intensity vs time. The horizontal lines shows the fluorescent intensity at room temperature 22 °C, 30, 40, and 50 °C temperature as measured by fluorescence spectrometer.

The magnetic nanoparticles when irradiated with the microwave radiations produce heat by magnetic hyperthermia principle as discussed earlier. The 2.45 GHz frequency with 1 second pulse was used for the in-vitro experiments and past studies have shown that few seconds' exposure to the microwave radiations does not have any major effect on the healthy tissue.[185,186] To achieve uniform heating of the composite sample and water as the reference, the turntable within the microwave unit was removed and the composite sample and water were heated from one to five times with a pulse of 1 second duration each. The iron nanoparticles encapsulated within the composite absorb the microwaves and heats up providing local heating. The PLGA

polymer swells up due to the heat produced leading to the release of the dye through the erosion of the polymer. The bulk water temperature of the composite sample as well as the reference reached up to 32 °C after irradiating the sample five times with a pulse of 1 second duration each. Fluorescent measurements were carried out after irradiating the sample for one to five times with 1 second pulse each, as well as heating the sample to 30, 40, and 50 °C. The sample was just heated five times as further heating leads to drastic increase in the temperature of the sample. Figure 5-16 shows the plot of the fluorescence intensity with time of irradiation of the sample by the microwaves and externally heating the sample at 30, 40, and 50 °C. It can be seen that the rate of release of the dye at 2 seconds is equal to that of 30 °C and the 4 seconds irradiation release equals to 40 °C.

5.7. Conclusion

Successful encapsulate the drug analog Ru(bpy) dye and magnetic Fe@FeOx nanoparticles into the PLGA composites was achieved by oil-in-water emulsion solvent evaporation technique. The local heating of the PLGA composites was also achieved by irradiating the Fe@FeOx nanoparticles with 2.45 GHz microwave radiations. The release of the Ru(bpy) dye from the PLGA composites after microwave irradiation was successfully achieved. Also higher Ru(bpy) dye release from the composites by locally heating the sample with 2.45 GHz microwave pulse compared to externally heating the composite sample was demonstrated.

Fe^{2+} and Fe^{3+} ions acts as a very good quencher for the fluorescent Ru(bpy) dye, which is observed with the decrease in the fluorescence intensity of the released dye at 610 nm when the temperature is increased externally or by irradiating the sample five times with 1 second pulse each from a 2.45 GHz commercial microwave unit. The composite sample when irradiated with microwaves or externally heated at 30, 40 or 50 ˚C, the sorbitol layer on the nanoparticles

decomposes at that temperature. The sorbitol was used to provide a barrier between the iron oxide nanoparticles and the Ru(bpy) dye so that they do not come in contact with each other leading to dynamic quenching of the Ru(bpy) dye. The quenching of the Ru(bpy) dye by the iron oxide nanoparticles is observed when the composites are irradiated or heated externally. As a result a systematic study of the quenching process of the ruthenium dye needs to be done. To clearly understand the quenching process of the Ru(bpy) dye in-situ measurements of the dye release need to be done. For this reasons Radio frequency (Rf) radiations were used instead of 2.45 GHz microwave radiations to generate heat from the magnetic iron nanoparticles by magnetic hyperthermia principles. It is easier to mount an Rf frequency coil on the sample carrying out simultaneous heating and fluorescent measurements. Also a bench top fluorescence spectrometer equipped with 530 nm laser source was used to carry out in-situ measurements. An Rf frequency coil was mounted on the sample and then fluorescence measurements are carried out. A detailed explanation of the experimental set up and the results obtained will be given in chapter 6.

Chapter 6. Ferrofluid based drug delivery system with dual modal imaging and therapeutic applications

6.1. Overview

As discussed earlier a drug delivery system made up of biodegradable and biocompatible PLGA polymeric composites containing the Fe@FeOx nanoparticles and the drug analog has been successfully designed. But as seen in the previous results the PLGA composites synthesized were poly-dispersed with a wide size distribution of around 200 nm–1.5 μm. For *in-vitro* applications mono-dispersed PLGA composites with higher dye loading efficiency are desirable. To obtain mono-dispersed PLGA composites, the magnetic Fe@FeOx nanoparticles need to be dispersed in either organic or aqueous medium. The PLGA composites earlier synthesized in chapter 5 were prepared by oil-in-water (o/w) emulsion technique. The basic principle of this technique is that both polymer and the active agents to be encapsulated need to be dispersed/ dissolved into the organic phase (DCM), and the resultant organic phase is emulsified into the water phase containing the emulsifier of choice. In the earlier case when Fe@FeOx nanoparticle-Ru(bpy) dye mixture was encapsulated into the PLGA polymer, the nanoparticle-dye mixture did not form a stable disperse into DCM. So it was a solid-in-oil-in-water (s/o/w) emulsion, in which a solid is dispersed into the organic phase which is then emulsified in the aqueous phase.[187] But the s/o/w technique has certain drawbacks such as formation of poly-dispersed composites and increase in the burst release of the active agent. In s/o/w technique very low and uniform particle size of the active agent is required for the complete encapsulation.[188] Therefore the poly-dispersed in the PLGA composites could have come from the poly-dispersed Fe@FeOx nanoparticle-Ru(bpy) dye mixture. To overcome this problem the nanoparticle-dye mixture needs to be dispersed into the organic phase. The Ru(bpy) dye is soluble in the aqueous as well as organic phase but the Fe@FeOx nanoparticles do not disperse into organic as well as the aqueous phase. So, it is essential to obtain a stable dispersion

of the magnetic nanoparticles into the desired solvent. This can be achieved by using a ferrofluid instead of the iron nanoparticles.

This chapter first describes the synthesis of the chloroform based ferrofluid by thermolysis technique followed by its characterization. The next step is the preparation of the PLGA composites utilizing the synthesized ferrofluid and the drug analog by oil-in-water emulsion solvent evaporation technique. The PLGA composites were further functionalized with folic acid for targeted delivery. The functionalization of the PLGA was achieved utilizing carbodiimide chemistry and will be discussed in detail in section 6.4. The release of the drug analog from the functionalized PLGA composites was studied by fluorescence spectroscopy while placing the sample in a radio frequency (Rf) induction coil. The PLGA composites were also investigated by magnetic resonance relaxivity measurements for its application in MRI

6.2. Ferrofluid

Ferrofluids are stable colloidal suspensions of nanoscale magnetic particles into a carrier fluid, usually organic solvent or water.[148,189] The magnetic nanoparticles have an average particle size of about 10 nm that are suspended by Brownian motion and do not settle out, even when exposed to a strong magnetic, or gravitational field. The magnetic nanoparticles are mainly nanoscale magnetite or maghemite. In the absence of a magnetic field, the magnetic moments of the nanoparticles are randomly distributed and the ferrofluid has no net magnetization. But when a magnetic field is applied to a ferrofluid, the magnetic moments of the nanoparticles orient along the field lines almost instantly. The magnetization of the ferrofluid responds immediately to the changes in the applied magnetic field and when the applied field is removed, the moments randomize quickly.

The magnetic nanoparticles of the ferrofluid are coated with a stabilizing dispersing agent that prevents the particle agglomeration even when a strong magnetic field is applied to the ferrofluid. These stabilizers prevent the nanoparticles from clumping together, ensuring that the particles do not form aggregates that become too heavy to be held in suspension by Brownian motion. There are two main types of stabilizers used for dispersing magnetic nanoparticles such as the surfactant stabilized nanoparticles and ionically stabilized nanoparticles. Tetramethylammonium hydroxide is the most commonly used ionic stabilizer for polar solvents based ferrofluid. The positively charged tetramethylammonium hydroxide $[N(CH_3)_4^+]$ cation forms a diffuse shell around the negatively charged nanoparticle surface, inducing electrostatic repulsion between the neighboring particles. For non-polar solvents based ferrofluid, surfactants are used to coat the nanoparticle surface that induces steric repulsion on the neighboring nanoparticles. The most commonly used surfactants are oleic acid, citric acid, and soy lecithin. A surfactant has a polar head which adsorbs to a nanoparticle and non-polar tail that sticks out into the carrier medium preventing the agglomeration of the nanoparticles. The stability of the ferrofluid is influenced by several parameters such as an optimum size range of the nanoparticles, viscosity of the carrier liquid, length of the surfactant, temperature, and magnetic field strength. Various techniques have been shown to produce magnetic nanoparticles such as wet grinding, co-precipitation, micro-emulsion, and thermal decomposition of metal salts (thermolysis).[189-191] After the synthesis of the nanoparticles, additional steps are typically required to coat them with the appropriate stabilizer.

6.2.1. Synthesis

Thermolysis is a synthetic technique where in the nanoparticles are synthesized by thermally decomposing the metal precursor in high boiling organic solvents containing

stabilizing surfactant.[192,193] Mono-dispersed nanoparticles can be achieved through thermolysis technique. Furthermore, utilizing this technique the surfactant coating of the nanoparticle can be achieved in a single step process.
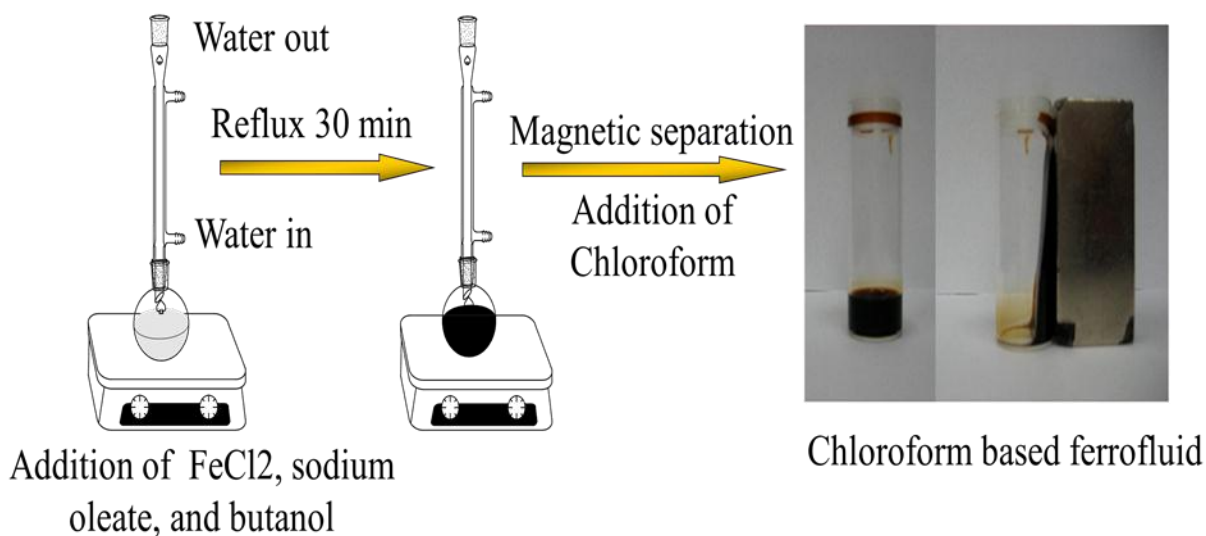
Figure 6-1: Synthetic scheme for the design of the chloroform based ferrofluid
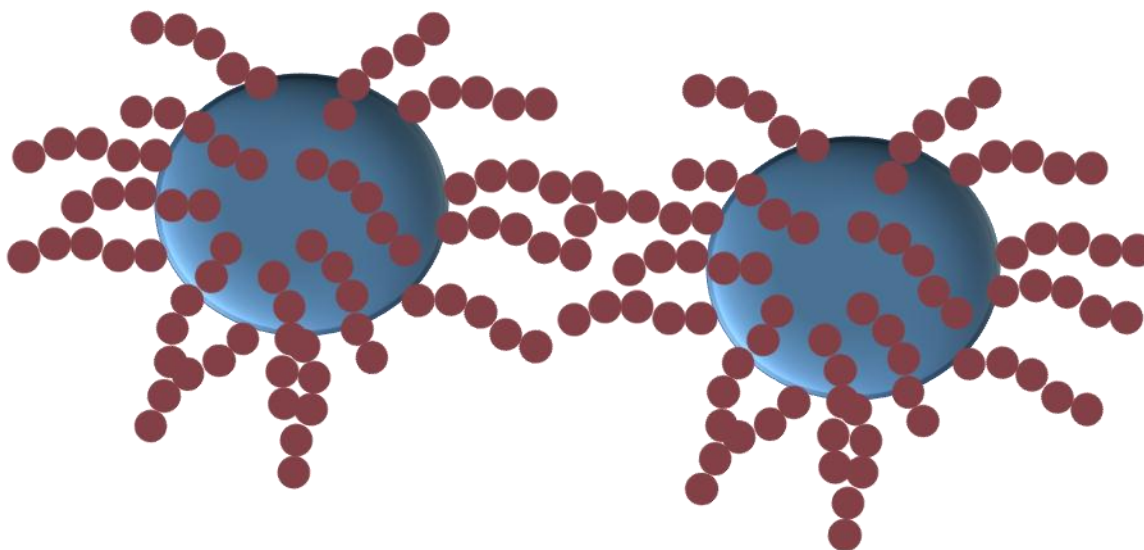
Figure 6-2: Schematic representation of the magnetic nanoparticles coated with sodium oleate in the ferrofluid. The sodium oleate chains induces steric repulsion on the neighboring particles preventing the agglomeration

Chloroform based ferrofluid was synthesized by thermolysis technique under ambient conditions. 1.00 g of iron (II) chloride tetrahydrate (FeCl$_2$.4H$_2$O) and 2.50 g of sodium oleate are placed in a 100 mL one neck round bottom flask. Sodium oleate is used here as a surfactant to coat the magnetic nanoparticles as shown in Figure 6-2. The sodium oleate induces steric repulsion between the neighboring nanoparticles thus preventing agglomeration. Then 25 mL of n-butanol is slowly added to the flask under magnetic stirring. The reaction solution is quickly heated to reflux conditions for an hour. During which the reaction solution undergoes a color change from dark orange to grey and finally to jet black at the end of 1 hour reflux. After an hour the reaction solution was allowed to cool to room temperature and quenched with the addition of 100 mL methanol. Throughout the reaction the particles did not seem to stick to the magnetic stirrer during the reaction. The nanoparticles are magnetically extracted and further washed several times with methanol. The methanol washing step is necessary to remove any excess of the sodium oleate surfactant. To prepare the chloroform based ferrofluid, the nanoparticles were taken in a vial and chloroform was slowly added under sonication. The colloidal stability of the prepared ferrofluid was checked with a rare earth magnet. The resulting ferrofluid is stable for over six months without visual degradation.

The next step is the preparation of the PLGA composites utilizing the ferrofluid and the drug analog. In previous work Ru(bpy) dye was used as the drug analog, but the loading efficiency was too low around 0.25%. Another dye Rose Bengal was used but it also suffered from the same problem of poor loading. Both Ru(bpy) and Rose bengal are water soluble and leached out during the emulsification process leading to poor encapsulation efficiency. Moreover most of the anticancer drugs are water insoluble so we need a water insoluble drug analog. Rhodamine B base is a sparingly soluble in water. Rhodamine B base is a fluorescent

dye belonging to the family of fluorone dyes and its structure is as shown in Figure 6-3. Rhodamine B base has and excitation wavelength around 540 ± 2 nm and emission wavelength around 580 ± 2 nm. Rhodamine B base also undergoes dynamic quenching by Fe^{2+} and Fe^{3+} ions through excited state charge transfer mechanism. [176,194]
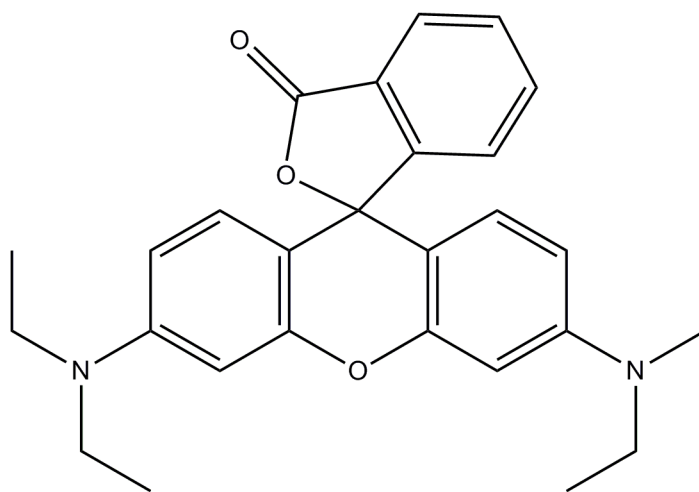
Rhodamine B base

Figure 6-3: Chemical structure of Rhodamine B base dye

6.3. Preparation of the PLGA composites containing the Ferrofluid and Rhodamine B dye

The PLGA composites containing the ferrofluid and Rhodamine B base dye were synthesized by oil-in-water emulsion solvent evaporation technique as discussed earlier with a slight modification. In the previous work the first step was the preparation of the nanoparticle-dye mixture. But it is know that the metal ions quench the dye through excited state charge transfer mechanism. The efficiency of the quenching depends on the distance between the donor and the acceptor species.[177] So, if the distance between the donor and acceptor species is increased the quenching process can be restricted.
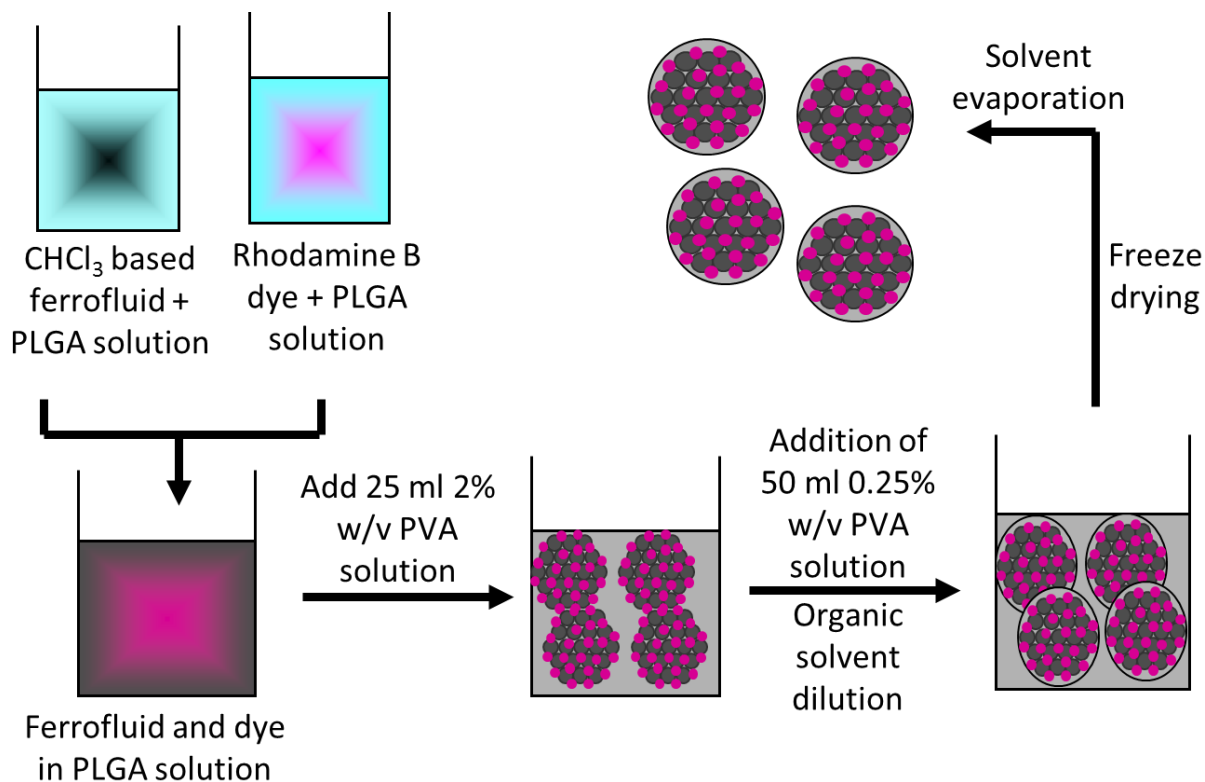
Figure 6-4: Schematic representation of modified oil-in-water (o/w) emulsion solvent evaporation technique utilized for the encapsulation of the ferrofluid and Rhodamine B base dye into PLGA polymer

Figure 6-4 represents the schematic representation of the synthetic scheme for preparing the PLGA composites. Firstly the polymer solution was formed by dissolving 200.00 mg of PLGA in 3 mL of dichloromethane (DCM). This polymer solution was divided into half. To the first half 1 mL of chloroform based ferrofluid was added while 20.00 mg of the Rhodamine B dye was added to the other half polymer solution. Both the ferrofluid and the dye containing solutions were sonicated for 5 minutes to achieve uniform mixing. The two polymer solutions were then mixed together to form the organic phase. This organic phase was then added to 50 mL of aqueous phase containing 2% w/v poly(vinyl alcohol) (PVA) as the stabilizer, to form the oil-in-water emulsion. PVA helps to reduce the surface tension of continuous phase (aqueous

phase), avoids the coalescence and agglomeration of the emulsion droplets formed and stabilizes the emulsion. The emulsion was homogenized with Ultra Turrax IKA T-18 basic homogenizer at 60,000 rpm for 1 minute. After that 50 mL of 0.25% w/v PVA solution was added to the oil-in-water emulsion and further homogenized at 40,000 rpm for another minute. This dilutes the organic solvent concentration in water and leads to the hardening of the composites. The solution was stirred for 4 hours to evaporate the organic solvent and then freeze dried. PLGA composites containing just the dye as well as the ferrofluid were also synthesized by the same procedure as controls. The prepared PLGA composites were stored in vial till further use.

6.4. Functionalization of the PLGA composites with Folic acid

For an effective drug delivery active targeting of the active agent to the tumor site is necessary. As discussed in chapter 1, Folic acid (FA) is a water soluble vitamin that can be used for tumor targeting via folate receptor mediated endocytosis. Folate receptor has been known to be greatly over expressed in several human tumors such as ovary, lung, breast, kidney, and brain. Folic acid has emerged as an attractive ligand for drug targeting due to its low molecular weight (MW-441), which allows for good tissue penetration. Also FA can be easily attached to the PLGA composites through carbodiimide chemistry. The PLGA composites can be functionalized with FA prior to the composite formation or can be conjugate to the pre formed PLGA composites. The FA conjugation prior to the composite formation is preferred as it is found to be robust as compared to the functionalization of the pre formed composite.

The functionalization of PLGA by FA was carried out in three steps. The first step was modification of the PLGA surface by controlled aminolysis to produce primary and secondary amine groups on the surface. The second step was activation of the FA by EDC and NHS. And the final step was the conjugation of the activated FA with aminolyzed PLGA.

6.4.1. Controlled aminolysis of PLGA
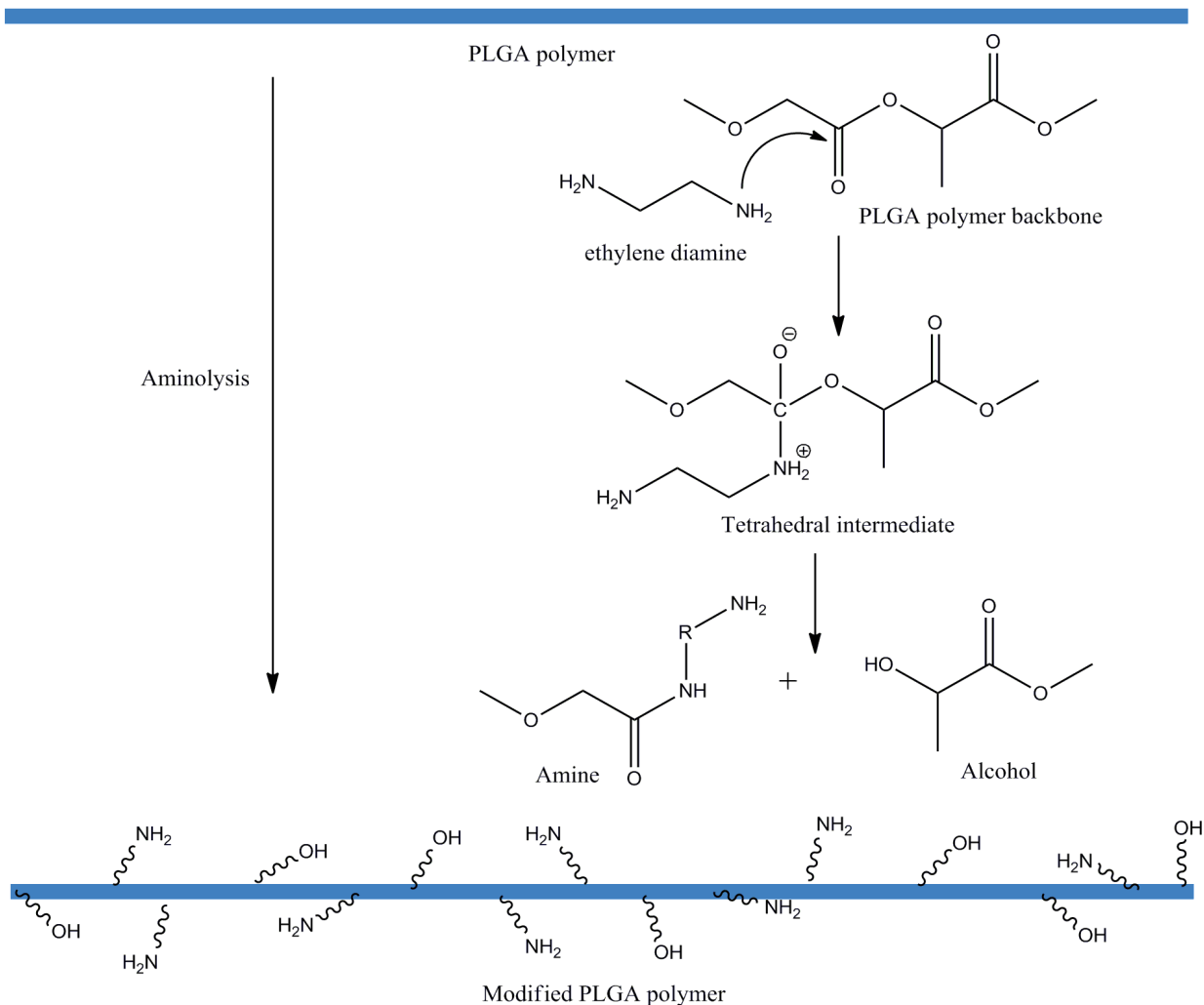
Figure 6-5: Controlled aminolysis of the PLGA polymer with ethylenediamine

Aminolysis is a technique that is used for surface modification of polyesters.[195-197] The reaction proceeds via nucleophilic attack on the carbonyl carbon to form a positively charged tetrahedral intermediate. Under basic conditions, the tetrahedral intermediate is deprotonated and the reaction proceeds to the formation of an amide and an alcohol as shown in Figure 6-5. 200.00 mg of premade PLGA were immersed in aqueous solution of 5 mL of 0.05 M ethylenediamine (ED) for 15 minutes. The aminolyzed PLGA was then washed three times with

ice cold water to remove any excess of ethylenediamine. IR spectroscopy was performed on the aminolyzed PLGA to confirm the presence of the amino groups.

6.4.2. Activation of Folic acid (FA)

The chemical conjugation of aminolyzed PLGA with folic acid (FA) was carried out utilizing the carbodiimide chemistry. Carbodiimide is a functional group containing the general formula RN=C=NR. In synthetic chemistry carbodiimides are used to form amide linkage between carboxylic acids and amines. Dicyclohexylcarbodiimide (DCC) is a zero length crosslinking agent used to couple carboxyl groups to primary amines. DCC reacts with a carboxyl group forming an amine-reactive O-acylisourea intermediate. This intermediate may react with an amine, yielding an amide. However, the failure to react quickly with an amine results in hydrolysis and regeneration of the carboxyl moiety. The addition of N-hydroxysuccinimide (NHS) stabilizes the amine-reactive intermediate by converting it to an amine-reactive NHS ester, thus increasing the efficiency of DCC-mediated coupling reactions. The amine-reactive NHS ester intermediate has sufficient stability to permit two-step crosslinking procedures.

The carboxylic group of folic acid was activated by DCC and NHS as shown in the synthetic scheming in Figure 6-6. Briefly, 1.00 g of FA was dissolved in 20 mL of dimethylsulfoxide (DMSO) in a 100 mL one neck round bottom flask under magnetic stirring. Then 1.10 g of NHS and 1.10 g of DCC were added to the FA solution (folic acid/NHS/DCC molar ratio=1:1.1:1.1). The reaction mixture was allowed to react at room temperature for 12 hours in dark. At the end of 12 hours of reaction, white byproduct N,N'-dicyclohexylurea precipitates are found. The reaction mixture is filtered through glass wool plug and precipitated with ethyl ether. The precipitated FA-NHS ester was pelleted by centrifugation and the

supernatant was removed. The precipitated FA-NHS ester was vacuum-dried and stored in an amber vial till further use.
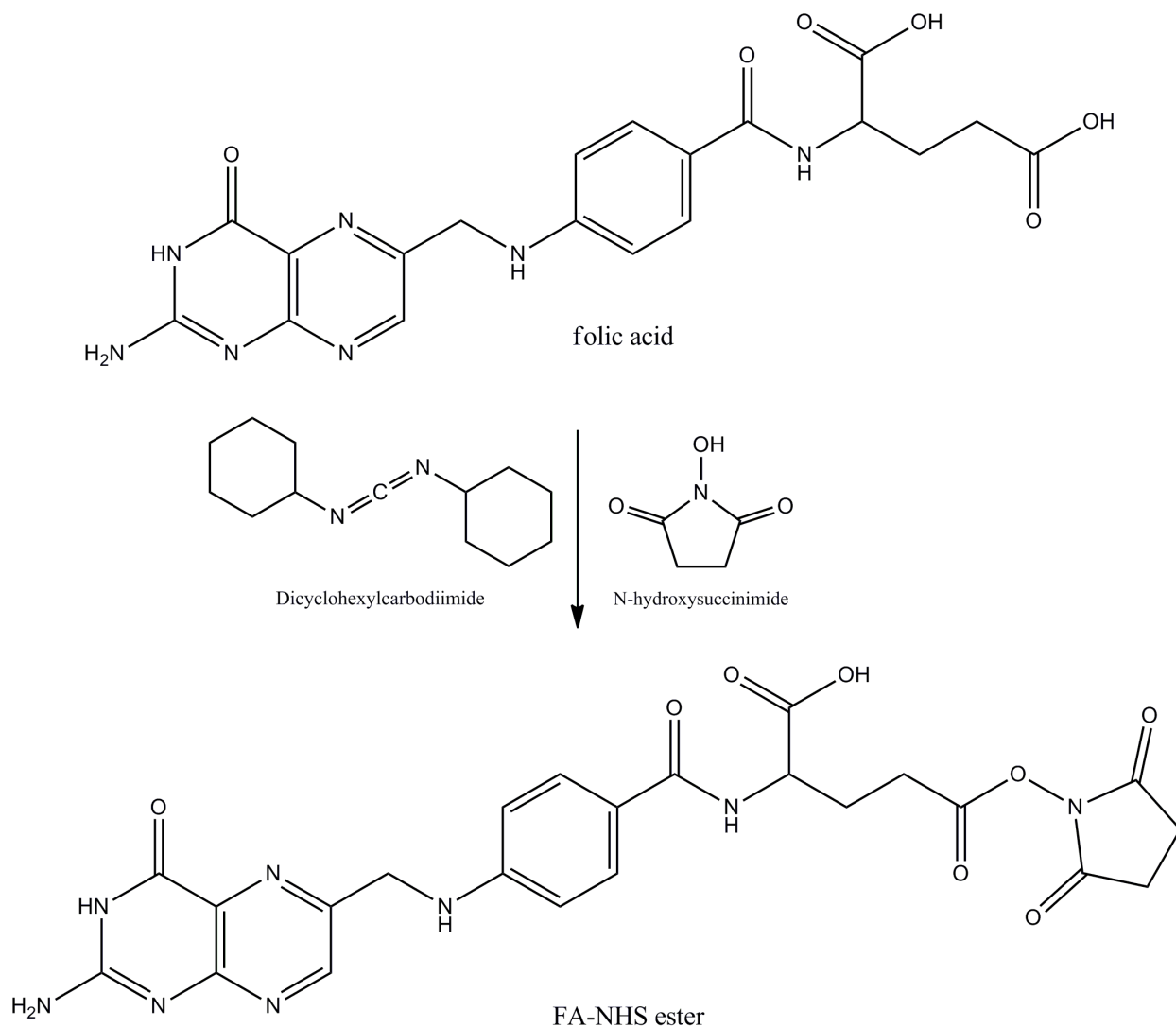
Figure 6-6: Activation of the carboxyl group of FA with DCC and NHS to form the FA-NHS ester

6.4.3. Conjugation of FA-NHS ester with aminolyzed PLGA

200.00 mg of aminolyzed PLGA was dissolved in 10 mL DCM in a 25 mL round bottom flask under magnetic stirring. Then 200.00 mg of FA-NHS ester was added to it and was let to react for 4 hours. After the end of 4 hours the FA functionalized PLGA (FA-PLGA) was precipitated with ethyl ether. The precipitated FA-PLGA was pelleted by centrifugation and the

supernatant removed. The pellet was re-dissolved in DCM (<1 mL), precipitated, and centrifuged once more to remove any unreacted FA-NHS ester.

This FA -PLGA polymer was used to synthesis the composites utilizing the ferrofluid and Rhodamine B dye by modified oil-in-water emulsion solvent evaporation technique as discussed in section 6.3.

6.5. Results and Discussion

The ferrofluid and PLGA composites were characterized by x-ray diffraction, electron microscopy, vibrating sample magnetometry, and fluorescence spectroscopy to determine the phase, size and morphology, saturation magnetization and the loading percentages of the dye and nanoparticles. The chloroform based ferrofluid was evaporated in a watch glass to obtain dried nanoparticles powder. These dried nanoparticles were used for the powder XRD and VSM measurements.

Powder x-ray diffraction (XRD) measurements were performed using a Panalytical X'pert pro diffractometer at a scanning step of 0.05º with a 2θ range from 20º to 80º using a graphite monochromated Cu-Kα radiation source. Sample was ground and pressed onto a no background, low volume silicon holder. Figure 6-7 shows the powder XRD pattern of the as synthesized ferrofluid nanoparticles with an overlay of the data obtained from the JSPDS reference powder diffraction pattern of magnetite.[198] The pattern shows a pure phase magnetite (Fe_3O_4). Major diffraction peaks for magnetite at 30.125°, 35.483°, 37.117°, 43.124°, 53.501°, 57.033°, 62.949°, 71.430°, 74.493°, 75.504°, and 79.504° correspond to the (220), (311), (222), (400), (422), (511), (440), (620), (533), (622), and (444) miller indices, respectively. The peaks were indexed by the JCPDS database for magnetite (fd3m, card#01-086-1343).
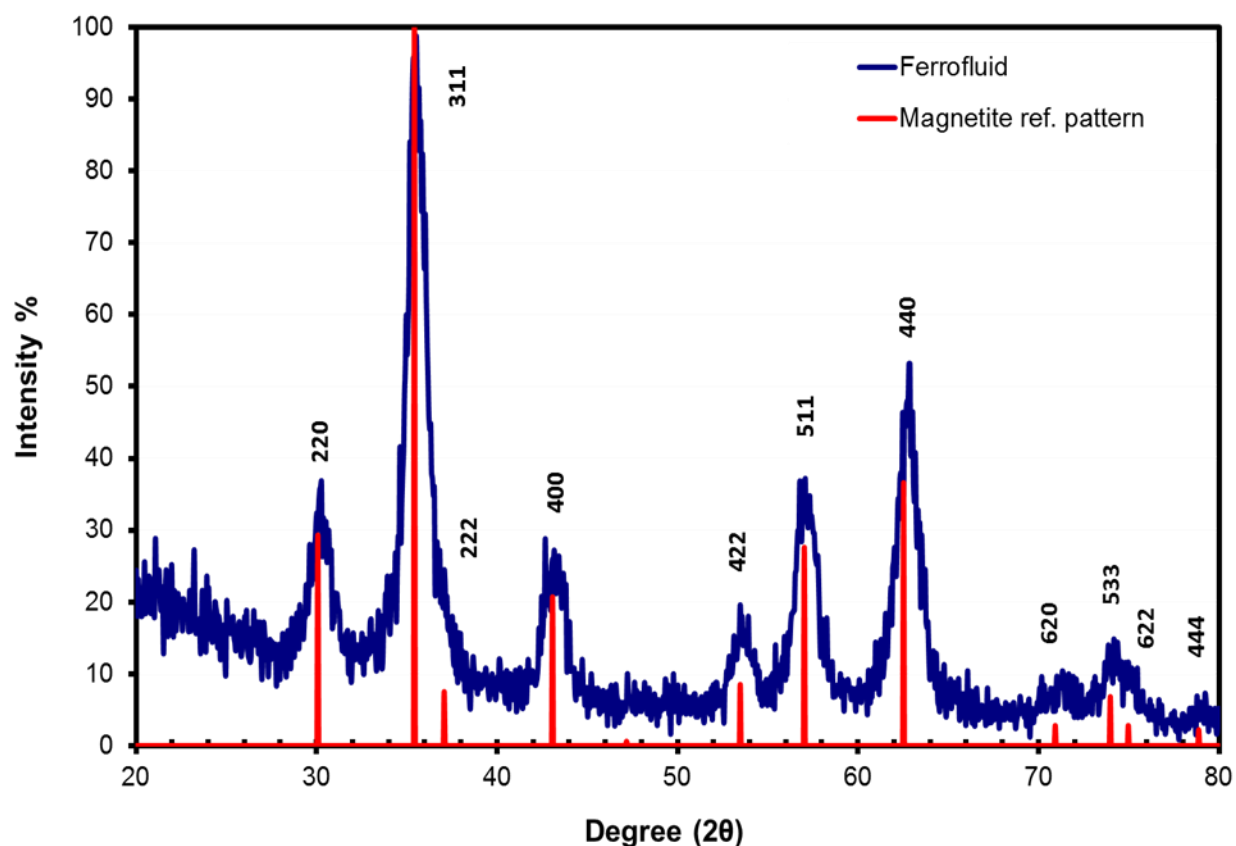
Figure 6-7: Powder x-ray diffraction pattern of as synthesized ferrofluid

The size and morphology of the synthesized ferrofluid was confirmed by transmission electron microscopy (TEM). Figure 6-8 shows relatively uniformed size spherical nanoparticles with average diameter of 10 ± 5 nm. The spherical nanoparticles seem to be agglomerated and not mono-dispersed in the TEM image. The agglomeration can rise from the TEM sample preparation. For the TEM grid preparation the dried magnetite nanoparticles were dispersed in methanol and then around 5 µL of the dispersed solution was placed on the copper grid. We believe that the agglomeration of the particles is induced by drying of the ferrofluid
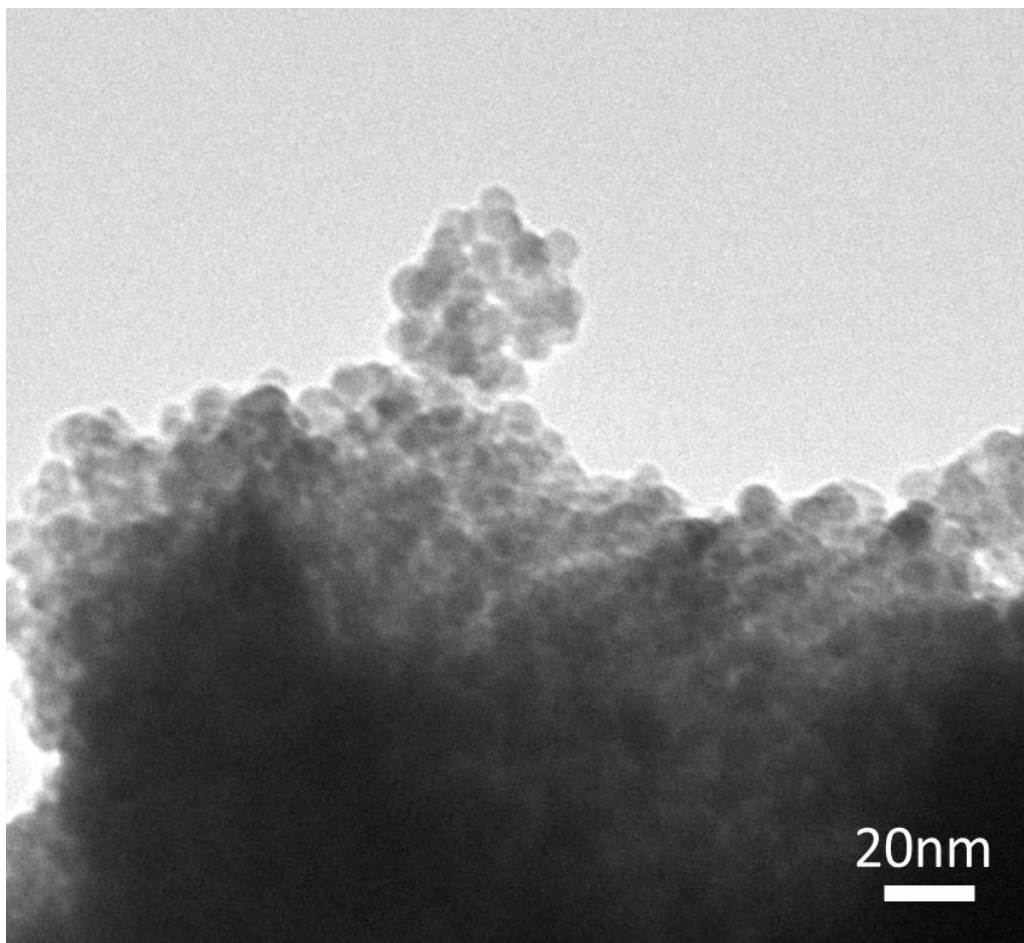
Figure 6-8: TEM image of the magnetite nanoparticles in the ferrofluid.

The FA functionalization of the PLGA composites was confirmed by both FTIR and UV-Vis. spectroscopy. The appearance of the amide linkage in the FTIR confirms the covalent attachment of the FA to PLGA. The presence of the characteristic bands of FA in the FA conjugated PLGA also confirms the covalent attachment of FA.

Figure 6-9 shows the IR spectra of PLGA, aminolyzed PLGA, FA functionalized PLGA and FA by itself. From the spectrum of PLGA, it can be observed that there is a strong characteristic band at 1740 cm^{-1} corresponding to the stretching vibrations of the carbonyl group (C=O), the bands at 2940 and 2990 cm^{-1} are assigned to the C–H stretching vibrations of the –CH$_2$ groups in the backbone chains of PLGA. Similarly, the bands at 1160 and 1070 cm^{-1} are

attributed to C–O stretching of the ester group. When aminolyzed PLGA was analyzed by IR, similar peaks to those of PLGA were observed with additional bands appearing at 1640 and 1570 cm^{-1} due to N-H bending vibrations of amine group (NH_2). The presence of this band confirms the presence of amine groups on the PLGA. The folic acid functionalized PLGA (FA_PLGA) shows characteristic bands of PLGA as well as folic acid. The band at 3550 and 3300 cm^{-1} corresponding to O-H and N-H stretching vibrations of amide group, 1610 cm^{-1} corresponds to the C=O stretching vibrations of amide group and 1380 cm^{-1} corresponding to C-N stretch for amide group. The appearance of the characteristic bands of amide group confirms the covalent attachment of folic acid with PLGA While the IR spectrum of folic acid is characterized by bands between 3600 and 3000 cm^{-1} are due to the OH stretching and N-H stretching vibration bands, band at 1670 cm^{-1} for C=O stretching vibrations from carboxyl group (COOH) and 1600 cm^{-1} for N-H bending vibrations of amine group (NH_2).[177]
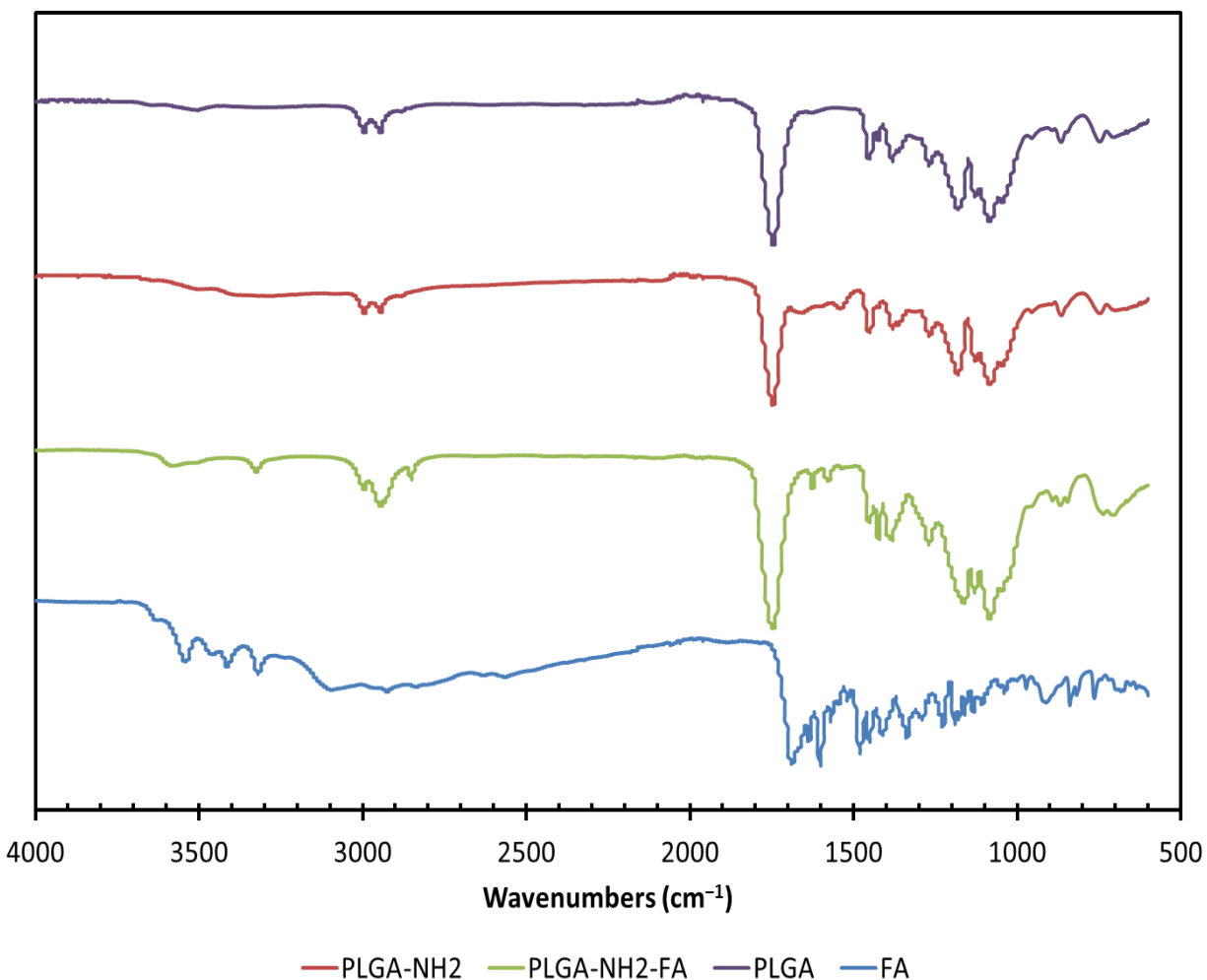
Figure 6-9: IR spectra of PLGA, aminolyzed PLGA (PLGA-NH$_2$), FA functionalized PLGA and FA

Further the FA functionalization of PLGA was confirmed by UV-vis spectroscopy. Figure 6-10 shows the absorbance spectra of the FA functionalized PLGA polymer (FA-PLGA) and folic acid by itself. The FA absorbs UV light and has absorption peaks at 210, 280 and 360 nm.[199,200] The absorbance spectra of the FA functionalized PLGA also shows absorbance maxima at 280 and 360 nm confirming the covalent attachment of the folate. The FA and FA-PLGA samples for absorbance measurements were prepared by dispersing about 1 mg each in water. The absorbance of the aqueous suspension was measured in a quartz cuvette.
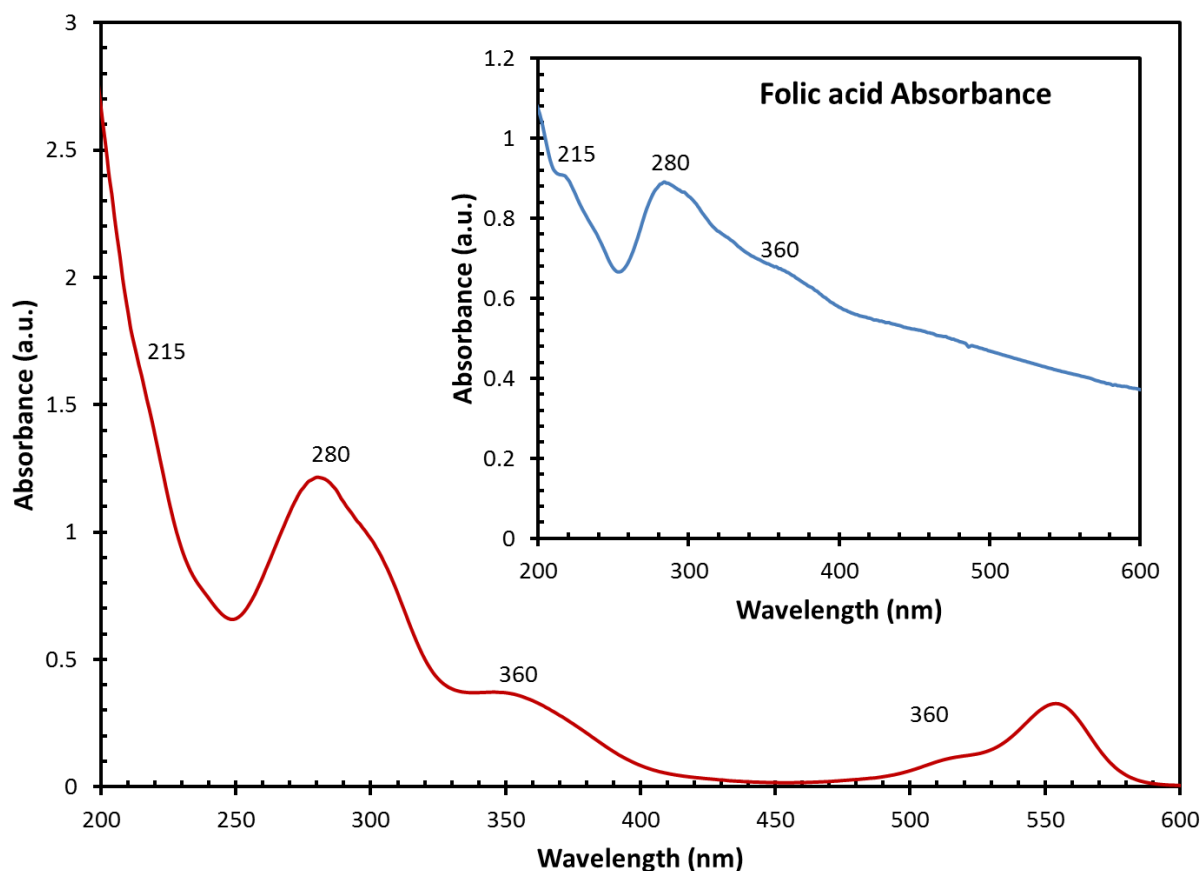
Figure 6-10: UV-Vis absorbance spectra of the FA functionalized PLGA polymer. Inset shows the absorbance spectra of pure folic acid (FA)

Scanning electron microscopy was performed on Hitachi SU-70 field emission scanning electron microscope to evaluate the size distribution and morphology of the magnetic PLGA composites and the FA-PLGA composites containing the dye and the ferrofluid. Both PLGA and FA-PLGA composites samples were prepared by lightly sprinkling the composite powder on a conductive carbon tape mounted on the sample holder. The sample was then sputtered with gold to make it conductive and reduce charging. As seen in Figure 6-11 the PLGA composites are relatively uniform sized with an average diameter of 300±50 nm while the FA-PLGA composites are found to be spherical with a wider size distribution. The FA-PLGA composite

looks as if they are interconnected and we speculate that it occurs due to excessive charging of the FA-PLGA composites even after sputtering it with conductive gold.
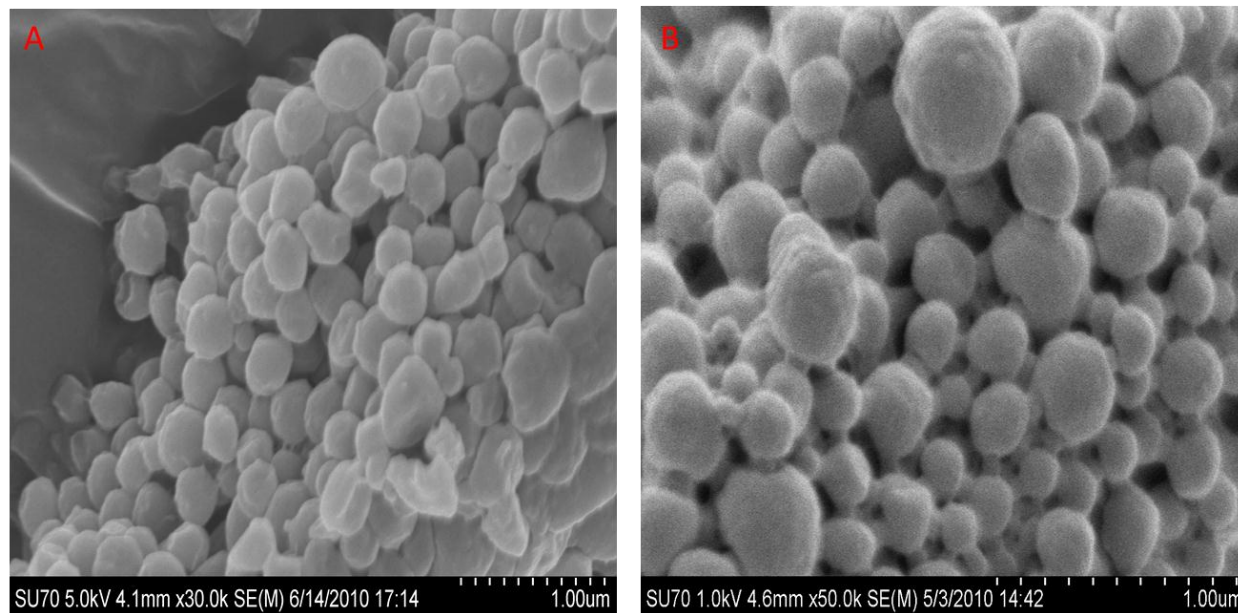
Figure 6-11: SEM image of the PLGA composites utilizing the ferrofluid and Rhodamine B dye. (A) PLGA composites, (B) FA-PLGA composites

The loading efficiency of the prepared PLGA composites was determined by fluorescence spectroscopy. Rhodamine is acetone soluble so 4.00 mg of the PLGA composite were dissolved in 10 mL of acetone and filtered to remove the iron oxide nanoparticles. Fluorescence measurements were performed on the filtrate to determine the dye content in 4 mg of the composites. Fluorescence intensity of known concentrations of dye was measured and a linear curve fit was performed which yields around 1.97% w/w dye loading in the PLGA composites containing both dye and ferrofluid.
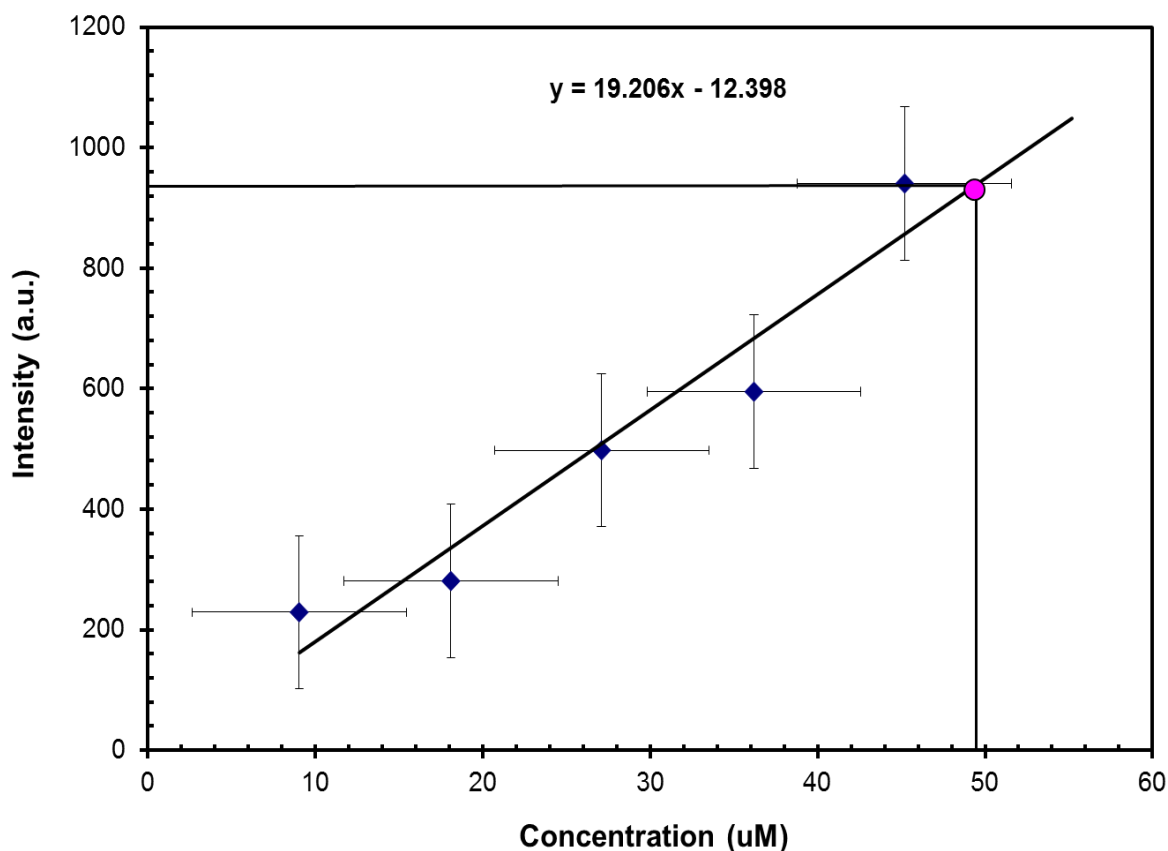
Figure 6-12: Linear regression plot yielding a 1.97 % w/w Rhodamine B dye loading into the PLGA composites

Thermogravimetric analysis (TGA) was performed on the PLGA composites containing the dye and ferrofluid (magnetic PLGA comp.), as well as the controls- PLGA dye composite, PLGA ferrofluid composite and PLGA by itself. As can be seen in Figure 6-13 TGA plot yields around 2 % w/w Rhodamine B dye and 6.67 % w/w magnetite nanoparticle loading. The decomposition event around 240º C attributed to the decomposition of PLGA as seen in figure. The decomposition event around 240º C is observed in the magnetic PLGA composites decomposition profile. The Rhodamine B dye yields two decomposition events around 315 º C and 430 º C. A trivial decomposition event is observed at 315º C and 430º C attributed to the decomposition of Rhodamine B dye in the magnetic PLGA composites decomposition profile.

The ferrofluid shows a decomposition event around 200º C due to the decomposition of the sodium oleate surfactant on the surface of the particles. The magnetite nanoparticles thereafter are stable and show no degradation till 600º C.
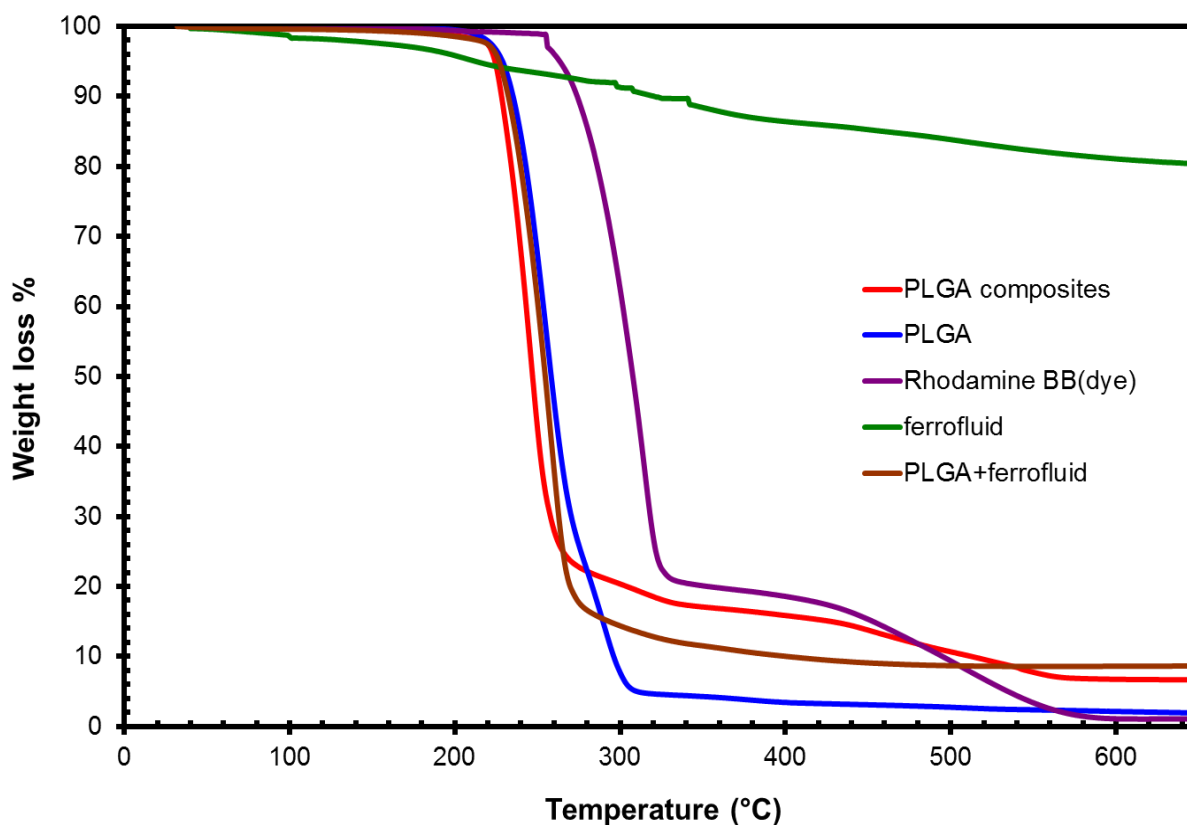
Figure 6-13: TGA plot showing the decomposition profile of the PLGA composites and the controls

Magnetic characterization was performed on the chloroform based ferrofluid as well as the PLGA composites by room temperature vibrating sample magnetometer (VSM) after drying the fluid. Figure 6-14 shows a hysteresis plot of the as synthesized ferrofluid and PLGA composites. The saturation magnetization of the iron oxide nanoparticles was around 105 emu/g. As seen in the inset the corecivity of magnetite nanoparticles is found to be negligible. The saturation magnetization of the bulk magnetite is found to be around 90-120 emu/g. The

decrease in the magnetization of the magnetite nanoparticles is attributed to the surfactant coating on the surface of the particles. The inset shows the hysteresis plot of the PLGA composites containing the dye and the ferrofluid yields net magnetization around 8.18 emu/g. Utilizing the TGA data for weight correction the net magnetization of PLGA composites was found to be 100.00 emu/g. The hysterysis loop for the PLGA composites is observed to be very noisy because the volume of magnetite nanoparticles is very less within the PLGA composites as well as the particles is randomly spread within the composites.
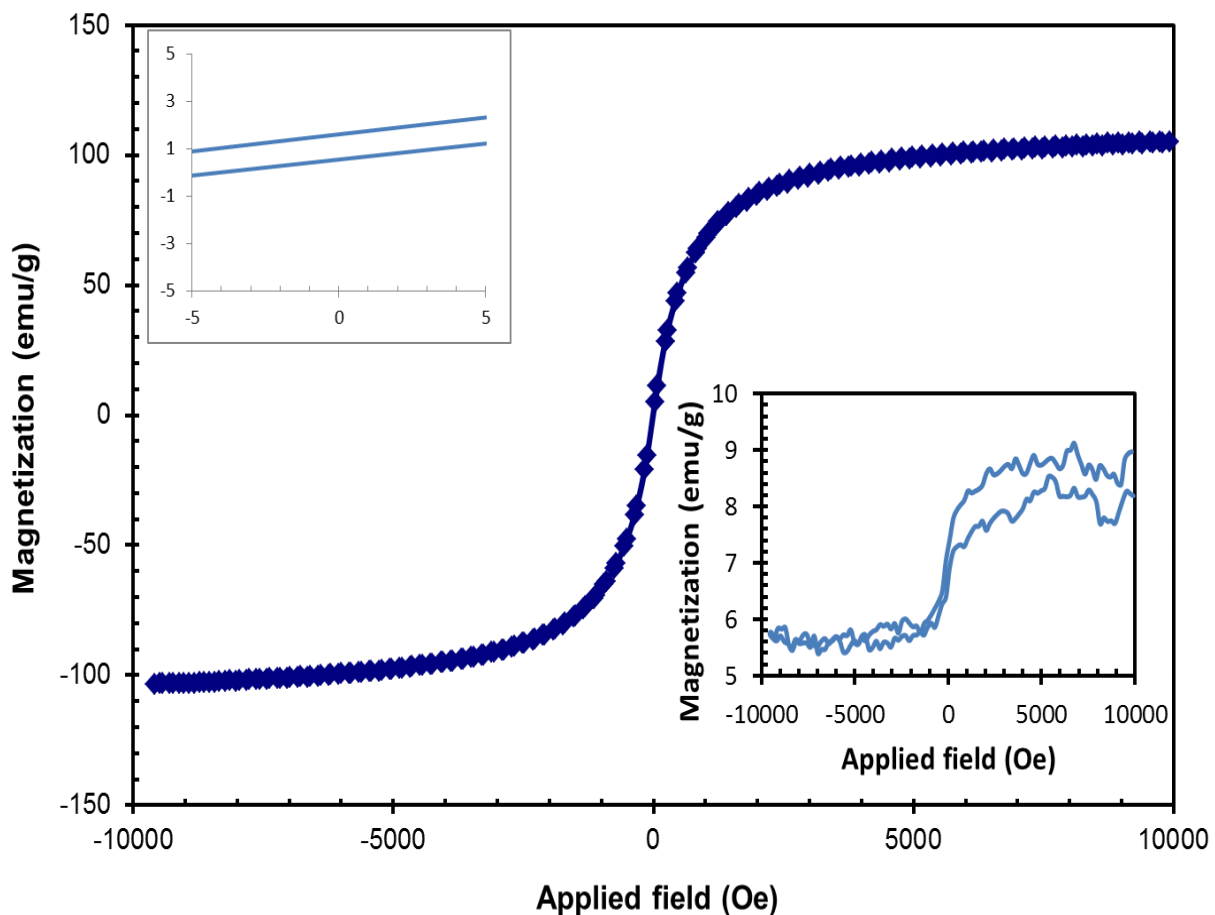
Figure 6-14: Room temperature VSM data of the as-prepared ferrofluid material plotted as magnetization (emu/g) versus applied field (Oe)

Fluorescence spectroscopy was employed to study the release kinetics of the Rhodamine B dye from the PLGA composite while placing the sample in a radio frequency (Rf) induction heating coil. Fluorescence measurements were performed on an open bench top HORIBA Jobin Yvon spectrometer equipped with a 535 nm laser source and synapse CCD detector shown in the Figure 6-15.
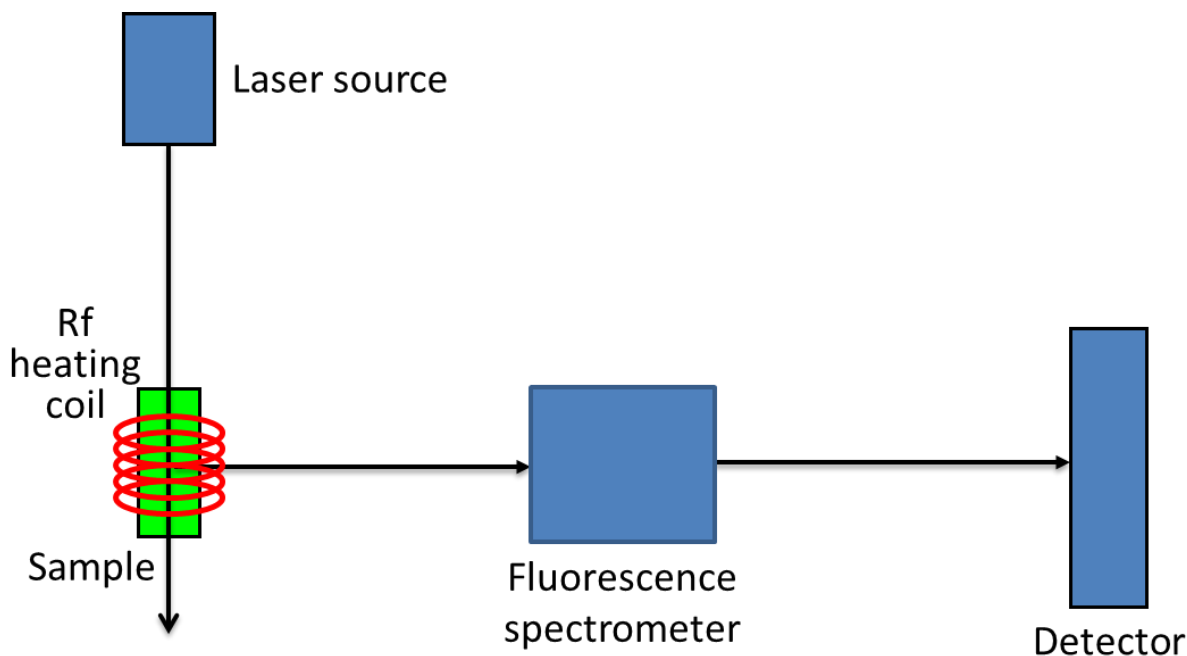
Figure 6-15: Block diagram of the open bench top fluorescence spectrometer equipped with laser and the Rf heating coil set

6.5.1.Rf induction heating

Rf induction heating was carried out using Ambrell Inc. Model Easyheat 0224 induction heating system. In a basic induction heating setup shown in Figure 6-16, a solid state Rf power supply sends an AC current through an inductor coil (often a copper coil). The passage of current through this coil generates a very intense and rapidly changing magnetic field in the

space within the inductor coil and the sample to be heated is placed inside the coil. The intense alternating magnetic field inside the inductor coil repeatedly magnetizes and de-magnetizes the iron oxide nanoparticles. This rapid flipping of the magnetic domains causes considerable friction and heating inside the material. The magnetic hyperthermia induced by Rf radiations is termed as Rf hyperthermia.
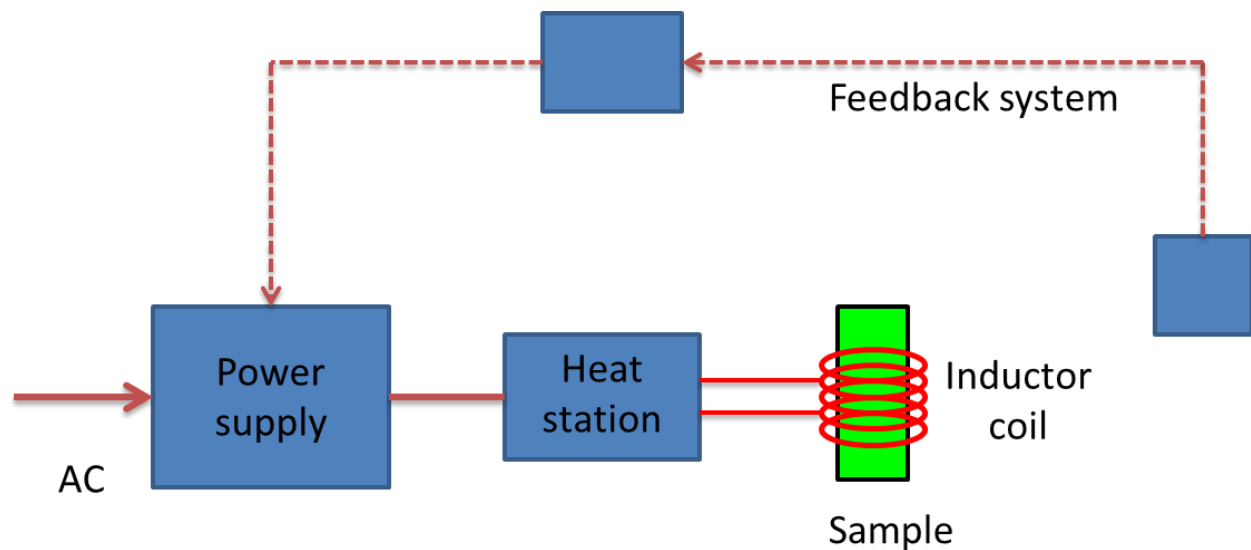
Figure 6-16: Block diagram of the basic induction heating coil system

The Rf hyperthermia technique offers benefits over existing hyperthermia treatments such as the technique can be localized using suitable Rf coils.[201,202] Also Rf can be used for heating deep-seated tumors compared to microwave hyperthermia that has a poor depth of penetration, which makes it unsuitable for treatment of deep-seated tumors. The microwave radiations also heats up the surrounding water molecules by dielectric heating producing excessive heat.[186] Another major benefit of Rf hyperthermia is that it can be integrated into magnetic resonance imaging (MRI) systems for simultaneous treatment and monitoring.[202]
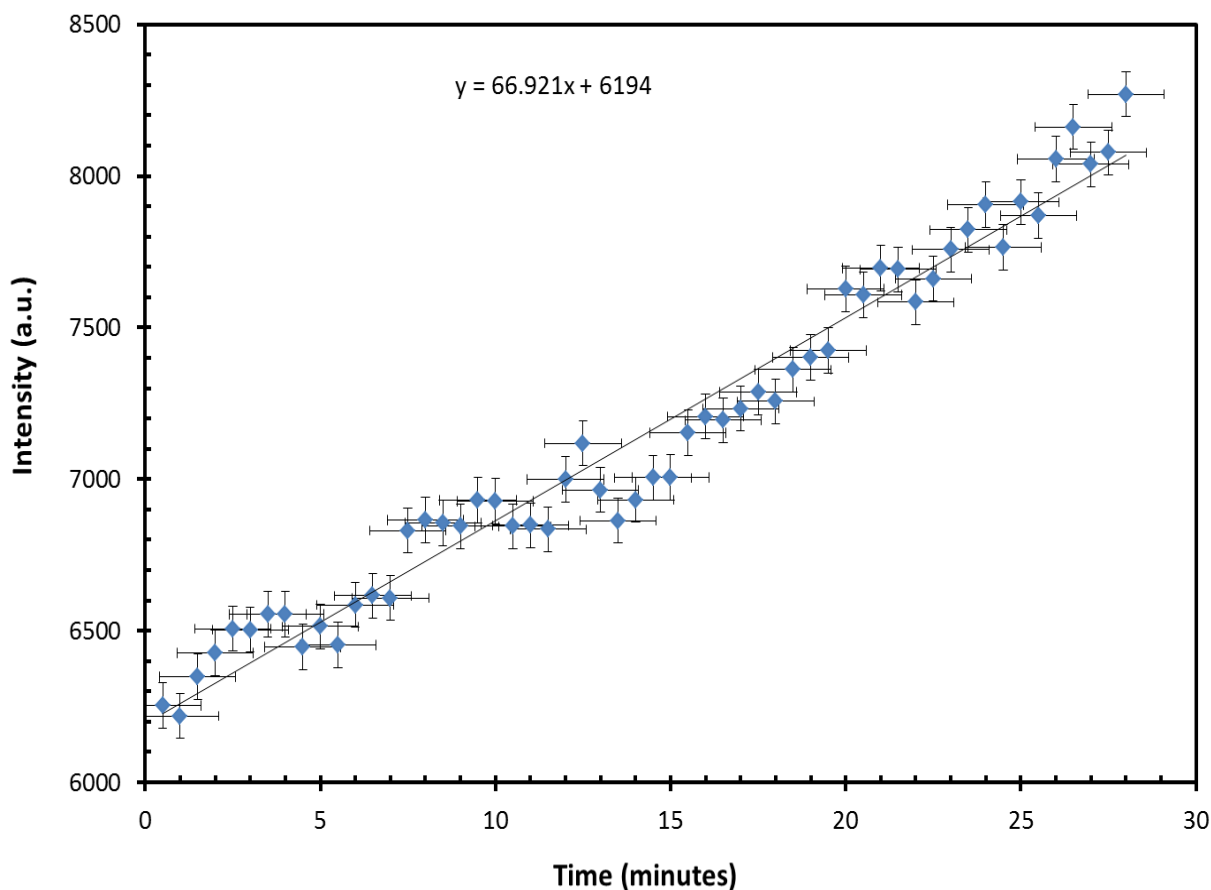
Figure 6-17: Plot of fluorescence intensity with the time of Rf induction heating of the PLGA composites. An increase in the fluorescence intensity is observed with time.

The PLGA composites were dispersed in water and sonicated for about 15 minutes to remove the aggregated particles and then magnetically extracted and re-dispersed in water. In-situ fluorescence measurements were carried out on the dispersed PLGA composites at every 30 seconds time interval for 30 minutes while the sample was placed in the Rf induction coil. Figure 6-17 shows that the fluorescence intensity of the PLGA composites increases linearly with time of Rf induction heating.
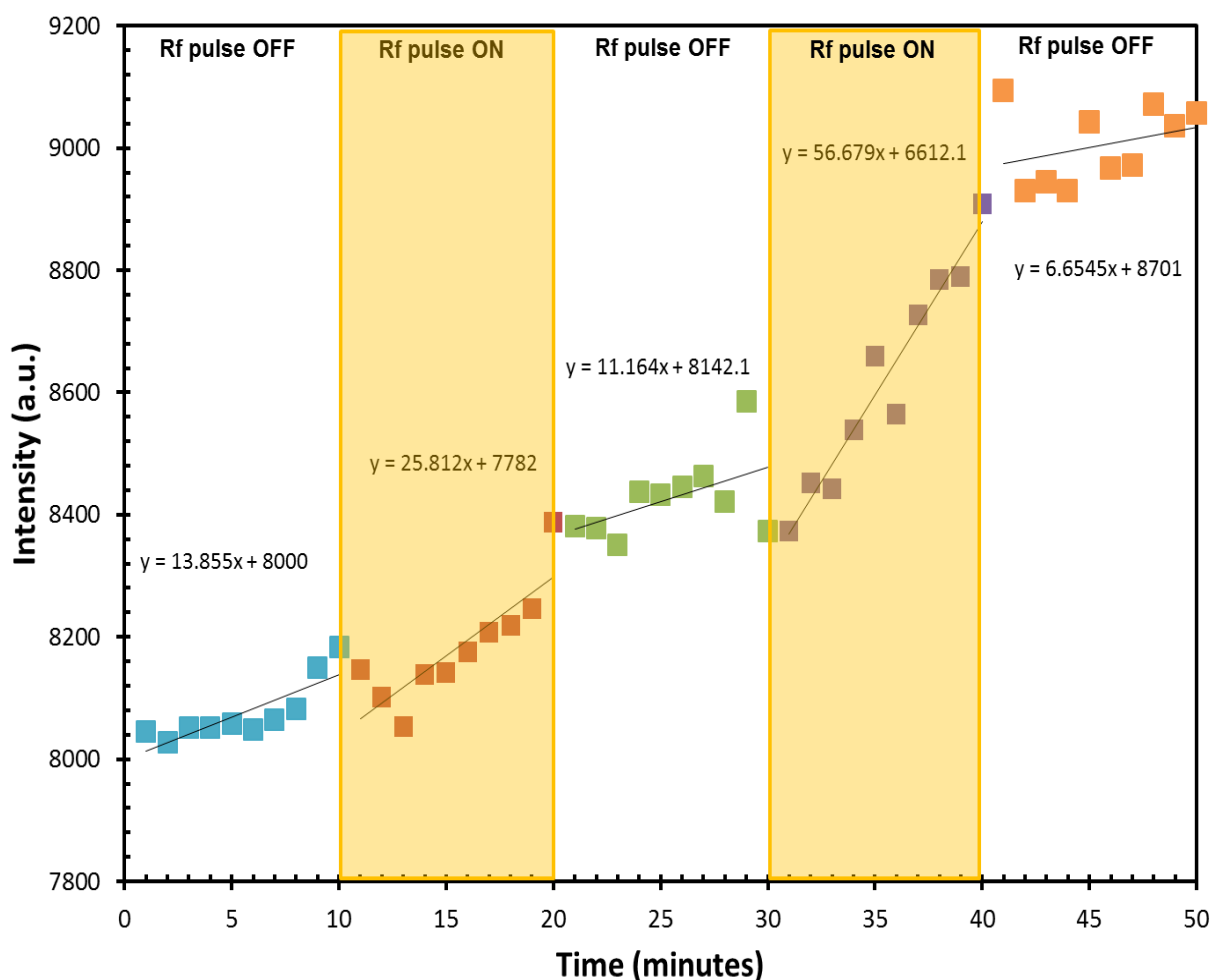
Figure 6-18: Plot of fluorescence intensity with the time of pulsed Rf induction heating of the PLGA composites. An increase in the fluorescence intensity is observed when the Rf pulse is switched ON and the intensity decreased when the Rf pulse is switched OFF

A pulsed Rf treatment of the PLGA composites was also carried out which showed a corresponding increase in the rate of the dye release when the PLGA composites were heated (Rf pulse ON) and the rate of dye release decreases when RF pulse was OFF. As seen in Figure 6-18 the fluorescent intensity increases slightly in the first 10 minutes when the RF pulse is OFF, due to the burst release of the dye at the surface of the composites. For the next 10 minutes i.e. between 10 to 20 minutes when the Rf pulse is ON an increase in fluorescent intensity is observed. An insignificant increase in intensity is observed from 20 to 30 minutes when the Rf

pulse OFF and that is due to the remnant heat left when the Rf pulse was ON. With the next Rf pulse ON between 30 to 40 minutes, a significant increase in the intensity is observed and again the intensity decreases when the Rf pulse is switched OFF between 40-50 minutes.
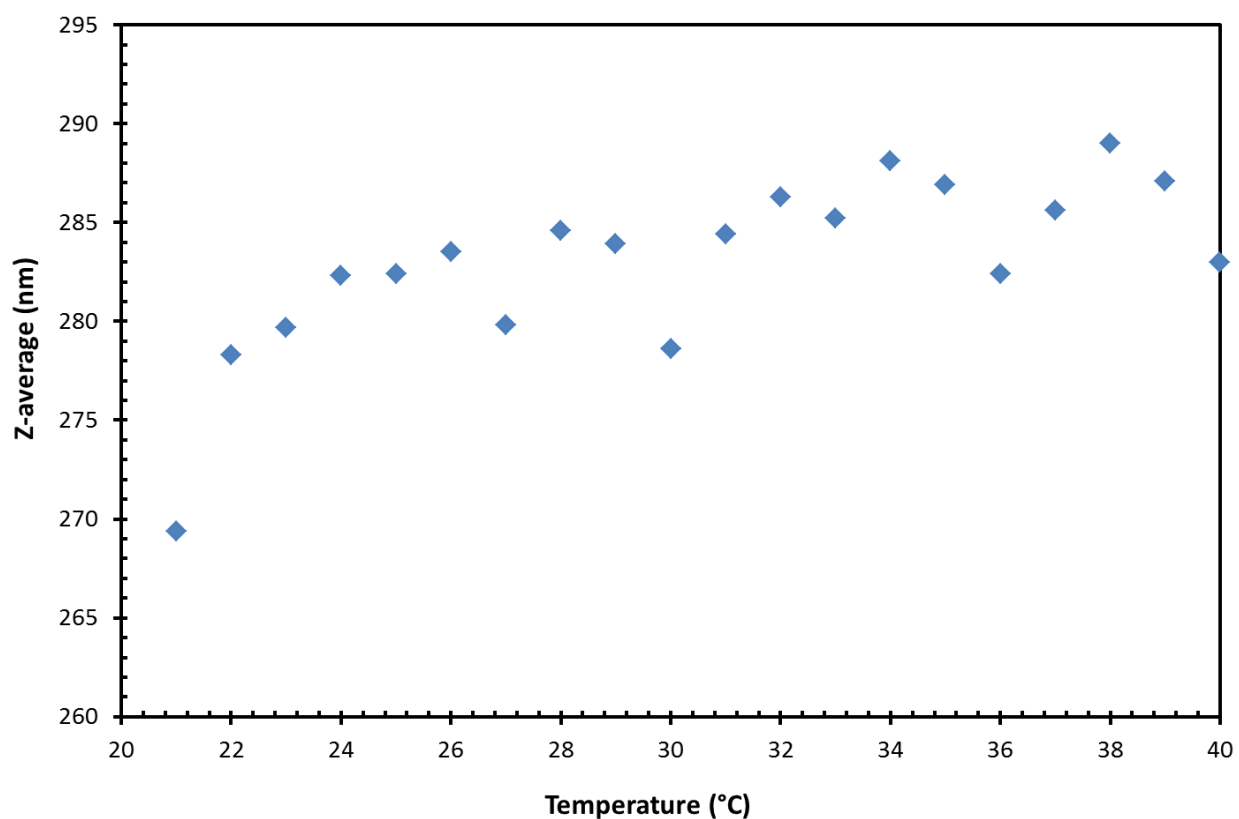
Figure 6-19: Plot of DLS results showing the increase in size with the increase in temperature

We speculate that when the magnetite nanoparticles are inductively heated that heat up the surrounding polymeric composite leading it to swell. The swollen polymeric composites in turn lead to the release of Rhodamine B dye. The swelling up of the PLGA composites due to the heat is confirmed by dynamic light scattering measurements. Figure 6-19 shows the plot of temperature vs. the average particle size of the PLGA composites containing the dye and

ferrofluid as well as the PLGA composites by itself. An increase in the size of the composites is observed with increase in the temperature. Similar results were obtained for PLGA controls.

6.6. MRI contrast application

This ferrofluid was also investigated in vitro by magnetic resonance relaxivity measurements for its application in magnetic resonance imaging. The magnetic resonance imaging (MRI)/spectroscopic experiments were performed on a 2.4 T/40 cm bore MR system (Biospec/Bruker). For magnetic resonance relaxivity measurements the PLGA composites were dispersed in low melting agarose gels to avoid settling of the composites.

6.6.1. MRI sample preparation

The 1% agarose (w/v) gels were prepared by dissolving agarose powder in deionized water. The solution was heated in a microwave oven while stirring occasionally to ensure complete dissolution of agarose. The MRI relaxation times were measured for gels containing PLGA composites with concentrations of 0.6700, 0.3350, 0.1675, 0.0838, and 0.0419 mM.   A control sample without PLGA composites was measured.

The MRI/spectroscopic experiments were performed by a collaborator and the experimental details followed were as follows. Spectroscopic T_1 and T_2 ^{1}H relaxation measurements of the PLGA composites dispersed in agarose gel were conducted using an inversion recovery sequence with eight inversion times (TI) and repetition times (TR) at least five times the expected T_1 value. For the T_2 measurements, a multi-spin-echo CPMG sequence was employed with several echo times (TE) and TR values at least five times the expected T_1. The relaxation times were computed from least-squares fitting of the exponentially varying signals using analysis routines available at the MR system. Relaxivities were extracted from

graphs of relaxation rates ($1/T_1$ and $1/T_2$) versus concentration. The concentration range used for the relaxivity measurements was in the range 0.0419-0.6700 mM.

6.6.2. MRI results

Measured at 2.4 T and 20^0 C

R_2
y = 58.713x + 10.87
R^2 = 0.9976

R_1
y = 0.1303x + 0.3645
R^2 = 0.9954
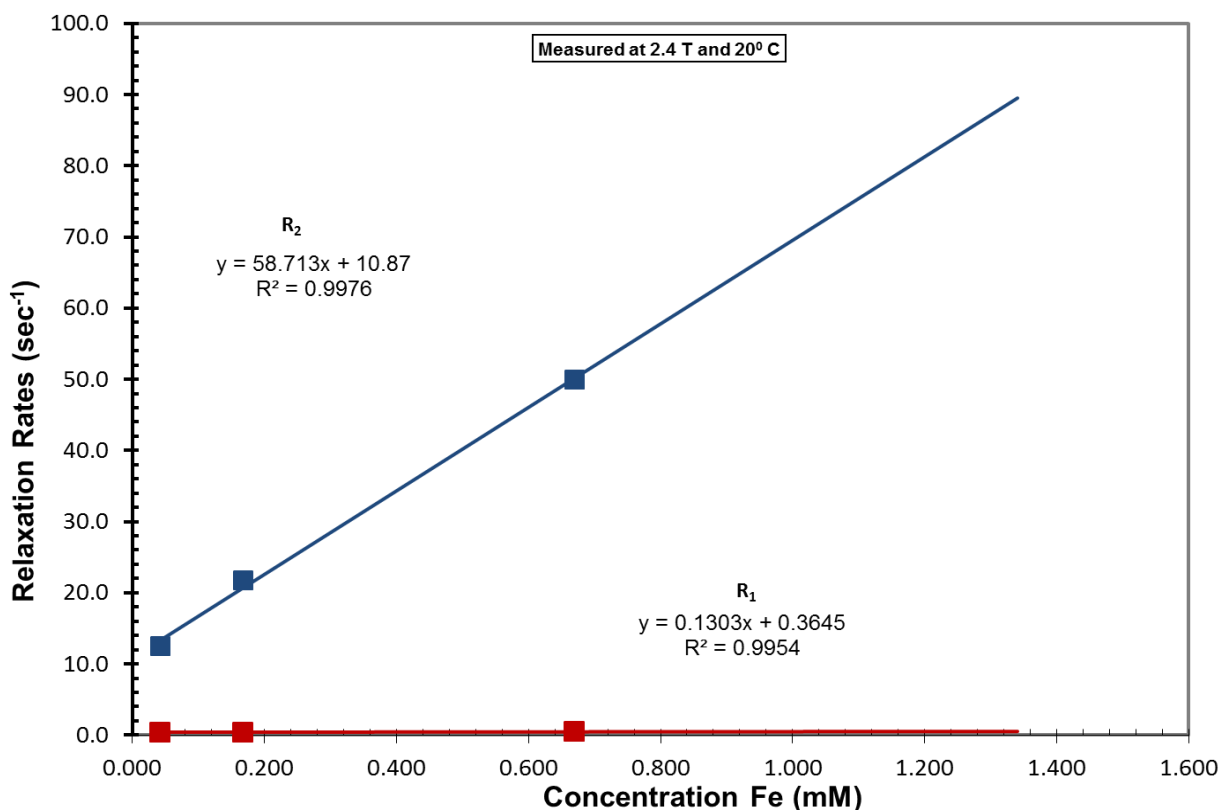
Figure 6-20: Relaxivity plot for first MRI measurements

In Figure 6-20, the relaxation rates $R_1=1/T_1$ and $R_2=1/T_2$ are shown as a function of concentration of the PLGA composites. The relaxivities R_1 and R_2, representing the slopes of these curves, are 0.1 $s^{-1}mM^{-1}$ and 58.7 $s^{-1}mM^{-1}$ respectively. Iron oxide nanoparticles are known to be T_2 enhancement agent as they have high magnetic susceptibilities and generate high magnetic field gradients near their surfaces. These gradients create local magnetic field inhomogeneities that cause rapid dephasing of nearby proton spins, thus increasing proton

transverse relaxivities (R_2) which is evident from the relaxivity plot. A negligible reduction in the transverse relaxivity (R2) is observed due to the polymeric coating on the nanoparticles.
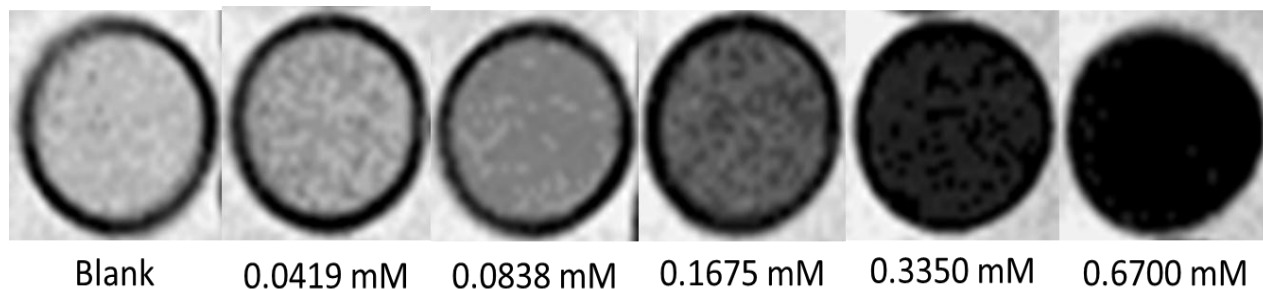
Figure 6-21: MRI T$_2$-weighted image of the PLGA composites sample in agarose with varying concentration of the magnetite (iron oxide) nanoparticles.

As discussed earlier the iron oxide (magnetite) nanoparticles are effective in reducing the T_2 relaxation time, thereby inducing a signal darkening on the T_2-weighted MRI images. As seen in Figure 6-21 as the concentration of the iron oxide nanoparticles increases the image contrast the respective micro-centrifuge tubes increases. This phenomenon is caused by the significant enhancement of transverse proton relaxation in the vicinity of areas containing magnetic iron oxide, thus leading to quick fading of MR signals.

6.7. Conclusion

In conclusion, the chloroform based ferrofluid containing monodisperse magnetite nanoparticles were produced using thermolysis technique. The magnetite nanoparticles of the ferrofluid were mono-dispersed with an average diameter of 10 ± 5 nm and were highly magnetic with a saturation magnetization of 105 emu/g. The ferrofluid was found to be stable over six months. The PLGA composites were synthesized using the ferrofluid and Rhodamine B dye by modified oil-in-water emulsion evaporation technique. The PLGA composites were further

functionalized with folic acid to achieve targeted delivery.   The release of the dye from the PLGA composite when place in a Rf induction coil was determined by fluorescence spectroscopy and an increase in the fluorescent intensity was observed with increase in the Rf induction heating time.   A pulsed Rf treatment of the PLGA composites was also carried out which shows a corresponding increase in the rate of dye release when the composites are heated (RF pulse ON) and rate decrease (RF pulse OFF). The dye is released from the PLGA composites due to the swelling of the polymer and this is confirmed by dynamic light scattering measurements.   Magnetic resonance imaging was also performed using the PLGA composites which showed enhancement in the T_2-weighted image contrast and thus negligible reduction in the contrast capabilities of the iron oxide particles (R_2 = 58.7 s^{-1}mM^{-1}).   The PLGA composites containing the dye and the iron oxide nanoparticles thus show a potential for being a dual modal imaging and therapeutic delivery system with reduced drug related toxicity and better drug activity.

Chapter 7. Conclusions

The goal of this dissertation was to design a dual modal controlled release drug delivery system with cellular targeting capabilities. As discussed in this dissertation the design of the drug delivery carrier consisted of magnetic nanoparticles as a core with a biocompatible polymer coating. The incorporating of magnetic iron/iron oxide nanoparticles into the polymeric composites was to achieve local heating of the composites through magnetic hyperthermia principles. These polymeric composites are expected to be superior to conventional routes of drug administration because the use of nanocomposites would improve the lifetime of the drug in the circulation, increase the accumulation of the drug at the tumor site through specific site reorganization mechanism, increase the time that the tumor would be exposed to the drug, and minimize the amount of drug able to enter healthy tissue as a result of the entrapment of the drug within a polymeric matrix. A summary of some of the main conclusions in this dissertation work is presented as below:

1. The first step in the design of the drug delivery was to achieve a complete polymeric coating on the magnetic iron oxide nanoparticles. Magnetic iron oxide nanoparticles were synthesized by one-pot polyol technique. This process enabled the liquid polyol to act not only as a solvent, but also as a mild reducing agent and a surfactant for the stabilization of the nanoparticles. The iron oxide nanoparticles synthesized were then coated with a copolymer of styrene- poly (styrene-co-vinylbenzylchloride-co-divinylbenzene) (PSVBDVB) which has better mechanical properties compared to polystyrene. Also, monomer vinylbenzylchloride used has chlorine on its para position that doesn't interfere in the polymerization process and provides a site for further functionalization of the polymer through nucleophilic substitution reactions. Complete encapsulation of the iron oxide nanoparticles with PSVBDVB copolymer was achieved

through precipitation polymerization process and was evident from the SEM images of the copolymer composites. The results indicated that the iron oxide nanoparticles are not only incorporated into the copolymer matrix but also act as nucleation sites for the polymerization process to begin. The polymerization process was found to have no effect on the magnetization of the nanoparticles. But the nanoparticles had several effects on the resultant polymeric composite size and morphology. As the loading of the nanoparticles was increase during the polymerization process, a decrease in the composite diameter was observed. Also an increase in the polydispersity, and decrease in the uniformity of the polymeric composition was detected. These effects of nanoparticle loading reported give insight into parameters that may need to be adjusted in order to obtain mono-dispersed polymeric composition with better mechanical properties.

2. In the second phase of the design of drug delivery system, the PSVBDVB polymer was replaced by a biocompatible and biodegradable polymer- Poly (lactide-co-glycolide) (PLGA). It has been approved by FDA for human applications. The PLGA composites containing the Fe@FeOx core shell nanoparticles and the drug analog [Ru(bpy) dye] was prepared by oil-in water emulsion solvent evaporation technique. The PLGA composites prepared were spherical but had a wider size distribution in the range of 500 nm to 2.5 μm. The local heating of the PLGA composites was also achieved by irradiating the Fe@FeOx nanoparticles with 2.45 GHz microwave radiations. The Ru(bpy) dye can be quenched by iron oxide nanoparticles. A decrease in the fluorescent intensity of the PLGA composites was observed when the composites were heated by microwaves or external heat source. This decrease in intensity observed was speculated to be due to the quenching of the released dye by the iron nanoparticles. The release of the Ru(bpy) dye

from the PLGA composites after microwave irradiation was successfully achieved. Also higher Ru(bpy) dye release from the composites by locally heating the sample with 2.45 GHz microwave pulse compared to externally heating the composite sample was demonstrated.

3. The final step is the design of controlled release drug delivery system with dual modal imaging and therapeutic capabilities. For an efficient drug delivery carrier the carrier size plays and important role, so the Fe@FeOx nanoparticles previously used were replaced by a chloroform based ferrofluid. The ferrofluid was synthesized by novel thermolysis technique using sodium oleate as the surfactant. The synthesized ferrofluid consisted of mono-dispersed 10 ± 5 nm in diameter. The nanoparticles were highly magnetic with saturation magnetization reaching 105 emu/g and 5 Oe corecivity. The ferrofluid and the drug analog-Rhodamine B dye were encapsulated into the PLGA polymer by modified oil-in-water emulsion technique and were confirmed by SEM. For achieving specific targeting capabilities the PLGA composites were functionalized with folic acid. The folic acid attachment to the PLGA was confirmed by IR and UV-Vis spectroscopy. The FA-PLGA composites were synthesized by the same modified oil-in-water emulsion technique. The release of the dye from the PLGA composites when placed in the Rf induction coil was determined by fluorescence spectroscopy and a linear increase in the fluorescent intensity was observed with time. The increase in the fluorescent intensity is observed indicating that the dye is released from the PLGA composites when locally heated. Also, the controlled release of the dye from the composites was achieved by a pulsed Rf treatment. Increase in the intensity is observed when the composites are heated with the Rf pulse ON and rate decreases when the Rf pulse is switched OFF. This

result confirms successful design of a controlled release therapeutic delivery system. The dye is released from the PLGA composites due to the swelling of the polymer and this is confirmed by dynamic light scattering measurements. Magnetic resonance imaging was also performed using the PLGA composites which showed enhancement in the T_2-weighted image contrast and thus negligible reduction in the contrast capabilities of the iron oxide particles (R_2 = 58.7 $s^{-1}mM^{-1}$). The PLGA composites containing the Rhodamine B dye and the iron oxide nanoparticles thus constitute a controlled release drug delivery system with dual modal imaging and therapeutic capabilities.

The present research contributed to the understanding of key parameters in the preparation of polymeric composites for therapeutic and imaging purposes. This work has added much to the understanding of the drug delivery system, and part of the ongoing work includes on achieving a stable water dispersion of the FA functionalized PLGA composites. Also a detailed cytotoxicity and intracellular uptake study of the composites needs to be done for further understanding the biological aspects needs to be concentrated for achieving an enhanced drug delivery system capable of replacing the conventional routes of drug administration.

7.1. Future work

7.1.1. Drug delivery application

The future step in the designing of the PLGA based drug delivery system is the incorporation of the anticancer drugs such as doxorubicin, paclitaxel, or platinum based drugs which are known to cause general toxicity. These drugs can be incorporated in the PLGA composites in the same manner by oil-in-water emulsification solvent evaporation technique in

which the drug analog- fluorescent dyes were incorporated in the present research.[203] For monitoring the release of the anticancer drugs from the PLGA composites, fluorescent tagged anticancer drugs can be used. The fluorescent tagging of the anticancer drugs makes it easy to monitor its release through fluorescent spectroscopy that has been very well established in this dissertation work. Also the drug release can also be determined by HPLC, and UV-Vis spectroscopy depending on the type of anticancer drug used. For example if doxorubicin is used as the active therapeutic agent, the encapsulation doxorubicin in PLGA composites can be determined by UV-Vis spectroscopy. Doxorubicin shows a absorbance maxima at 480nm that can be utilized to determine the drug concentration using a calibration curve method.[204,205]

It is also important to study the cytotoxicity of the prepared drug carrier. Cytotoxicity experiments need to be conducted on the prepared PLGA composites. The initial step would be to determine in-vitro cytotoxicity of the PLGA controls- the PLGA composites by itself and the PLGA composites containing the magnetic iron/iron oxide nanoparticles and finally the drug loaded magnetic PLGA composites. The next step has to be the in-vitro study of the heating effects of the composites on cell lines. It is necessary to confirm that the heat generated by the magnetic nanoparticles is within the defined hyperthermia range (42-46° C). The increase in the temperature of the sample when placed in the Rf induction coil can be measured by utilizing a fiber optic based thermometer. And the final step is to study the specific binding of the PLGA composites to the folate receptor on the cancerous cells.

7.1.2. Magnetic cell separation

Magnetic cell separation is a technique of cell sorting by incubating with magnetic nanoparticles coated with appropriate targeting ligands such as antibodies or proteins.[156,206] These surface coated magnetic nanoparticles bind to the call surface and can be magnetically

separated from the mixture and purified. The magnetic cell separation technique does not require a separating column.[207] It can be carried out in the sample tubes in liquid phase. The iron oxide nanoparticles loaded poly (styrene-co- vinylbenzylchloride-co-divinylbenzene) (PSVBDVB) composites prepared can be further functionalized with an appropriate targeting ligand and can be used for magnetic cell separation. The PSVBDVB composites can be functionalized with reactive dyes, e. g., Cibachrom Blue F3GA, or Procion Red for purification of purification of lysozyme, albumin, and lactate dehydrogenase.[207,208] The PSVBDVB composites can also be functionalized with streptavidin for isolation of biotinylated proteins.[209,210]

Chapter 8. References

List of References

(1)   Suzuki, R.; Rao, P.; Sasaguri, S. *Curr. Cancer Drug Tar.* **2007**, *7*, 273.

(2)   M., M. *Biodrug Delivery system*; Informa healthcare: Pinehurst, 2010.

(3)   Juillerat-Jeanneret, L.; Schmitt, F. *Med. Res. Rev.* **2007**, *27*, 574.

(4)   Mlineritsch, B. *Breast Care* **2009**, *4*, 162.

(5)   Cukierman, E.; Khan, D. R. *Biochem. Pharmacol.* **2010**, *80*, 762.

(6)   Fjallskog, M. L.; Frii, L.; Bergh, J. *Lancet* **1993**, *342*, 873.

(7)   Dorr, R. T. *The Annals of pharmacotherapy* **1994**, *28*, S11.

(8)   Walko, C. M.; McLeod, H. *Nat. Clin. Pract. Oncol.* **2009**, *6*, 153.

(9)   Patel, N. H.; Rothenberg, M. L. *Invest. New Drug* **1994**, *12*, 1.

(10)   Langer, R.; Tirrell, D. A. *Nature* **2004**, *428*, 487.

(11)   Selin, C. *Sci. Technol. Hum. Val.* **2007**, *32*, 196.

(12)   Whitesides, G. M. *Nature Biotechnol.* **2003**, *21*, 1161.

(13)   Jain, K. K. *Technology in Cancer Research & Treatment* **2005**, *4*, 407.

(14)   Duran, N.; Marcato, P. D.; Teixeira, Z.; Duran, M.; Costa, F. T. M.; Brocchi, M. *Current Nanoscience* **2009**, *5*, 396.

(15)   Gao, J. H.; Xu, B. *Nano Today* **2009**, *4*, 37.

(16)   Huber, D. L. *Small* **2005**, *1*, 482.

(17)   LaVan, D. A.; McGuire, T.; Langer, R. *Nat. Biotechnol.* **2003**, *21*, 1184.

(18)   Sinha, R.; Kim, G. J.; Nie, S. M.; Shin, D. M. *Mol. Cancer Ther.* **2006**, *5*, 1909.

(19)   Wang May, D.; Shin Dong, M.; Simons Jonathan, W.; Nie, S. *Expert Rev Anticanc.* **2007**, *7*, 833.

(20)   Ferrari, M. *Nat. Rev. Cancer* **2005**, *5*, 161.

(21)   Anon *Nat. Rev. Drug Discov.* **2007**, *6*, 174.

(22) Thies, C. *Mater. Res. Soc. Symp. Proc.* **1995**, *394*, 49.

(23) Brannon-Peppas, L.; Blanchette, J. O. *Adv. Drug Delivery Rev.* **2004**, *56*, 1649.

(24) Ferrari, M.; Barker, A. D.; Downing, G. J. *Nano Biotech.* **2005**, *1*, 129.

(25) Labhasetwar, V.; Song, C. X.; Levy, R. J. *Adv. Drug Deliv. Rev.* **1997**, *24*, 63.

(26) Pandey, A.; Singh, A. K.; Maurya, S. K.; Rai, R.; Shukla, H. S. *Dig. J. Nanomater. Bios.* **2008**, *3*, 141.

(27) Wong, H. L.; Chattopadhyay, N.; Wu, X. Y.; Bendayan, R. *Adv. Drug Deliver. Rev.* **2010**, *62*, 503.

(28) Chulia, D., Deleuil, M., Pourcelot, Y., In *Powder Technology and Pharmaceutical Processes*; Elsevier Science Publishing Company, New York: 1994.

(29) Cancer facts and figures 2009, American Cancer Society: 2009.

(30) Meinardi, M. T.; Gietema, J. A.; van Veldhuisen, D. J.; van der Graaf, W. T. A.; de Vries, E. G. E.; Sleijfer, D. T. *Cancer Treat. Rev.* **2000**, *26*, 429.

(31) Coates, A.; Abraham, S.; Kaye, S. B.; Sowerbutts, T.; Frewin, C.; Fox, R. M.; Tattersall, M. H. N. *Euro. J. Cancer Clin. On.* **1983**, *19*, 203.

(32) Kelland, L. *Nat. Rev. Cancer* **2007**, *7*, 573.

(33) Love, R. R.; Leventhal, H.; Easterling, D. V.; Nerenz, D. R. *Cancer* **1989**, *63*, 604.

(34) Spencer, C. M.; Faulds, D. *Drugs* **1994**, *48*, 794.

(35) Delaflorweiss, E.; Uziely, B.; Muggia, F. M. *Ann. Oncol.* **1993**, *4*, 723.

(36) Figgitt, D. P.; Wiseman, L. R. *Drugs* **2000**, *59*, 621.

(37) Carvalho, C.; Santos, R. X.; Cardoso, S.; Correia, S.; Oliveira, P. J.; Santos, M. S.; Moreira, P. I. *Curr. Med. Chem.* **2009**, *16*, 3267.

(38) Tebbi, C. K. *Cancer* **1993**, *71*, 3441.

(39) Farokhzad, O. C.; Langer, R. *Adv. Drug Deliv. Rev.* **2006**, *58*, 1456.

(40) Blasberg, R. G. *Mol. Cancer Ther.* **2003**, *2*, 335.

(41) Debbage, P.; Jaschke, W. *Histochem. Cell Biol.* **2008**, *130*, 845.

(42) Torchilin, V. P. *Nat. Rev. Drug Discov.* **2005**, *4*, 145.

(43)   Gref, R.; Minamitake, Y.; Peracchia, M. T.; Trubetskoy, V.; Torchilin, V.; Langer, R. *Science (New York, N.Y* **1994**, *263*, 1600.

(44)   Moghimi, S. M.; Hunter, A. C.; Murray, J. C. *Pharmacol. Rev.* **2001**, *53*, 283.

(45)   Sampathkumar, S. G.; Yarema, K. J. *Chemistry & biology* **2005**, *12*, 5.

(46)   Petkar, K. C.; Chavhan, S. S.; Agatonovik-Kustrin, S.; Sawant, K. K. *Crit. Rev. Ther. Drug* **2011**, *28*, 101.

(47)   Duncan, R. *Nat. Rev. Drug Discov.* **2003**, *2*, 347.

(48)   Bae, K. H.; Chung, H. J.; Park, T. G. *Mol. Cells* **2011**, *31*, 295.

(49)   Kratz, F.; Warnecke, A.; Schmid, B.; Chung, D. E.; Gitzel, M. *Curr. Med. Chem.* **2006**, *13*, 477.

(50)   Connors, T. A.; Knox, R. J. *Stem Cells* **1995**, *13*, 501.

(51)   Jain, N. K.; Asthana, A. *Expert Opin. Drug Del.* **2007**, *4*, 495.

(52)   Bai, S. H.; Thomas, C.; Rawat, A.; Ahsan, F. *Crit. Rev. Ther. Drug* **2006**, *23*, 437.

(53)   Oliveira, J. M.; Salgado, A. J.; Sousa, N.; Mano, J. F.; Reis, R. L. *Prog. Polym. Sci.* **2010**, *35*, 1163.

(54)   Smith, D. A. *Curr. Opin. Drug Disc.* **2007**, *10*, 550.

(55)   Singh, Y.; Palombo, M.; Sinko, P. J. *Curr. Med. Chem.* **2008**, *15*, 1802.

(56)   Dutta, T.; Jain, N. K.; McMillan, N. A. J.; Parekh, H. S. *Nanomed.-Nanotechnol.* **2010**, *6*, 25.

(57)   Fang, J. Y.; Hwang, T. L.; Huang, Y. L. *Curr. Nanosci.* **2006**, *2*, 55.

(58)   Medina, O. P.; Zhu, Y.; Kairemo, K. *Curr. Pharm. Design* **2004**, *10*, 2981.

(59)   Mondon, K.; Gurny, R.; Moller, M. *Chimia* **2008**, *62*, 832.

(60)   Torchilin, V. P. *Pharm. Res.* **2007**, *24*, 1.

(61)   Codde, J. P.; Lumsden, A. J.; Napoli, S.; Burton, M. A.; Gray, B. N. *Anticancer Res.* **1993**, *13*, 539.

(62)   Harper, B. W.; Krause-Heuer, A. M.; Grant, M. P.; Manohar, M.; Garbutcheon-Singh, K. B.; Aldrich-Wright, J. R. *Chem.- Eur. J.* **2010**, *16*, 7064.

(63)   Shi, Y.; Porter, W.; Merdan, T.; Li, L. C. *Expert Opin. Drug Del.* **2009**, *6*, 1261.

(64)   Torchilin, V. P. *J. Control. Release* **2001**, *73*, 137.

(65)   Teijon, J. M.; Trigo, R. M.; Garcia, O.; Blanco, M. D. *Biomaterials* **1997**, *18*, 383.

(66)   Venkatesh, S.; Saha, J.; Pass, S.; Byrne, M. E. *Eur. J. Pharm. Biopharm.* **2008**, *69*, 852.

(67)   Liu, Z.; Tabakman, S.; Welsher, K.; Dai, H. J. *Nano Res.* **2009**, *2*, 85.

(68)   Ilbasmis-Tamer, S.; Yilmaz, S.; Banoglu, E.; Degim, I. T. *J. Biomed. Nanotechnol.* **2010**, *6*, 20.

(69)   Gill, S.; Lobenberg, R.; Ku, T.; Azarmi, S.; Roa, W.; Prenner, E. J. *J. Biomed. Nanotechnol.* **2007**, *3*, 107.

(70)   Wadhwa, S.; Rea, C.; O'Hare, P.; Mathur, A.; Roy, S. S.; Dunlop, P. S. M.; Byrne, J. A.; Burke, G.; Meenan, B.; McLaughlin, J. A. *J. Hazard. Mater.* **2011**, *191*, 56.

(71)   Fubini, B.; Fenoglio, I.; Tomatis, M.; Turci, F. *Nanomedicine* **2011**, *6*, 899.

(72)   Fournier, E.; Passirani, C.; Montero-Menei, C. N.; Benoit, J. P. *Biomaterials* **2003**, *24*, 3311.

(73)   Staples, M. *Nanomed. Nanobiotechnol.* **2010**, *2*, 400.

(74)   Subramani, K.; Hosseinkhani, H.; Khraisat, A.; Hosseinkhani, M.; Pathak, Y. *Curr. Nanosci.* **2009**, *5*, 135.

(75)   Napier, M. E.; Desimone, J. M. *Polym. Rev.* **2007**, *47*, 321.

(76)   De Jong, W. H.; Borm, P. J. *Int. J. Nanomedicine* **2008**, *3*, 133.

(77)   Shultz, M. D.; Marin, J. R.; Naik, S. H.; Wilkins, J.; Laza, J. M.; Vilas, J. L.; Rodriguez, M.; Perez, N.; Carpenter, E. E. *J Appl Phys* **2009**, *105*.

(78)   Naik, S.; Carpenter, E. E. *J. Appl. Phys.* **2008**, *103*, 07A313.

(79)   Shultz, M. D.; Marin, J. R.; Naik, S. H.; Wilkins, J.; Laza, J. M.; Vilas, J. L.; Rodriguez, M.; Perez, N.; Carpenter, E. E. *J. Appl. Phys.* **2009**, *105*, 07B318.

(80)   Jalil, R.; Nixon, J. R. *J Microencapsul* **1990**, *7*, 53.

(81)   Mundargi Raghavendra, C.; Babu, V. R.; Rangaswamy, V.; Patel, P.; Aminabhavi Tejraj, M. *J Control Release* **2008**, *125*, 193.

(82)   de Jalon, E. G.; Blanco-Prieto, M. J.; Ygartua, P.; Santoyo, S. *Int. J. Pharm.* **2001**, *226*, 181.

(83)   Quintanar-Guerrero, D.; Allemann, E.; Fessi, H.; Doelker, E. *Drug Development and Industrial Pharmacy* **1998**, *24*, 1113.

(84)   Konan, Y. N.; Gurny, R.; Allemann, E. *Int J Pharm* **2002**, *233*, 239.

(85)   Nahar, M.; Dutta, T.; Murugesan, S.; Asthana, A.; Mishra, D.; Rajkumar, V.; Tare, M.; Saraf, S.; Jain, N. K. *Crit. Rev. Ther. Drug* **2006**, *23*, 259.

(86)   Kotti, K.; Kiparissides, C. *Macromol. React. Eng.* **2010**, *4*, 347.

(87)   Capek, I. *Adv. Colloid Interface* **2002**, *99*, 77.

(88)   Guo, J. S.; Sudol, E. D.; Vanderhoff, J. W.; Elaasser, M. S. *Acs Sym. Ser.* **1992**, *492*, 99.

(89)   Watts, P. J.; Davies, M. C.; Melia, C. D. *Crit. Rev. Ther. Drug* **1990**, *7*, 235.

(90)   Jaworek, A. *J. Microencapsul.* **2008**, *25*, 443.

(91)   Mohamed, F.; van der Walle, C. F. *J. Pharm. Sci.* **2008**, *97*, 71.

(92)   Jeffery, H.; Davis, S. S.; Ohagan, D. T. *Int. J. Pharm.* **1991**, *77*, 169.

(93)   Garti, N.; Bisperink, C. *Curr. Opin. Colloid In.* **1998**, *3*, 657.

(94)   Mundargi, R. C.; Babu, V. R.; Rangaswamy, V.; Patel, P.; Aminabhavi, T. M. *J. Control. Release* **2008**, *125*, 193.

(95)   Park, J. S.; Lee, J. H.; Shin, H. S.; Lee, T. W.; Kim, M. S.; Khang, G.; Rhee, J. M.; Lee, H. K.; Lee, H. B. *Tissue Eng. Regen. Med.* **2007**, *4*, 347.

(96)   Dinarvand, R.; Sepehri, N.; Manoochehri, S.; Rouhani, H.; Atyabi, F. *Int. J. Nanomed.* **2011**, *6*, 877.

(97)   Naranjos-Ramirez, N.; Torres-Cantu, D. I.; Castillo-Rodriguez, V. I.; Galindo-Rodriguez, S. A.; Chavez-Montes, A.; Castro-Rios, R.; Alvarez-Roman, R.; Martinez-Barbosa, M. E. *Rev. Mex. Fis.* **2011**, *57*, 41.

(98)   Vauthier, C.; Bouchemal, K. *Pharm. Res.* **2009**, *26*, 1025.

(99)   Schubert, S.; Delaney, J. T.; Schubert, U. S. *Soft Matter* **2011**, *7*, 1581.

(100)   Bilati, U.; Allemann, E.; Doelker, E. *Eur. J. Pharm.Sci.* **2005**, *24*, 67.

(101)   Galindo-Rodriguez, S.; Allemann, E.; Fessi, H.; Doelker, E. *Pharm. Res.* **2004**, *21*, 1428.

(102) Byrne James, D.; Betancourt, T.; Brannon-Peppas, L. *Adv. Drug Deliv. Rev.* **2008**, *60*, 1615.

(103) Shanle, E. K.; Xu, W. *Adv. Drug Deliver. Rev.* **2010**, *62*, 1265.

(104) Ciardiello, F.; De Vita, F.; Orditura, M.; Tortora, G. *Curr. Opin. Onco.* **2004**, *16*, 130.

(105) Sudimack, J.; Lee, R. J. *Adv. Drug Deliver. Rev.* **2000**, *41*, 147.

(106) Low, P. S.; Henne, W. A.; Doorneweerd, D. D. *Accounts of Chemical Research* **2008**, *41*, 120.

(107) Lu, Y. J.; Low, P. S. *Adv. Drug Deliver. Rev.* **2002**, *54*, 675.

(108) Clifton, G. T.; Sears, A. K.; Clive, K. S.; Holmes, J. P.; Mittendorf, E. A.; Ioannides, C. G.; Ponniah, S.; Peoples, G. E. *Hum. Vaccines* **2011**, *7*, 183.

(109) Laurent, S.; Bridot, J. L.; Elst, L. V.; Muller, R. N. *Future Med.Chem.* **2010**, *2*, 427.

(110) Wu, W.; He, Q. G.; Jiang, C. Z. *Nanoscale Res. Lett.* **2008**, *3*, 397.

(111) Yu, W. G.; Zhang, T. L.; Zhang, J. G.; Guo, J. Y.; Wu, R. F. *Prog. Chem.* **2007**, *19*, 884.

(112) Tural, B.; Oezenbas, M.; Atalay, S.; Volkan, M. *J. Nanosci. Nanotechno.* **2008**, *8*, 861.

(113) Carpenter, E. E.; Calvin, S.; Stroud, R. M.; Harris, V. G. *Chem Mater* **2003**, *15*, 3245.

(114) Willard, M. A.; Kurihara, L. K.; Carpenter, E. E.; Calvin, S.; Harris, V. G. *Int. Mater. Rev.* **2004**, *49*, 125.

(115) Fievet, F.; Lagier, J. P.; Blin, B.; Beaudoin, B.; Figlarz, M. *Solid State Ion.* **1989**, *32-3*, 198.

(116) Gupta, A. K.; Gupta, M. *Biomaterials* **2005**, *26*, 3995.

(117) Liu, F. J.; Laurent, S.; Fattahi, H.; Elst, L. V.; Muller, R. N. *Nanomedicine* **2011**, *6*, 519.

(118) Frimpong, R. A.; Hilt, J. Z. *Nanomedicine* **2010**, *5*, 1401.

(119) Tartaj, P. *Eur. J. Inorg. Chem.* **2009**, 333.

(120) Mahmoudi, M.; Sant, S.; Wang, B.; Laurent, S.; Sen, T. *Adv. Drug Deliver. Rev.* **2011**, *63*, 24.

(121) Xu, C. J.; Sun, S. H. *Polym. Int.* **2007**, *56*, 821.

(122) Laurent, S.; Forge, D.; Port, M.; Roch, A.; Robic, C.; Elst, L. V.; Muller, R. N. *Chem. Rev.* **2008**, *108*, 2064.

(123)	Laurent, S.; Boutry, S.; Mahieu, I.; Vander Elst, L.; Muller, R. N. *Curr. Med. Chem.* **2009**, *16*, 4712.

(124)	Vats, N.; Wilhelm, C.; Rautou, P. E.; Poirier-Quinot, M.; Pechoux, C.; Devue, C.; Boulanger, C. M.; Gazeau, F. *Nanomedicine* **2010**, *5*, 727.

(125)	Lin, S. P.; Brown, J. J. *J. Magn. Reson. Imaging* **2007**, *25*, 884.

(126)	Marzola, P.; Boschi, F.; Sbarbati, A. *Curr. Med. Imaging Rev.* **2006**, *2*, 291.

(127)	Na, H. B.; Song, I. C.; Hyeon, T. *Adv. Mater.* **2009**, *21*, 2133.

(128)	Zhang, Z. D.; Nair, S. A.; McMurry, T. J. *Curr. Med. Chem.* **2005**, *12*, 751.

(129)	Hasebroock, K. M.; Serkova, N. J. *Expert Opin. Drug Met.* **2009**, *5*, 403.

(130)	Lacroix, L. M.; Ho, D.; Sun, S. H. *Curr. Top. Med. Chem.* **2010**, *10*, 1184.

(131)	Nijdam, A. J.; Nicholson, T. R.; Shapiro, J. P.; Smith, B. R.; Heverhagen, J. T.; Schmalbrock, P.; Knopp, M. V.; Kebbel, A.; Wang, D.; Lee, S. C. *Curr. Nanosci.* **2009**, *5*, 88.

(132)	Weinstein, J. S.; Varallyay, C. G.; Dosa, E.; Gahramanov, S.; Hamilton, B.; Rooney, W. D.; Muldoon, L. L.; Neuwelt, E. A. *J. Cerebr. Blood F. Met.* **2010**, *30*, 15.

(133)	Sharma, R.; Chen, C. J. *J. Nanopart. Res.* **2009**, *11*, 671.

(134)	van der Zee, J. *Ann.Oncol.* **2002**, *13*, 1173.

(135)	Namdeo, M.; Saxena, S.; Tankhiwale, R.; Bajpai, M.; Mohan, Y. M.; Bajpai, S. K. *J. Nanosci. Nanotechno.* **2008**, *8*, 3247.

(136)	Silva, A. C. S. A. C.; Oliveira, T. R.; Mamani, J. B.; Malheiros, S. M. F.; Malavolta, L.; Pavon, L. F.; Sibov, T. T.; Amaro, E.; Tannus, A.; Vidoto, E. L. G.; Martins, M. J.; Santos, R. S.; Gamarra, L. F. *Int. J. Nanomed.* **2011**, *6*, 591.

(137)	Cherukuri, P.; Glazer, E. S.; Curleya, S. A. *Adv. Drug Deliver. Rev.* **2010**, *62*, 339.

(138)	Dias, A.; Hussain, A.; Marcos, A. S.; Roque, A. C. A. *Biotech. Adv.* **2011**, *29*, 142.

(139)	Lemarchand, C.; Gref, R.; Couvreur, P. *Eur. J. Pharm. Biopharm.* **2004**, *58*, 327.

(140)	Soenen, S. J. H.; De Cuyper, M. *Nanomedicine* **2010**, *5*, 1261.

(141)	Shim, S. E.; Yang, S. Y.; Choe, S. J. *J. Polym. Sci. Pol. Chem.* **2004**, *42*, 3967.

(142) Joseyphus, R. J.; Shinoda, K.; Kodama, D.; Jeyadevan, B. *Mater. Chem. Phys.* **2010**, *123*, 487.

(143) Shultz, M. D.; Braxton, W.; Taylor, C.; Carpenter, E. E. *J. Appl. Phys.* **2009**, *105*.

(144) Camponeschi, E.; Walker, J.; Garmestani, H.; Tannenbaum, R. *J. Non-Cryst. Solids* **2008**, *354*, 4063.

(145) Rodriguez, C.; Castro, E.; Martin, A.; Marin, J. R.; Berganza, J.; Cuevas, J. M. *Micro Nano Lett.* **2011**, *6*, 349.

(146) Holder, S. J.; Durand, G. G.; Yeoh, C. T.; Illi, E.; Hardy, N. J.; Richardson, T. H. *J. Polym. Sci. A1* **2008**, *46*, 7739.

(147) Ammar, S.; Jouini, N.; Fievet, F.; Stephan, O.; Marhic, C.; Richard, M.; Villain, F.; Moulin, C. C. D.; Brice, S.; Sainctavit, P. *J. Non-Cryst. Solids* **2004**, *345-46*, 658.

(148) Odenbach, S. *J. Phys-Condens Mat.* **2004**, *16*, R1135.

(149) Shim, S. E.; Yang, S. Y.; Choe, S. J. *J Polym Sci A Polym Chem* **2004**, *42*, 3967.

(150) Shim, S. E.; Yang, S.; Jin, M. J.; Chang, Y. H.; Choe, S. *Colloid Polym. Sci.* **2004**, *283*, 41.

(151) Downey, J. S.; Frank, R. S.; Li, W. H.; Stover, H. D. H. *Macromolecules* **1999**, *32*, 2838.

(152) Lamleung, S. Y.; Li, H. R. *J. Appl. Polym. Sci.* **1995**, *57*, 1373.

(153) Al Malyan, M.; Becchi, C.; Nikkola, L.; Viitanen, P.; Boncinelli, S.; Chiellini, F.; Ashammakhi, N. *J. Craniofac.Surg.* **2006**, *17*, 302.

(154) Levison, P. R.; Badger, S. E.; Dennis, J.; Hathi, P.; Davies, M. J.; Bruce, I. J.; Schimkat, D. *J. Chromatog. A* **1998**, *816*, 107.

(155) Franzreb, M.; Siemann-Herzberg, M.; Hobley, T. J.; Thomas, O. R. T. *Appl. Microbiol. Biot.* **2006**, *70*, 505.

(156) Yavuz, C. T.; Prakash, A.; Mayo, J. T.; Colvin, V. L. *Chem. Eng. Sci.* **2009**, *64*, 2510.

(157) Rytting, E.; Nguyen, J.; Wang, X. Y.; Kissel, T. *Expert Opin. Drug Del.* **2008**, *5*, 629.

(158) Sintzel, M. B.; Bernatchez, S. F.; Tabatabay, C.; Gurny, R. *Eur. J. Pharm. Biopharm.* **1996**, *42*, 358.

(159) Zhang, M. P.; Yang, Z. C.; Chow, L. L.; Wang, C. H. *J. Pharm. Sci.* **2003**, *92*, 2040.

(160) von Burkersroda, F.; Schedl, L.; Gopferich, A. *Biomaterials* **2002**, *23*, 4221.

(161)   Luo, Y.; Prestwich, G. D. *Expert Opin. Ther. Pat.* **2001**, *11*, 1395.

(162)   Rothstein, S. N.; Federspiel, W. J.; Little, S. R. *Biomaterials* **2009**, *30*, 1657.

(163)   Soares, J. S.; Zunino, P. *Biomaterials* **2010**, *31*, 3032.

(164)   Sintzel, M. B.; Merkli, A.; Heller, J.; Tabatabay, C.; Gurny, R. *Int. J. Pharm.* **1997**, *155*, 263.

(165)   Heller, J.; Barr, J.; Ng, S. Y.; Shen, H. R.; Schwach-Abdellaoui, K.; Emmahl, S.; Rothen-Weinhold, A.; Gurny, R. *Eur. J. Pharm. Biopharm.* **2000**, *50*, 121.

(166)   Katti, D. S.; Lakshmi, S.; Langer, R.; Laurencin, C. T. *Adv. Drug Deliver. Rev.* **2002**, *54*, 933.

(167)   Kumar, N.; Langer, R. S.; Domb, A. J. *Adv. Drug Deliver. Rev.* **2002**, *54*, 889.

(168)   Gopferich, A.; Tessmar, J. *Adv. Drug Deliver. Rev.* **2002**, *54*, 911.

(169)   Kumbar, S. G.; Bhattacharyya, S.; Nukavarapu, S. P.; Khan, Y. M.; Nair, L. S.; Laurencin, C. T. *J. Inorg. Organomet. P.* **2006**, *16*, 365.

(170)   Qiu, L. Y.; Zhu, K. J. *Acta Polym. Sin.* **2001**, 660.

(171)   Lassalle, V.; Ferreira, M. L. *Macromole. Biosci.* **2007**, *7*, 767.

(172)   Oh, J. K. *Soft Matter* **2011**, *7*, 5096.

(173)   Jalil, R.; Nixon, J. R. *J Microencapsul* **1990**, *7*, 41.

(174)   Astete, C. E.; Sabliov, C. M. *J. Biomater. Sci., Polym. Ed.* **2006**, *17*, 247.

(175)   Zhang, L.; Liu, B.; Dong, S. *J. Phys. Chem. B* **2007**, *111*, 10448.

(176)   Yuan, J. P.; Wang, E. *Electroanalysis* **2008**, *20*, 949.

(177)   Saha, D.; Das, S.; Maity, D.; Dutta, S.; Baitalik, S. *Inorg. Chem.* **2011**, *50*, 46.

(178)   Villa, I.; Sanchez, F.; Lopes, T.; Lopez-Cornejo, P.; Perez-Tejeda, P. *J. Phys. Chem. A* **2010**, *114*, 7912.

(179)   Pileni, M. P. *J. Exp. Nanosci.* **2006**, *1*, 13.

(180)   Carpenter, E. E.; Calvin, S.; Stroud, R. M.; Harris, V. G. *Chemistry of Materials* **2003**, *15*, 3245.

(181)   Shultz, M. D.; Calvin, S.; Fatouros, P. P.; Morrison, S. A.; Carpenter, E. E. *Journal of Magnetism and Magnetic Materials* **2007**, *311*, 464.

(182)   Foster, K. R.; Glaser, R. *Health Phys.* **2007**, *92*, 609.

(183)   Foster, K. R.; Lozano-Nieto, A.; Riu, P. J. *Bioelectromagnetics* **1998**, *19*, 420.

(184)   D'Andrea, J. A.; Ziriax, J. M.; Adair, E. R. *Prog. Brain Res.* **2007**, *162*, 107.

(185)   Breckenkamp, J.; Berg, G.; Blettner, M. *Radiat. Environ. Biophys.* **2003**, *42*, 141.

(186)   Roman, N. M.; Dan, V.; Ciupa, R. V.; Pompas, V. In *World Congress on Medical Physics and Biomedical Engineering, Vol 25, Pt 6*; Dossel, O., Schlegel, W. C., Eds. 2009; Vol. 25, p 103.

(187)   Wischke, C.; Schwendeman, S. P. *Int. J. Pharm.* **2008**, *364*, 298.

(188)   Takai, C.; Hotta, T.; Shiozaki, S.; Matsumoto, S.; Fukui, T. *Colloid Surface A* **2011**, *373*, 152.

(189)   Carroll, K. J.; Shultz, M. D.; Fatouros, P. P.; Carpenter, E. E. *J. Appl. Phys.* **2010**, *107*.

(190)   Massart, R.; Dubois, E.; Cabuil, V.; Hasmonay, E. *J. Magn.Magn. Mater* **1995**, *149*, 1.

(191)   Pileni, M. P.; Zemb, T.; Petit, C. *Chemical Physics Letters* **1985**, *118*, 414.

(192)   Ravikumar, C.; Bandyopadhyaya, R. *J. Phys. Chem. C* **2011**, *115*, 1380.

(193)   Kim, Y. H.; Lee, D. K.; Jo, B. G.; Jeong, J. H.; Kang, Y. S. *Colloid Surface A* **2006**, *284*, 364.

(194)   Das, S. N.; Panda, M. *Asian J. Spectrosc.* **2003**, *7*, 87.

(195)   Thire, R.; Meiga, T. O.; Dick, S.; Andrade, L. R. *Macromol. Sy.* **2007**, *258*, 38.

(196)   Croll, T. I.; O'Connor, A. J.; Stevens, G. W.; Cooper-White, J. J. *Biomacromolecules* **2004**, *5*, 463.

(197)   Cho, H. S.; Dong, Z. Y.; Pauletti, G. M.; Zhang, J. M.; Xu, H.; Gu, H. C.; Wang, L. M.; Ewing, R. C.; Huth, C.; Wang, F.; Shi, D. L. *Acs Nano* **2010**, *4*, 5398.

(198)   JCPDS Card No. 01-089-5892.

(199)   He, Y. Y.; Wang, X. C.; Jin, P. K.; Zhao, B.; Fan, X. Y. *Spectrochim. Acta A* **2009**, *72*, 876.

(200)   Stella, B.; Arpicco, S.; Peracchia, M. T.; Desmaele, D.; Hoebeke, J.; Renoir, M.; D'Angelo, J.; Cattel, L.; Couvreur, P. *J. Pharm. Sci.* **2000**, *89*, 1452.

(201)   Hiraoka, M.; Mitsumori, M.; Hiroi, N.; Ohno, S.; Tanaka, Y.; Kotsuka, Y.; Sugimachi, K. *Ieee T. Microw. Theory* **2000**, *48*, 1789.

(202)   Kato, H.; Ishida, T. *Med. Biol. Eng. Comput.* **1993**, *31*, S2.

(203)   Diao, Y. Y.; Han, M.; Ding, P. T.; Chen, D. W.; Gao, J. Q. *Pharmazie* **2010**, *65*, 356.

(204)   Yoo, H. S.; Lee, K. H.; Oh, J. E.; Park, T. G. *J. Control. Release* **2000**, *68*, 419.

(205)   Yoo, H. S.; Oh, J. E.; Lee, K. H.; Park, T. G. *Pharm. Res.* **1999**, *16*, 1114.

(206)   Safarik, I.; Safarikova, M. *J. Chromatog. B* **1999**, *722*, 33.

(207)   Thiel, A.; Scheffold, A.; Radbruch, A. *Immunotechnology* **1998**, *4*, 89.

(208)   Kodituwakku, A. P.; Jessup, C.; Zola, H.; Roberton, D. M. *Immunol. Cell Biol.* **2003**, *81*, 163.

(209)   Hsing, I. M.; Xu, Y.; Zhao, W. T. *Electroanal.* **2007**, *19*, 755.

(210)   Safarik, I.; Safarikova, M. *J. Chromatogr. B.* **1999**, *722*, 33.

VITA

Sweta Hemang Naik was born on October 31st, 1979 in Kalyan, India and is an Indian citizen. She graduated from Bright School, Baroda, India in 1997. She received her Bachelors of Science in 2000 and Masters of Science in 2002 from South Gujarat University, India. She worked as a graduate teaching assistant and graduate research assistant during her graduate studies at Virginia Commonwealth University.